UNIVERSITÄT PADERBORN
Die Universität der Informationsgesellschaft

Fakultät für Naturwissenschaften - Department Physik

Micro- and nanodevices for optoelectronic applications based on II-VI semiconductors

Dem Department Physik der Universität Paderborn
zur Erlangung desakademischen Grades eines
Doktors der Naturwissenschaften vorgelegte

Dissertation

von M.Sc. Marina Panfilova

Paderborn, 2010

Promotionskommission
Prof. Dr. Wolf Gero Schmidt (Vorsitzender)
Prof. Dr. Klaus Lischka (1. Gutachter)
Prof. Dr. Christine Silberhorn (2. Gutachter)
Dr. Christof Hoentzsch

Tag der Einreichung: 21. Mai 2010
Tag der mündlichen Prüfung: 12. Juli 2010

Abstract

In the past decade, there has been tremendous activities in the development of a quantum computer, a machine that would exploit the full complexity of a many-particle quantum wave function to solve a computational problem. Some of the active key components may rely on semiconductor devices with opto-electronic functions. In this thesis, devices like microdisk laser and photodiode based on II-VI semiconductor systems including impurities and quantum dots for quantum information technology were studied. We find that wide-bandgap II-VI semiconductor alloys are promising materials for short-wavelength opto-electronic devices with applications in photonics and quantum information technology.

Excitons bound to fluorine donors in ZnSe appear to meet most requirements for quantum memories. Lasing in ZnSe donor-bound excitons may be particularly useful as a component in quantum information processing devices which require a low-noise source laser, nearly resonant with the bound-exciton transitions used for qubit initialization, control, and readout. Semiconductor microdisks are promising for applications such as low-threshold lasers [McCall], [Slusher] and efficient solid-state based single photon emitters [Zwiller]. In this work, a fabrication process of microdisks based on a strained fluorine-doped ZnSe quantum well was developed. The structural properties of these microdisks, such as strain distribution and the density of extended defects were studied. Also, the optical characteristics of the disks were investigated and lasing was observed. We find that the laser threshold of our optically pumped devices is extremely low, among the latest values reported so far for a devices in the blue-green spectral area.

While microdisk cavities are applicable as low-threshold lasers, membranes constitute waveguides structures for interconnecting microdisks in integrated photonic circuits. In this context ZnSe/ZnMgSe membrane structures were fabricated. Investigations of strain

distribution and of extended defects density were carried out, demonstrating a step towards the fabrication of membranes with a photonic crystal for single-photon emitters and integrated optical waveguide systems with II-VI compound semiconductors.

Another approach to realise semiconductor qubits for quantum technology makes use of a two-level system which is formed by the exciton ground state in a single quantum dot. For this reason, self assembled Stranski-Krastanov CdSe quantum dots were embedded in ZnSe and enclosed in a Schottky photodiode with a near-field shadow mask on a semi-transparent contact. Electrical and optical access was provided to investigate the quantum states of individual quantum dot excitons. We found a redshift of the photoluminescence due to the quantum confined Stark effect at increasing negative bias voltage. At resonant excitation of the quantum dot excitons, a photocurrent signal was achieved which is considered as the first demonstration of an electric readout of the wide-gap CdSe quantum dots.

Contents

1 Introduction

Today many people are familiar with at least the consequences of Moore's Law [1] published 1965 – the fastest computer available in sales doubles in speed about every two years. This is because electronic component devices are shrinking getting smaller and smaller. The smaller and denser they get on a semiconductor chip, the faster they work. In strongly reduced structures with size down to several nanometers, a physical end of the classic design of computer devices was predicted due to predominantly increasing quantum effects. The fact that single charge carriers exhibit wave-like properties and are furthermore able to perform tunnelling processes through small potential barriers is a handicap for the classic design of semiconductor structures.

In contrast to conventional information technology, fundamental quantum phenomena play a central role for quantum information technology – information is stored, processed and communicated according to the laws of quantum physics. The combination of quantum mechanics and computers forms a new subject – quantum computers. Feynman considered this possibility in 1985 [2] and concluded optimistically:

"it seems that the laws of physics present no barrier to reducing the size of computers until the bits are the size of atoms, and quantum behaviour holds dominant sway".

The development of quantum information technologies is nowadays certainly one of the most important achievements in research.

Compared to the digital bit that is always in the state $|0\rangle$ or $|1\rangle$, the quantum bit (qubit) has rather more freedom. In a quantum computer the state of the bit can be described by a wave function, which consists of a superposition of qubit states $\Psi = a|0\rangle + b|1\rangle$, where the coefficients a and b are complex numbers representing the probability that the qubit is in the corresponding state. If it is possible to operate simultaneously with all the states of a quantum register, there is clearly the possibility of achieving fast computational speeds by massive parallel computation based on quantum superpositions.

At the moment, there are few physical implementations of quantum computers, that compose of only a few number of qubits. In 2009, researchers at Yale University created

the first rudimentary solid-state quantum processor [3]. The two-qubit superconducting chip was able to run elementary algorithms. Another team, working at University of Bristol, created a silicon-based quantum computing chip, based on quantum optics [4]. The team was able to run Shor's prime factoring algorithm on the chip.

Quantum information research promises more than computers. A similar technology allows quantum communication which enables the sharing of secrets with quantum cryptography, a security guarantee by the laws of physics. The full spectrum of potential technologies have probably not yet been imagined, nor will it be until actual quantum information hardware is available for future generations of quantum engineers [5].

The central question is what form quantum hardware will take, and for this there are no easy answers. Quantum bits are often imagined to be constructed from the smallest form of matter, an isolated atom, as in ion traps or optical lattices, but they may likewise be made from electrical components far larger than routine electronic components, as in some superconducting systems, or even from a vial of liquid, as in nuclear magnetic resonance. It would be convenient if a quantum computer could be made out of the same material that current computers are made out of, i.e. silicon, but it may well be that they will be made of an entirely different material.

In this thesis, for the realization of qubits, II-VI semiconductor systems including impurities and quantum dots (QDs) were studied. The individual fluorine impurity has a single nuclear spin of ½ embedded in isotopically pure ZnSe, which has a nuclear spin of 0. At low temperatures, a donor electron is bound to the fluorine nucleus with a recombination lifetime less than 100 ps [6]. These donor electrons may mediate nuclear spin interactions and allow nuclear qubits to be individually measured. This is a similar system to phosphorous in silicon. However, unlike in silicon, the direct, wide bandgap of ZnSe provides an oscillator strength comparable to a QD. Furthermore, laser based on ZnSe donor-bound excitons may be particularly useful as a component in quantum information processing devices, which require a low-noise source laser nearly resonant with the bound-exciton transitions used for qubit initialization, control, and readout.

The other approach to investigate semiconductor qubits makes use of a two-level system, which is formed by the exciton states in a single QD. CdSe QDs in ZnSe provides higher confinement in comparison to the extensively investigated InGaAs QDs embedded in GaAs. Therefore the CdSe/ZnSe material system is an attractive candidate for coherent operation at elevated temperatures. Furthermore, in CdSe QDs the exciton-biexciton energy difference is considerably higher than in III-V system. This allows a significant

decrease of the excitation pulse duration and thus a higher number of coherent manipulations within the dephasing time.

The highlight of the work presented here is the demonstration of the preliminary devices for qubit realization based on fluorine impurities and CdSe QDs. Resonator structures like microdisks (MDs) present low-threshold lasing based on fluorine impurity bound-exciton transitions. Free standing membranes allow the waveguide structures for coupling of several devices like MDs. Photodiodes with enclosed individual CdSe QD provide electrical and optical access to probe and modify the quantum state of QD excitons. The realization of these devices is an important step forward to future quantum devices.

Outline of this thesis

This work starts with the introduction into the experimental methods regarding growth methods, basic structural and optical properties, and spectroscopic methods. The details of the experimental setups are explained in chapter two.

The MD resonator is presented in chapter three. In the beginning of the chapter, the basic concepts of the MD resonator and its lasing properties are explained briefly to provide a fundamental basis for further discussion. Next the fabrication process of the first MDs from a strained II-VI system on a pedestal is described. The investigation of the structural properties of MDs by means of photoluminescence and Raman spectroscopy is presented. Finally the highlight – low threshold lasing in MDs contributed by fluorine impurities is demonstrated. The lasing modes are described by their theoretical simulation that has been done by Christoph Claßen from the group of Prof. R. Schuhmann.

In order to perform the waveguides, first freestanding micro-membranes were fabricated, as described in chapter four. Investigations of the structural and optical properties of the membranes are presented.

In chapter five the basic concepts and the fabrication of the QD photodiodes are explained. The optical properties of the CdSe QDs in the photodiodes are presented. Lastly the highlight – first evidence of a resonant photocurrent signal is demonstrated. This research has been done in close collaboration with Steffen J. Michaelis de Vasconcellos from Prof. A. Zrenner's group.

A conclusion of the results and achievements of this work, together with an outlook presenting the perspective of future investigations based on this work, is given in chapter six.

2 Experimental Methods

In this chapter a brief introduction of the experimental methods for the growth and characterization of semiconductor layers is given. Firstly, a description of the molecular beam epitaxy system used for growth is presented. Secondly, the characterization methods such as high resolution X-ray diffraction, Raman and photoluminescence spectroscopy which have been used for the investigation of the epitaxial layers as well as completed devices are introduced.

2.1 Molecular beam epitaxy

The crystal growth by molecular beam epitaxy (MBE) is a standard method for high-quality semiconductor layers. The samples used in this work were grown in a MBE system with two coupled ultra high vacuum (UHV) chambers for III-V and II-VI materials. Figure 1 shows a schematic cross section of an MBE setup with the main components. The III-V system is equipped with a standard Knudsen effusion cell for the evaporation of gallium and with a cracker-cell for the evaporation of arsenic. The II-VI system is equipped with standard effusion cells for the deposition of zinc, magnesium, cadmium and zinc fluoride,

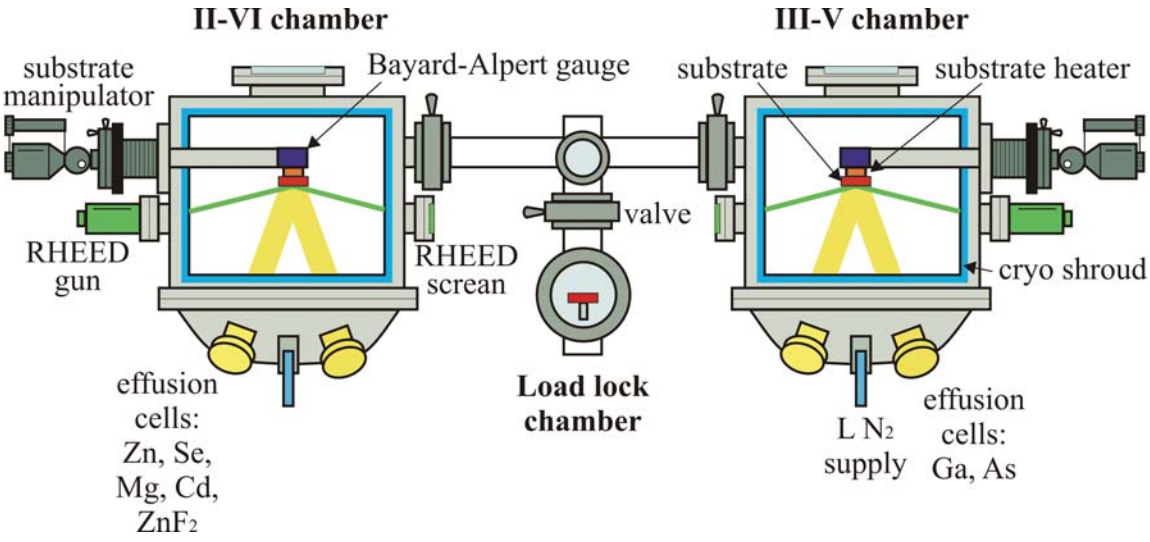

Figure 1. Schematic cross section of an MBE setup consisting of two epitaxy chambers and a connective load lock chamber.

as well as with a cracker-cell for the evaporation of selenium. The typical purity of the evaporated materials is 99,9999% (6N). All cells are equipped with shutters for the opening and closing of the molecular beam. Both chambers are provided with a temperature controlled substrate heater (PID controller). The fluxes of the cells, i.e. the beam equivalent pressure of the cells are measured by means of Bayard-Alpert ion gauges to guarantee reproducible conditions during different growth runs. A liquid nitrogen-cooled shroud is used in order to minimize any residual vapor in the central part of the vacuum chamber during growth. The substrate is locked-in into the system through the load lock chamber, which is connected with both MBE chambers and allows to transfer the substrate from one chamber into the other under UHV conditions.

For the in-situ control of the layer growth Reflection High Energy Electron Diffraction (RHEED) was used [7]. RHEED is an experimental technique for determining the properties of crystalline surfaces. A focused beam of high energy (5 - 20 keV) electrons is directed at grazing incidence (1-2°) to the sample which limits the beam penetration depth and makes the probe highly surface-sensitive. Figure 2 shows the schematic diagram of the elastically scattered electrons in real space geometry. Electrons diffracted from the surface are detected with a fluorescence screen placed opposite the RHEED gun. Atoms at the sample surface diffract (scatter) the incident electrons due to the wavelike properties of electrons. The scattered wave vector lies on the surface of the sphere of constant energy, the so-called Ewald sphere. In reciprocal space, the two-dimensional array of the surface atoms turns into vertical lines, the reciprocal rods. Wherever these rods cross the Ewald sphere, the condition for constructive interference of the elastically scattered electron beams from the surface is fulfilled. Therefore, these crossing points in reciprocal space

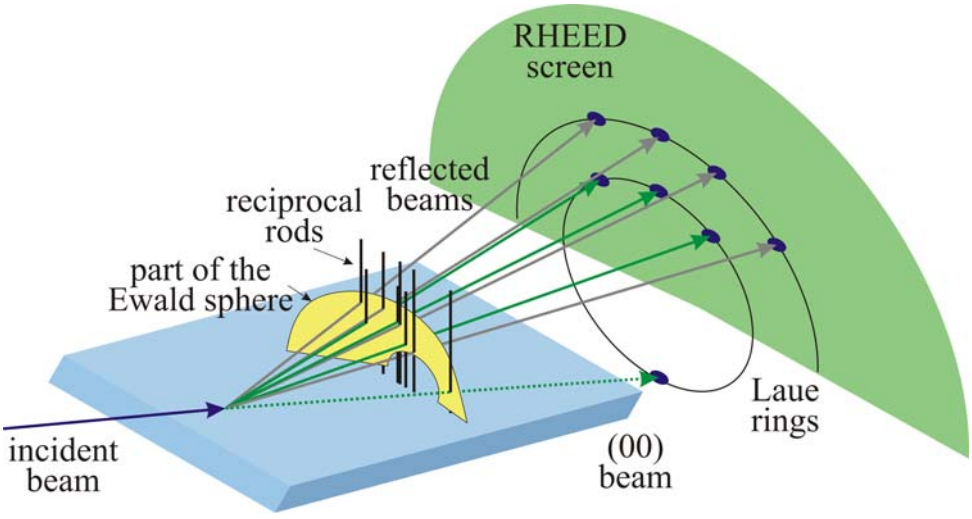

Figure 2. Schematic diagram of the RHEED diffraction geometry.

determine the directions of constructive interference for the electrons in real space. These scattered electron beams hit a fluorescent screen in certain RHEED spots, lying on so-called Laue circles. The observed RHEED-pattern can be used to monitor the growth stoichiometry, the state of the surface and the growth rate in real time.

2.2 High resolution X-ray diffraction

High resolution X–ray diffraction (HRXRD) was used for the non-destructive ex-situ analysis of the epitaxial layers. By HRXRD it is possible to obtain information about the composition and uniformity of epitaxial layers, their thickness, built-in strain, strain relaxation and crystalline perfection, which is related to the dislocation density in the crystal volume.

The diffraction of X-rays on crystal planes is described by the Bragg equation [8]:

$$2d_{hkl} \cdot \sin\Theta = n'\lambda \qquad \text{Eq. 1}$$

where λ is the wavelength of the X-ray radiation, n' is the order of the diffracted beam, Θ is the incidence angle of radiation and d_{hkl} is the spacing of the lattice planes given by

$$d_{hkl} = \frac{a_0}{\sqrt{h^2 + k^2 + l^2}} \qquad \text{Eq. 2}$$

with a_0 - the lattice constant and (hkl) - triplet of Miller indices, which assign the diffracted rays in the reciprocal space. The Bragg reflexes can be detected only when the incident angle to the lattice plane is equal to the diffracted angle. In reciprocal space the diffraction planes (which consist of lattice points) present reciprocal lattice points as indicated in Figure 3. The diffraction geometry is defined by the incident vector $\vec{k}_i$ and the diffracted

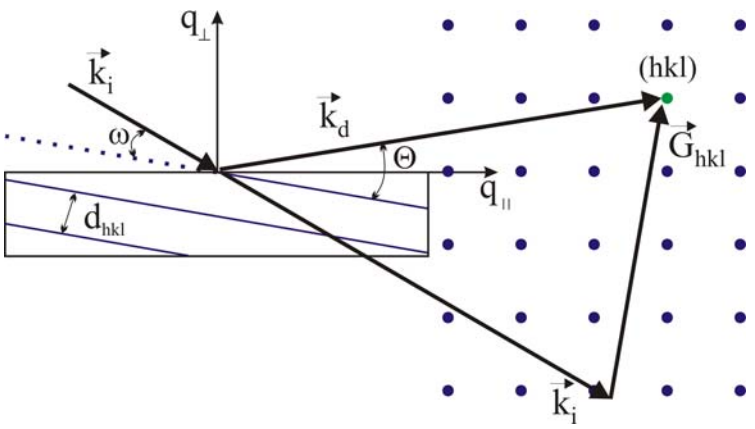

Figure 3. Sketch of the diffraction geometry. The exact Bragg condition for lattice planes is fulfilled, if the scattering vector $\vec{G}_{hkl}$ ends at a reciprocal lattice point (hkl).

vector $\vec{k}_d$ that are represented by the scattering vector $\vec{G}_{hkl}$. When the scattering vector ends at a reciprocal lattice point (hkl), the exact Bragg condition is fulfilled. The measurements and detailed analysis of diffracted intensity around reciprocal lattice points is the subject of high resolution diffractometry.

The angular variation of the incident beam allows to analyse different crystal properties. If the detector angle is fixed and the sample is rotated, the ω-scans, so-called rocking curves, can be measured. From the width of the rocking curve the edge and screw dislocation density (DD) can be calculated with the model of Gay et al. [9]:

$$DD = \frac{\Delta\omega^2}{9b^2} \qquad \text{Eq. 3}$$

with the Burgers vector $b = a_0/\sqrt{2}$ for most common 60° dislocations [10]. Thereby a_0 is the lattice parameter. If the angular rotation speed of the detector is twice that of the incident angle, the ω-2Θ-scans can be measured. With this kind of scan geometry it is possible to get information on lattice parameter and chemical composition of epitaxial layers. With a combination of ω-scans and ω-2Θ-scans a two dimensional distribution of intensity in reciprocal space, so-called reciprocal space map (RSM), can be observed. Using this mode it is possible to get information about the strain status and the chemical composition of the crystal.

In this work, the 3-axis X'Pert diffractometer from PANalytical with an X-ray radiation of the Cu-$K_{\alpha 1}$-line with wavelength of 1.54056 Å was used for the X-ray analysis. The resolution of the equipment is about 8 arcsec.

2.3 Raman spectroscopy

Raman spectroscopy allows the observation of elementary excitations of solids by the frequency shift between incident and scattered photons of a sample [11]. From the point of view of quantum mechanics the first step in a Raman process is the absorption of a photon ħω. This leads to an electronic intermediate state which may interact with elementary excitations, e.g. phonons with quantum energy ħΩ, via several mechanisms (e.g. Fröhlich interaction), and elementary excitations are created or annihilated. Finally charges in the scattered intermediate state recombine by emitting a photon with a different frequency $\hbar\omega_s$. Energy is conserved in the whole process under the condition that

$$\hbar\omega = \hbar\omega_s \pm \hbar\Omega \ . \qquad \text{Eq. 4}$$

The scattering of light without change of frequency is called Rayleigh scattering, and the scattering of light with change of frequency is called Raman scattering. The emission/absorption of elementary excitations via an intermediate state is called Stokes or anti-Stokes scattering, respectively. Figure 4 schematically shows the energy levels for the Rayleigh scattering, Stokes, and anti-Stokes Raman scattering. For each intermediate step the crystal momentum which is expressed by

$$\boldsymbol{k} = \boldsymbol{k_s} \pm \boldsymbol{q} \qquad \text{Eq. 5}$$

has to be conserved. In this equation $\boldsymbol{k}$ and $\boldsymbol{k_s}$ are photon wavevectors and $\boldsymbol{q}$ is the crystal momentum vector of the elementary excitation. Since $|\boldsymbol{k}|$ and $|\boldsymbol{k_s}|$ in the visible range of the spectrum are small compared to reciprocal lattice vectors, only elementary excitation with $|\boldsymbol{q}| \cong 0$ participates in the Raman process, i.e., only states close to the Brillouin zone centre can be observed. For forward scattering $|\boldsymbol{q}| = |\boldsymbol{k} - \boldsymbol{k_s}| \cong 0$ holds quite well. However, the Raman spectra of absorbing materials are mostly measured in backscattering geometry where the crystal momentum transfer is $|\boldsymbol{q}| \cong 2|\boldsymbol{k}| = 4\pi n(\lambda)/\lambda$ and depends on the refractive index $n(\lambda)$ and the laser wavelength λ. The value of $|\boldsymbol{q}|$ is still small, but the fact that it is nonzero is essential for some scattering mechanisms.

Symmetry properties of the interactions involved in a Raman process lead to selection rules which are conveniently summarized in a form of Raman tensors (solutions of the wave equations which do not cancel themselves) [12]. Adding these tensors to the electric field polarization vectors of incident and scattered photons yields the scattering intensity for a given configuration. For optic phonons in polar semiconductors like ZnSe, two

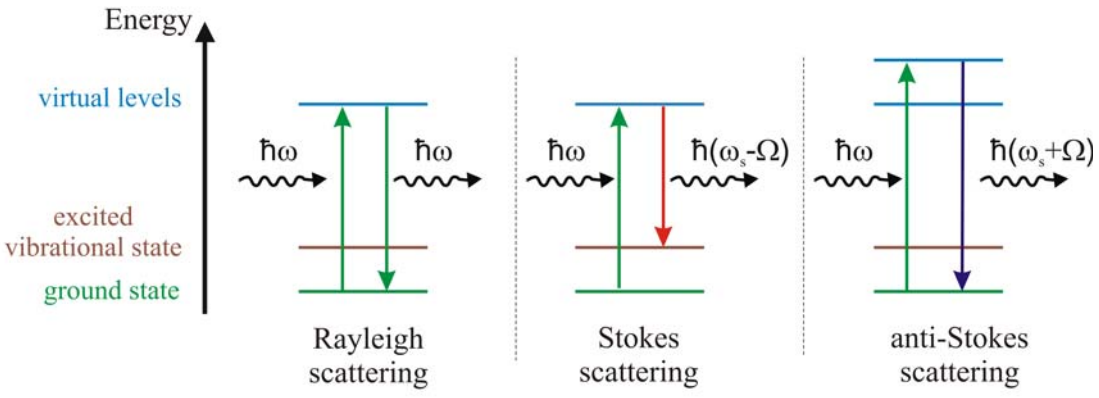

Figure 4. Sketch of the energy levels by Rayleigh scattering, Stokes and anti-Stokes Raman scattering. By Raman scattering the frequency of the irradiate light (green arrows) can be shifted to a lower (Stokes scattering, red arrow) or to a higher spectral range (anti-Stokes scattering, blue arrow).

mechanisms of electron-phonon coupling are important: a) the short-range deformation-potential coupling mediates scattering processes via the periodic modulation of the electronic structure caused by the relative sublattice displacement of the ions by the phonon; b) the long-range Fröhlich interaction has its origin in the macroscopic electric field, which in a polar semiconductor is connected with a longitudinal lattice vibration. Backscattering of longitudinal optical (LO) phonons form an [001]-oriented surface of, e.g., GaAs or ZnSe, is described by the following Raman tensor:

$$R_F = \begin{matrix} a_F & 0 & 0 \\ 0 & a_F & 0 \\ 0 & 0 & a_F \end{matrix}; \qquad \text{Eq. 6}$$

where a_F is the Raman polarizability. For polarization vectors $\hat{e}_l$ and $\hat{e}_s$ the Raman scattering intensity is proportional to

$$I \propto \left| \hat{e}_s * \mathrm{R}\hat{e}_l \right|^2 . \qquad \text{Eq. 7}$$

The change of strain as well as defects in the crystal affect the phonon frequencies. Accordingly the phonon frequencies give information about the lattice state. Thus Raman spectroscopy is a suitable technique for non-destructive characterization of the structural properties of semiconductor heterostructures.

Experimental setup. ZnSe/GaAs heterostructures were characterized by confocal μ-RS at room temperature in backscattering geometry $z(x,y,)\bar{z}$, where x = [100], y = [010] and z = [001]. Figure 5 shows the sketch of the μ-Raman setup. The sample was placed on a piezo-positioner that provides the lateral spatial resolution less than 500 nm. For the excitation two laser sources were used. The diode pumped solid state (DPSS) laser with 532 nm (2.33 eV) line and the cw laser with 473 nm (2.62 eV) radiation. An average excitation power of 0.5 mW was applied. The laser beam was collimated to 400 nm diameter by 100 x 0.7 NA objective. The scattered light was collected by the same objective and focused onto the 100 μm pinhole mounted at the entrance of the single-monochromator with a transmitting efficiency up to 70%. The monochromator was equipped with holographic grating yielding a spectral resolution of 5 cm^{-1} and with reflective diffraction grating with 1800 lines per mm yielding a spectral resolution of 1 cm^{-1}. Signal detection was performed by a cooled low-noise Andor CCD camera.

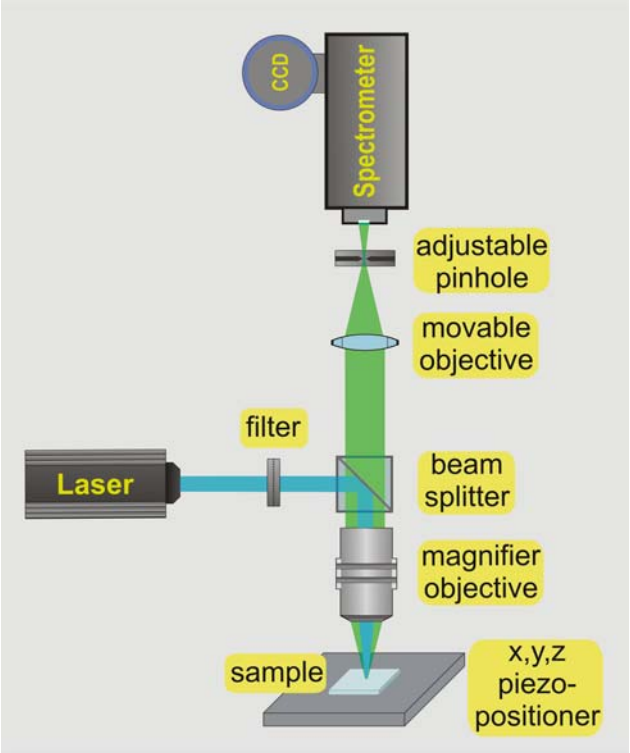

Figure 5. Sketch of the micro-Raman setup.

2.4 Photoluminescence spectroscopy

Photoluminescence (PL) spectroscopy is a contactless, nondestructive basic characterization method to investigate the electronic structure of materials. Light with an energy higher than the band gap of the excited material is directed onto a sample, where it is absorbed and it transfers excess energy into the material in a process called photo-excitation. This excess energy can be dissipated by the sample through the emission of light, or PL. The intensity and spectral content of this PL is a direct measure of various important material properties, such as band gap determination, impurity levels and defect detection, recombination mechanisms, and material quality.

Photo-excitation causes electrons within the material to move into allowed excited states. When these electrons return to their equilibrium states, the excess energy is released and may include the emission of light (a radiative process) or may not (a nonradiative process). The energy of the emitted light (PL) is the difference in energy levels between the two electron states involved in the transition between the excited state and the equilibrium state.

Through an excitation an exciton can be formed. When a photon enters a semiconductor, it may excite an electron from the valence band into the conduction band. The missing electron in the valence band leaves a hole (of opposite electric charge) to which the electron is attracted by the Coulomb force to form a quasiparticle. Since an exciton is an electron-hole pair, the overall charge is zero. The exciton results from the binding energy of the electron with its hole. Consequently, the exciton has slightly less energy than the unbound electron and hole. The wave function of the bound state follows that of the hydrogen atom.

A simple Hamiltonian to describe the exciton is:

$$H = H_0 + U \text{ with } U = -\frac{e^2}{4\pi\varepsilon\varepsilon_0(r_e - r_h)} \qquad \text{Eq. 8}$$

Where H_0 is the kinetic energy of the electron-hole pair in the centre of the mass frame (we neglect the centre of mass kinetic energy), U is the Coulomb attraction between the electron and hole, screened by the dielectric constant ε, and ε_0 is the permittivity of the vacuum. The Schrödinger equation $H\Psi = E\Psi$ has as eigenvalues a series of quasi-hydrogen states.

$$E_{exc,n_q} = -R_y \frac{m_r}{m_0} \frac{1}{\varepsilon^2 n_q^2} \qquad \text{Eq. 9}$$

where R_y = 20 meV is the Rydberg constant for the exciton in bulk ZnSe [13], m_r is the reduced exciton mass given by $m_r^{-1} = m_e^{-1} + m_p^{-1}$ for simple parabolic bands and n_q is the principal quantum number. The exciton radius is a quasi-hydrogen radius

$$a_{exc,n_q} = a_H \frac{\varepsilon}{m_r / m_0} n_q^2 \qquad \text{Eq. 10}$$

with

$$a_H = \frac{4\pi\varepsilon_0\hbar^2}{m_0 e^2} = 0.529 \text{ Å} \qquad \text{Eq. 11}$$

where a_H is the Bohr radius of the hydrogen atom. For ZnSe we obtain $E_{exc} \approx 21$ meV and $a_{exc} \approx 50$ Å [14].

Depending on the reduced exciton mass and the dielectric constant, we distinguish between Wannier-Mott excitons, which extend over many lattice constants, and Frenkel excitons, which have a radius comparable to the interatomic distance and resemble the atomic excited state. Frenkel excitons are observed in ionic crystals with relatively small dielectric constants, large effective masses and strong coupling with the lattice, as well as

in molecular crystals. These excitons, referred to be tight-binding excitons, show relatively large binding energies, usually in excess of 0.5 eV and cannot be described by a simple hydrogenic model. Wannier-Mott excitons are found in most of the typical semiconductors and extend over many lattice constants. The ionization energy of these excitons in typical semiconductors is in the order of 10 meV.

Donor-bound excitons. In II-VI like ZnSe, zinc (Zn) has two valence electrons while selenium (Se) has six. When a donator with seven valence electrons is incorporated, there is one extra valence electron in the neutral donor state which forms an s-like state localized at the donor impurity namely the so-called neutral donor state. A photon penetrating a semiconductor, in particular ZnSe, may excite an electron in the ground state into an excited state. An exciton bound to a neutral donor is formed if such a donor captures a free exciton (to complete its electronic configuration). As a result, the bound exciton has slightly less energy than the free exciton due to its binding energy to the donor. Eventually, the excited electron may drop back to its ground state via electron-hole recombination, emitting a photon. A single photon is expected to emerge out of such a recombination. The emission energy corresponds to:

$$E_{ph} = E_{g(ZnSe)} - E_{FX} - E_{DX} \qquad \text{Eq. 12}$$

E_{ph} is the emission energy while $E_{g(ZnSe)}$, E_{FX} , E_{DX} represent material bandgap, free-exciton and bound-exciton binding energy, respectively. This process is illustrated in Figure 6 referred to as the main transition. A two-electron transition or two-electron

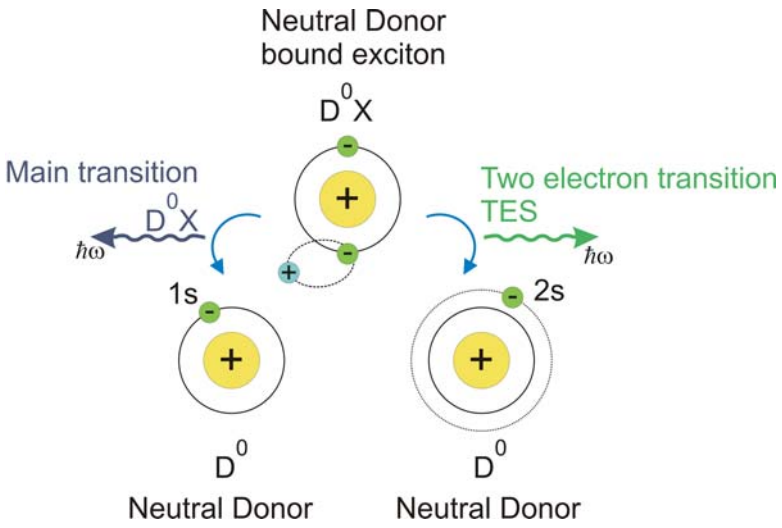

Figure 6. Neutral donor state and neutral donor-bound exciton state of F:ZnSe. A single photon emerges when the excited electron drops back to ground state. TES occurs when E_{ph} is partially absorbed to excite the remaining electron of the neutral donor.

satellite (TES) occurs when some of E_{ph} is absorbed to excite the remaining electron of the donor to the 2s or 2p state.

ZnSe has effective masses m_e^* and m_h^*, a static dielectric constant ε_0 and negligible electron-lattice coupling. The donor binding energy is given by:

$$E_D = \frac{\left(m_e^* / m_0\right)}{\varepsilon_0^2} R_y \qquad \text{Eq. 13}$$

According to Merz et al. [15], the estimated donor binding energy for fluorine is about 28 meV from experimental results. Excitons bound to neutral donors and acceptors have been observed in many systems and especially for II-VI semiconductors show a systematic trend is known as the Haynes rule:

$$E_{xnd} / E_D \equiv f\left(m_e^* / m_h^*\right) \qquad \text{Eq. 14}$$

where E_{xnd} represents the binding energy of an exciton bound to a neutral donor and E_D represents the donor binding energy i.e., fluorine binding energy to ZnSe. The remarkable features are that the exciton binding energy and donor binding energy remain proportional even when there are substantial central-cell corrections; the results seem valid beyond the Hynes model. For II-VI compounds $m_e^* / m_h^* \approx 0.25$ is typical, and experimental results suggest $f(0.25) \approx 0.2$ [16]. With the above approximation, we can calculate the exciton binding energy to a neutral fluorine donor:

$$E_{xnd} = E_D(F) \cdot f\left(m_e^* / m_h^*\right) \approx 6 \ \ meV \qquad \text{Eq. 15}$$

Energy states in a fluorine doped ZnSe quantum well. A quantum well is a potential well that confines particles to two dimensions perpendicular to the layer surface. Due to the confinement of carriers, the dispersion relation along the confinement direction is changed. The change in dispersion relation results in a change in the density of states. For a quantum well with a rectangular profile, the density of states is constant within certain energy intervals. A quantum well is often realized with a thin layer (typically between 1 and 10 nm thick) of a semiconductor medium, embedded between other semiconductor layers of a wider bandgap. If a quantum well is subject to strain, as can be caused by a slight lattice mismatch (for example ZnSe quantum well embedded in ZnMgSe: $a_{ZnMgSe} > a_{ZnSe}$), the electronic states are further modified. Induced strain into the crystal structure produces heavy hole (hh) and light hole (lh) splitting in the valence band.

Structures used in this work consist of layers with three different lattice parameters: GaAs substrate with a_{GaAs}=5.6533 Å [17], ZnMgSe barriers with about 9% Mg content with $a_{Zn_{0,91}Mg_{0,09}Se}$ = 5.6906 Å and ZnSe QW with a_{ZnSe} = 5.6676 Å [17]. On the GaAs substrate the ZnSe QW and the ZnMgSe barriers have a compressively strained lattice perpendicular to the surface. If the GaAs substrate is removed, the ZnSe QW is likely to be tensile strained on ZnMgSe, considering the volume ratio of ZnMgSe versus ZnSe. The lattice mismatch between substrate and layers is

$$m = \frac{a_{substrate} - a_{layer}}{a_{layer}} 100\% \qquad \text{Eq. 16}$$

For the ZnSe QW compressively strained on GaAs the lattice mismatch is -0.25% and for the ZnSe QW tensile strained on ZnMgSe m = 0.4%.

Figure 7 shows the sketch of the transitions in compressively and tensile strained ZnSe QWs with fluorine δ-doping in the middle. On the left side the transitions of the excitons in compressively strained QW and on the right side in the tensile strained QW are shown. The purple arrow represents the excitation energy. The black dotted line indicates quantized states in the QW, the blue dotted line donor states. Due to the splitting in the valence band to lh and hh four first order transitions can take part in the luminescence. For compressive strain of ZnSe QW hh transitions have a lower energy than lh transition of free exciton (FX) and neutral donor-bound exciton (D^0X). By the change of the compressive to the tensile strain in the ZnSe QW the lh position shifts strongly to the higher band energy so that the lh transition has a lower energy in comparison to the hh transition, where the

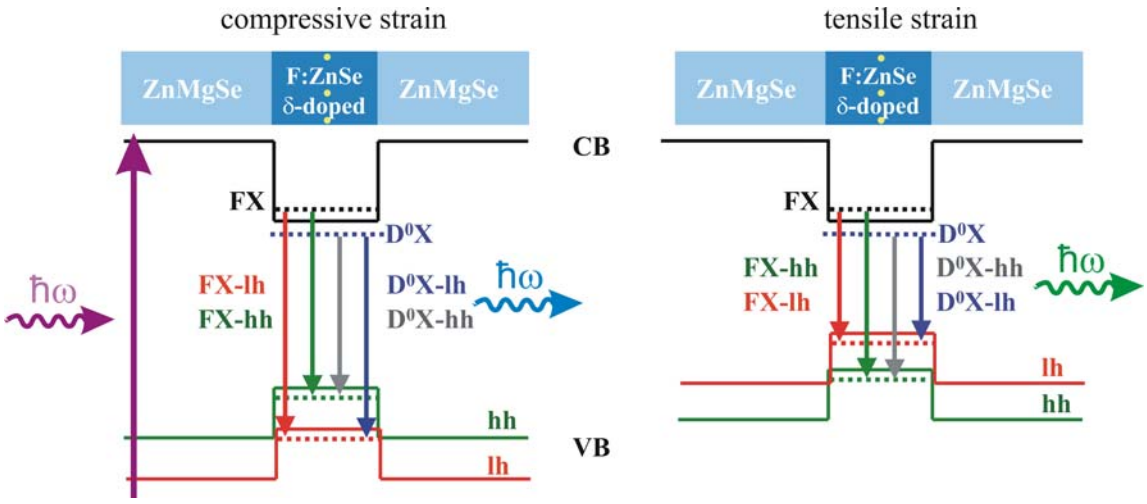

Figure 7 . Exciton transitions of a compressive and a tensile strained ZnSe/ZnMgSe QW.

position has a small shift in the band energy. For the compressively strained ZnSe QW the hh transitions have higher probability and the most emitting efficiency. In the tensile strained QW this relation is reversed and the lh transitions become stronger. However, both states and their corresponding D^0X-transitions contribute to the PL. In a δ-doped F:ZnSe QW an additional second order transition as the two electron transition (TES) occurs. The fluorine-donor binding energy amounts to ~5-6 meV [18]. The D^0X-TES binding energy averages to ~21 meV [19]. The transition is consistent with the finite barrier model in Refs. [20], [21].

Energy states in quantum dots. A QD is a semiconductor nanocrystal ranging typically from 2-10 nm (10-50 atoms) in diameter, which can confine electrons or other carriers in all three dimensions. The carrier confinement changes the density of states for the confined particles, compared with the density of states for structures in a bulk semiconductors. For an ideal, isolated quantum dot (zero dimensional system, 0D), there are discrete energy levels corresponding to a delta-shaped density of states with no states in between the delta peaks, analogous to the states of an atom.

In a QD the confinement potential affects the exciton additional to the Coulomb attraction. Due to the confinement, a higher overlap is generated in the wave functions of the electron and hole, and the Coulomb interaction is higher, which causes an increase of the exciton binding energy. Since it is practically impossible to have excited electrons and holes not bound to each other in the QD, it is difficult to acquire the experimental determination of the exciton binding energy. The accurate access to the exciton binding energy are numerical calculations. In this work, self-assembled CdSe QDs in a ZnSe matrix were used, which typically have a binding energy of about 20-25 meV [22]. Another implication of the confinement potential is the appearance of several-particle states, of which a few are shown in Figure 8. Figure 8 (a) shows an exciton ground state (X). In Figure 8 (b) electron and hole occupy a state in the p-shell and form the p-shell exciton (X_p). The biexciton (XX or 2X) shown in Figure 8 (c) consists of two

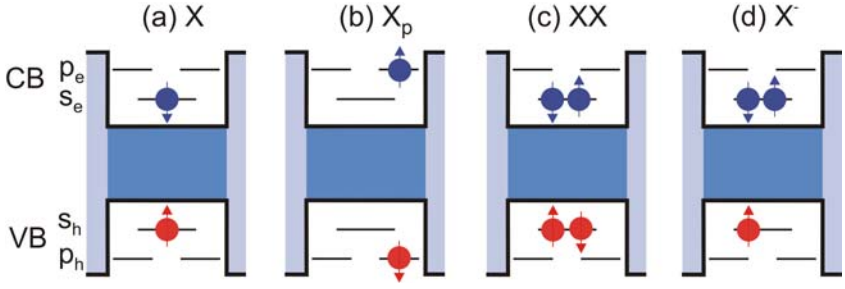

Figure 8. Schematic illustration of different QD occupations: (a) exciton (X), (b) p-shell exciton, (c) biexciton (XX), (d) single charged exciton (X^-).

excitons and two holes confined in the QD as s-shell is two-fold spin degenerated. When confining additional electrons into the QD (d), the exciton-electron complex is called negatively charged exciton (X^-). Finally, in the QD the excitons can recombine radiatively without participation of the other processes.

A precise theoretical calculation of the energy states is difficult due to the varying geometry of the QDs and the potential barriers. However, a tight-binding model can be used to calculate the energy levels of quantum dots as shown by Grünberg for CdSe QDs [23]. For the hole states, it has to be taken into account that the valence bands of the light and heavy holes are degenerated at the Γ-point of the Brillouin zone in a bulk semiconductor. For lower energy levels of the QD, only the heavy holes are relevant, because the quantization energy depends on the effective mass.

Experimental setup. PL spectroscopy is based on the principle of excitation of charge carriers by light and their subsequent relaxation into the lowest states. The light resulting from the recombination of electron and hole is analyzed with a spectrometer. Basically all PL experiments described in this thesis require a high spatial resolution and a low temperature. The basic experimental setup is shown in Figure 9. The setup was mounted on a breadboard for flexible mounting of different optical components. For the characterization, the samples were placed in a low-temperature cryostat cooled by liquid

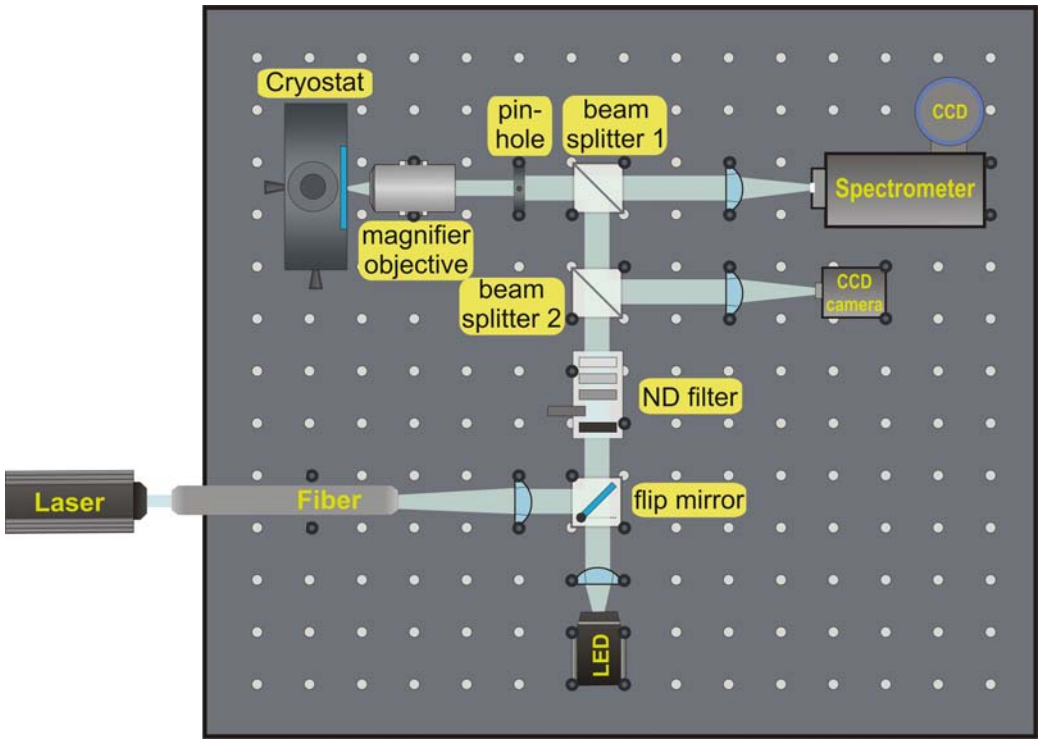

Figure 9 . Basic setup for the micro-PL measurements.

helium (temperature T = 4.2 K). The laser excitation was steered in a free space setup to the sample holder. First, laser light was coupled into an optical fiber and then made parallel through a lens, then reflected by 45° by a flip mirror. The intensity of the excitation was adjusted to the appropriate level by different neutral density filters. Next the laser beam passes beam splitter 2 with 45° 50/50 refraction and beam splitter 1 with 45° 90/90 refraction. The beam splitter 1 crystal structure is aligned in such a way that it reflects 90% of the incoming intensity for wavelengths less than 400 nm, while it transmits 90% of the intensity for wavelengths higher than 400 nm. To decrease the beam cross-section a pinhole was used. The emitted luminescence of the sample was transmitted through beam splitter 1 and focused onto the spectrometer.

The collected luminescence of the sample was dispersed by a spectrometer and detected by a multi-channel camera. The Acton spectrometer had a focal length f_L of 150 mm and at least two different diffraction gratings (g = 2400 1/mm and g = 600 1/mm, both blazed at 500 nm). A liquid nitrogen cooled silicon charge coupled device (CCD) was mounted on the spectrometer. The CCD camera can detect light with wavelengths from 200 nm up to 700 nm. The maximum spectral resolution of the setup was determined by the spectrometer geometry, the slit width of the spectrometer entrance, the dispersion of the grating used in the spectrometer, the pixel size of the CCD-camera and the central wavelength. The maximum resolution which could be achieved was 280 μeV.

An imaging unit allowed to monitor the sample on a monitor. This made it relatively easy to position the structure under the microscope objective. Thereby the sample was illuminated by the LED, whereas the flip mirror was revolved and the LED light was focused onto the sample. The focus spot could be varied by the pinhole up to maximal value of 40 μm. The reflected light from the sample was steered through both beam splitters and detected by the CCD camera.

For a basic characterization of the semiconductors the excitation energy has to be higher than the bandgap of the material. In this work several exitation sources were used:

- For the excitation of the ZnSe layers and the CdSe QDs a semiconductor laser diode with a wavelength of 404 nm (3.07 eV) or 365 nm (3.4 eV), was used as excitation source. The laser excitation could be focused down to a spot size of about 1 μm onto the structures by a NA = 0.75 microscope objective, which also collected the PL in a confocal geometry.
- Lasing of single MDs was excited using pulsed excitation by a frequency doubled mode-locked Ti:Sapphire laser operated at 409 nm wavelength (3.03 eV) with a pulse

repetition rate of 82 MHz and a pulse width of 1.5 ps. The FWHM diameter of the focused laser spot on the sample was about 15 μm. The excitation occurred under an angle of 30° to the disk surface and the PL emission was collected in the direction of 45° to the disk surface.

- For the resonant and tunable excitation of the CdSe QDs between 515 nm and 560 nm (2.4 eV and 2.21 eV, respectively) a laser pumped optical parametric oscillator (OPO) was used. The laser pulses had a repetition frequency of 160 MHz, a temporal width of about 3 ps and a spectral width of about 3 meV. The laser excitation could be focused down to a spot size of about 1 μm in a confocal geometry.

3 Low-Threshold ZnSe Microdisk Laser

For applications like lasing without inversion [24], electromagnetically induced transparency [25] and optically addressable quantum memory for quantum information processing [26 - 31], quantum interference of the two optical pathways of an optical Λ-system provides a powerful mechanism. In semiconductors, donor impurities and charged quantum dots provide promising realizations of a Λ-system, in which two long-living ground states are optically coupled to a single excited state. The long-lived ground states are provided by the bound electron spin in a high magnetic field, while the optically excited state is formed by the lowest energy donor-bound exciton or trion state. For applications involving quantum memories, however, quantum dots have the disadvantage of severe inhomogeneity in optical transition frequencies and electron magnetic moments. Such inhomogeneity may prevent the ability to incorporate many optically interacting QD-based Λ–systems into a scalable quantum-information processing device. In contrast, the potential provided by the donor impurities in a perfect crystal are very homogeneous, as demonstrated by high-quality samples of GaAs [32] and Si [33]. Homogeneous ensembles of donor-bound excitons in bulk GaAs have been demonstrated to exhibit coherent population trapping [34], which is one effect that exhibits quantum coherence between the two emission pathways of the optical Λ–system.

Donor-bound excitons in ZnSe are of particular interest because ZnSe may be isotopically purified to feature only spin-0 substrate nuclei, thus avoiding the disadvantage of decoherence limited by the dynamics of nuclear spins in III–V semiconductor systems [35]. Silicon-based systems also have the potential to overcome nuclear decoherence [36], but silicon is optically dark due to its indirect band gap. Hence, in ZnSe the nuclear spins may be entirely removed from the substrate as in the case of silicon, and the donor-bound-exciton emission is optically bright as in the case of GaAs. The fluorine (^{19}F) donor in ZnSe is of particular interest because it provides a 100% abundant spin-1/2 nucleus, which may be employed for long-living storage of quantum information.

For these reasons, lasing in ZnSe donor-bound excitons may be particularly useful as a component in quantum information processing devices. The design of quantum computers [30] or quantum repeaters [31] based on donor-bound excitons in optical microcavities requires a low-noise laser source nearly resonant with the bound-exciton transitions used for qubit initialization, control, and readout. A laser based on the same medium as the qubit provides promising pathways for device integration.

The first step towards the realization of such laser devices is a microdisk (MD) resonator. MD lasers consist of a thin disk on a pedestal. The main features of such lasers are ultra low thresholds, periodically spaced frequencies of lasing, and predominant in-plane light emission. The lasing modes are optical whispering gallery modes (WGM) confined by total internal reflection at the interfaces of the disk [37] – this explains the periodicity of lasing frequencies within the PL band. In MD resonators the overlap between the small volume gain region with WGMs enables a very efficient coupling of spontaneous emission into the lasing mode, thus offering a high potential to obtain lasing with low thresholds and predominantly in-plane light emission. Furthermore, MD lasers are easier to fabricate in comparison to other low-threshold semiconductor laser types like vertical-cavity surface-emitting lasers (VCSEL), micro-post lasers, and photonic crystal lasers.

Due to these advantageous properties, MD resonators have been applied to a large variety of active materials. Disk-shaped microresonators represent a versatile platform for testing laser gain materials, whether bulk materials [38], quantum wells [37, 39] or subwavelength small structures such as quantum dots [40, 41] or optical dopants [42].

Semiconductor lasers in the form of thin disks on pedestals were first demonstrated successfully in the early 1990s as extremely compact sources of light [37, 43, 44]. These disks, usually 1–10 μm in diameter and 100–300 nm in thickness, were made of GaAs and contained one 5–10 nm thick GaAs/AlGaAs or GaAs/InP quantum wells (QW) as an active region to provide the emission wavelength around 1550 nm. Next, the single QW as an active region was upgraded to cascaded multiple-QW structures [45, 46, 47]. As manufacturing technologies such as lithography, wet and dry etching, epitaxial growth and thin-film deposition developed quickly, the QWs were replaced by layers of randomly grown quantum boxes [48] and quantum dots (QDs) [40, 41]. A QD-based active region has advantages over a QW one, offering less dependence on temperature and a distinct density of states which allows for nearly threshold-less lasers. In addition, these factors are important for achieving single-mode laser operation. New active material systems have

also been tried to cover wavelength bands from infrared to ultraviolet [38, 49, 50]: GaInP/InP (650 nm), ZnSe/CdS (510 nm), ZnO/SiO_2 (390 nm), and InGaN/GaN (370 nm). On the other hand, cascading of the 20–30 periods of three-QW active regions has enabled researchers to design microcavity lasers with emission wavelengths as long as λ=5μm [46], λ=10μm [51] and longer [52]. The first experiments with new materials were performed with optical pumping and at cryogenic temperatures. By refining the technologies, the next step was usually to achieve continuous-wave room-temperature lasing and demonstrate a device with current injection [53 - 57]. Injection lasers, however, immediately revealed that the proper placement of electrodes plays a crucial role in their performance.

Today's trends in microcavity lasers are associated with refining the smoothness of the cavity, optimising the shape of the pumped area, building arrays of MDs, and shrinking the active zone to a single QD.

In the blue region ($\lambda \approx 440$ nm) lasing is traditionally difficult to obtain. ZnSe is a wide-bandgap semiconductor which emits light in this region. Early studies of lasing in ZnSe for the purpose of blue lasers were limited because the material is too soft to be used in high-current or high-excitation regimes so that heating effects degenerate the active medium [58, 59]. However, low-threshold lasing is achievable in MD structures, where a high-Q, low-volume optical microcavity introduces a high ratio of stimulated emission to spontaneous emission, known as the β-factor [60]. Previous work on lasers in wide-bandgap II–VI semiconductors has focused on lasers based on CdSe QDs [61, 62] or ZnCdSe QWs [43] confined by quaternary alloys of ZnMgSSe and ZnCdSSe, which are lattice-matched to a GaAs substrate. However, their quaternary composition results in alloy fluctuations, which have substantial impact on the optical properties (increased linewidth) of the lasing devices. Alternatively, with strained ZnSe QW enclosed in ternary ZnMgSe layers with low Mg concentration, the alloy fluctuations can be minimized. Hence in this work, a MD resonator containing a fluorine δ-doped ZnSe layer at the centre of the QW was proposed and developed. Optical and structural properties of the microresonators were investigated. Finally, low-threshold lasing on discrete, bound-exciton transitions of such MDs was observed.

3.1 Basics of microdisk laser

The intention of this chapter is to give a brief overview about semiconductor lasing and associated parameters to define the basic terms used throughout this thesis.

Semiconductor laser fundamentals are shown in Figure 10. (a) "Pumping" energy into a semiconductor can excite an electron into the conduction band. That electron leaves behind a hole in the normally filled valence band, and thus an e-h pair is created. The electron and hole each relax to the respective band-edge states by nonradiative processes. During the band-edge transition, a photon is emitted as the excited electron spontaneously recombines with the hole. (b) Stimulated emission occurs when a photon induces the excited electron to decay. The emitted photon has the exact frequency, phase, and polarization of the initial photon. (c) For a ground state that contains two electrons, exciting only one electron (population equality) can lead to two equally probable outcomes: the photon excites the ground-state electron and is absorbed (left), or the incoming photon stimulates the excited electron to decay, producing an extra photon (right). There is no net gain or loss of photons. In this case, the medium is in the transparency regime. (d) Optical gain can occur if there are more electrons in the excited state than in the ground state (population inversion) because photon absorption is inhibited. If a population inversion is established in a system and if the gain from stimulated emission is larger than losses that absorb or scatter photons, the system will exhibit amplified spontaneous emission.

The spontaneous emission *factor* β is the fraction of the total spontaneous radiative decay that couples into the lasing mode, both spatially and spectrally and is defined as

$$\beta \equiv A_0 \Big/ \sum_i A_i \qquad \text{Eq. 17}$$

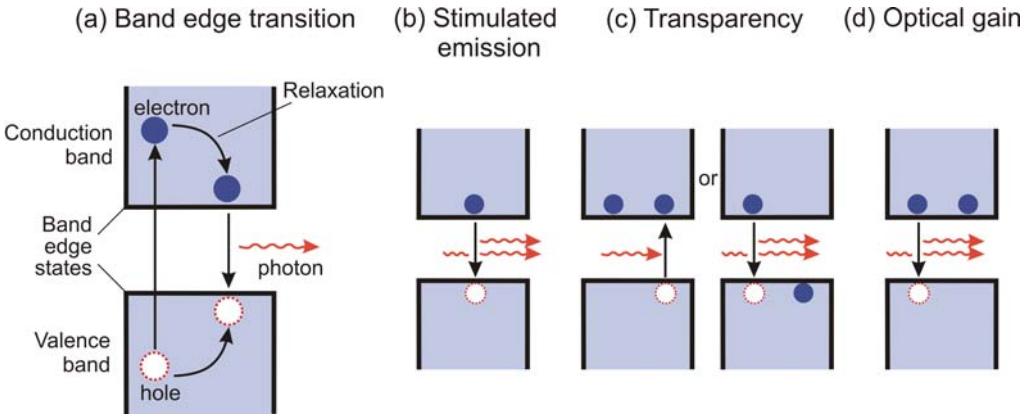

Figure 10. Semiconductor laser basics

where A is the spontaneous emission rate of the active material into a mode i, index 0 indicates the optical mode which will eventually provide stimulated emission.

The *quality factor* (Q factor) of a resonator is a measure of the strength of the damping of its oscillations, or for the relative linewidth. There are two common definitions of the Q factor of a resonator:

- Definition via energy storage: the Q factor is 2π times the ratio of the stored energy to the energy dissipated per oscillation cycle, or similarly the ratio of the stored energy to the energy dissipated per radian of the oscillation. For an optical resonator, one oscillation cycle is understood as corresponding to the field oscillation period, not to the round-trip period. The Q factor of a resonator depends on the optical frequency ω_0, the fractional power loss per round trip l and the oscillation period T:

$$Q = \omega_0 T \frac{2\pi}{l} \qquad \text{Eq. 18}$$

- Definition via resonance bandwidth: the Q factor is the ratio of the resonance frequency ω_0 and the full width at half-maximum (FWHM) bandwidth $\delta\omega$ of the resonance:

$$Q \equiv \omega_0 \big/ \delta\omega \qquad \text{Eq. 19}$$

Both definitions are equivalent only in the limit of weakly damped oscillations, i.e. for high Q values.

The enhanced radiative rate of an emitter within a microcavity relative to its value in free space is the *Purcell factor*. The total transition rate of an emitter depends on the density of states of the ambient electromagnetic field. The photonic density of states of a free space is given as

$$D_f(\omega) = \frac{\omega^2}{\pi^2 c^3} \qquad \text{Eq. 20}$$

By assuming a cavity with a single mode, that has the spectral width $\Delta\omega$ and is limited to the volume V_{cav}, the photonic density of states can be described by

$$D_{cav}(\omega) = \frac{2}{\Delta\omega V_{cav}} = \frac{2Q}{\omega V_{cav}} \qquad \text{Eq. 21}$$

Thereby we assume that the emitter and the cavity are in resonance and the spectral width of the cavity is higher than that of the emitter. The ratio of both these states D_{cav} and D_f gives the Purcell factor [63]:

$$\frac{D_{cav}(\omega)}{D_f(\omega)} = \frac{3Q\pi^2 c^3}{\omega^3 V_{cav}}\eta = \frac{3\left(\lambda/n\right)^3 Q}{4\pi^2\ V_{cav}}\eta = f_p \qquad \text{Eq. 22}$$

where the factor of 3 stems from 1/3 averaging factor accounting for the random polarization of free space modes, n is the refractive index of the medium and η is a factor that takes into account the various nonidealities. Whereas the first term is only related to cavity properties (Q, V_{cav}), the latter (η) (which is always smaller than 1) depends on the emitter/mode spectral detuning, on the relative field amplitude at the emitter's location and on the orientation matching of the transition dipole and electric field.

In order to find a figure of merit for the cavity alone, it is convenient to consider the spontaneous emission rate enhancement for an "ideal" emitter, whose properties allow to maximize the magnitude of the Purcell effect. This ideal emitter should be: 1) perfectly matched spectrally with the cavity mode, 2) located at a maximum of the electric field, and 3) with its dipole aligned with the local electric field. So, for the enhancement of the transition rate, a higher Q value or a smaller mode volume is required. This simple description shows that the emission rate depends not only on the emitting system, but also on the density of the photonic states. If the spontaneous emission into the lasing mode is enhanced by the Purcell factor f_p, the β factor is increased. As a consequence, lasers with large β factors represent an ultimate goal as they have small thresholds. In the theoretical limit of $f_p \rightarrow \infty$ the β factor can approach unity. This would describe a thresholdless laser with a quantum efficiency of 100%.

The high index contrast ratio between the disk (e.g. ZnSe with n ≈ 2.8) and its surroundings (e.g. air with n = 1) is a key feature of the design of MD lasers because it strongly confines the active optical modes to the plane of the disk. Hence, MDs confine the light in the periphery of the disk by total internal reflection. The high index contrast ratio enhances the high reflectivity and mode selectivity of the microcavity. Optical modes occur at the edge of a thin semiconductor dielectric disk, similar to WGMs [64].

In transverse electric (TE) or H-modes, the electric field is perpendicular and the magnetic field is in propagation direction. In transverse magnetic (TM) or E-modes, the magnetic field is perpendicular but the electric field is parallel to propagation direction. A major fraction of the mode overlaps with the gain region layer thus providing the lasing effect.

The disk radii, height and material dependent resonance frequencies are crucial for the MD design. To optimize the parameters, calculations had to be carried out in order to

enhance the lasing effect. Several approaches can be used to calculate the energetic position of the WGMs and the corresponding field distributions in MDs. It is possible to solve Maxwell's equation with appropriate boundary conditions for a two-dimensional MD [65]. The resulting expression is the scalar wave equation for propagation in a dielectric medium, also known as the Helmholtz equation, with an approximated solution including Bessel functions. However, the third dimension and the electric field at the boundary of the disk is neglected. In order to calculate the resonances of a three-dimensional MD, the MD with a certain height is treated as a coplanar resonator. For this task most commonly the analytical method of effective refractive index n_{eff} is used to estimate the eigenfrequencies and the modal field distribution. A new quantity n_{eff} can be introduced analogous to an approach proposed by Slusher et al. [66], which represents the coplanar resonator properties of a MD. According to Slusher et al., the MD is basically separated into a coplanar resonator and a two-dimensional ring resonator. The quantity n_{eff} can be incorporated into the calculation of the ring resonator which then yields solutions for a quasi-three dimensional model of the MD modes. However, it has been shown experimentally that this often used method can fail for the description of thin three-dimensional dielectric disk resonators: Within a high accuracy experiment at microwave frequencies (radius 274.8 mm), the resulting eigenmodes do not agree with the experimental results [67].

For the calculations of our MDs computational methods were used that are feasible to gain information about the resonances in flat dielectric disks, based on a three-dimensional discretization with the Finite Integration Technique (FIT). Both time domain and frequency domain approaches were applied. The simulations were carried out by Christoph Claßen from the group of Prof. R. Schuhmann of department of theoretical electrical engineering.

3.2 Fabrication of microdisks

Semiconductors can be formed into optical microresonators using photolithographic techniques. The fabrication process of the devices consists of several steps. The first step of the device fabrication is the deposition of the ZnSe and ZnMgSe layers on a GaAs substrate by MBE. Next, the semiconductor surface is cleaned and structured using photolithography to define round structures. Then, using dry plasma etching, the

photoresist pattering is transferred into the layers. Selective wet chemical etching is used to undercut the structures. In this section the fabrication procedure for ZnSe MDs is outlined in detail.

3.2.1. Growth procedure of quantum well structures

Preparation and growth of GaAs. The industrial fabricated n-doped (2×10^{18} cm^{-3}) (001) GaAs substrates with a size of 10×10 mm^2 were glued onto a molybdenum substrate holder with a compound of indium and gallium, which remains liquid at room temperature. The substrate was transferred into the III-V-GaAs MBE chamber through a load lock chamber (s. Figure 1). Within an arsenic atmosphere (~2×10^{-6} mtorr), the temperature of the substrate was slowly increased to remove the epiready layer and oxide from the substrate surface. When the reflexes of the GaAs crystal surface were visible by RHEED under all azimuth angles, the Ga cell was opened and the growth of GaAs was started. The stoichiometry of the growth front and the thickness of the GaAs layer were checked by RHEED. Afterwards the growth of GaAs was stopped by closing the Ga shutter. In most experiments ~ 150 nm of GaAs were deposited. The substrate heater was turned off and the sample was cooled down under arsenic overpressure. Then the sample was transferred under UHV-conditions into the II-VI MBE system.

Growth of ZnSe/ZnMgSe quantum wells. Before the substrate was transferred into the II-VI system, the chamber was “floated” with zinc to reduce the selenium surplus in the remaining atmosphere in the system. This prevents the spontaneous formation of Ga_2Se_3, which has a hexagonal structure and ruins the cubic two-dimensional growth of ZnSe.

The sample was heated until it reached the growth temperature of about 290°C. The procedure of ZnSe growth was started first by a 10 s zinc deposition to increase the amount of zinc on the sample surface and reducing the possibility to form Ga_2Se_3. For the next 10 s, the sample remained in a vacuum with all cells closed. Afterwards, both the zinc and the selenium cells were opened simultaneously to start the growth of ZnSe. The ZnSe layers were grown at selenium excess with zinc to selenium flux ratio of 1:3 (Se flux ~1.4×10^{-6} mtorr). The complete sample structure is shown in Figure 11. Firstly, for optimal interface properties, 20 nm of ZnSe-buffer were grown. For the 30 nm thick $Zn_{1-x}Mg_xSe$ barriers with 8-9% magnesium content and the 10 nm thick ZnSe QW, phase-lock (PLE) and migration enhanced epitaxy (MEE) methods were used in order to fabricate the QW with minimal interface fluctuations. In the centre of the QW a monolayer of fluorine was

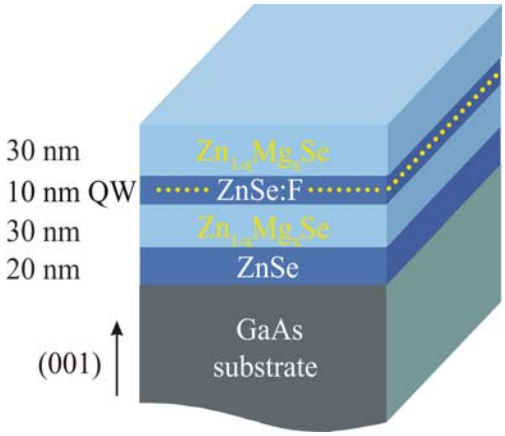

Figure 11. ZnSe/ZnMgSe QW structure with fluorine δ-doping in the middle on a GaAs substrate.

deposited to define the delta doping, whereas the zinc fluoride cell was opened for 1-2 seconds in the middle of the QW growth. From the given ZnF_2 flux and by capacitance-voltage measurements, the concentration of the F-atoms was estimated to be about 500 F-atoms/monolayer (ML) in 1 μm^2.

The crystal growth was monitored by RHEED in [-110]-azimuth. The RHEED-oscillations of the intensity of the specular spot of the ZnSe layer were measured and used for the calculation of the growth rate of ZnSe. Figure 12 shows the RHEED pattern in [-110] direction of a typical ZnMgSe surface at 290°C under Se overpressure at the end of the growth. The surface is two-dimensional as can be seen from the streaky diffraction pattern of the electron beam on the surface under the shadow edge. The streaks and the specular spot are indicated. The distance between the (-10) and (10) streaks in the RHEED 2D pattern is related to the in-plane lattice parameter of the layer. During growth the distance between the streaks did not change: the layers grew pseudomorphically or the

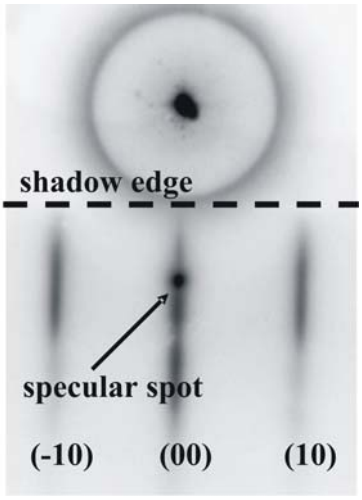

Figure 12. RHEED pattern of a ZnMgSe surface at the end of the growth.

relaxation was below the detection limit. The lattice mismatch between ZnSe and $Zn_{0.92}Mg_{0.08}Se$ to GaAs is 0.25% and 0.64%, respectively. Thus, ZnSe relaxes when the critical layer thickness of about 200 nm [68] is exceeded. The overall grown layer thickness of 90 nm is below the critical thickness and the ZnSe/ZnMgSe layers are supposed to be strained on GaAs. However, RHEED measurements give only information about the surface quality of the epitaxial layers.

The crystalline morphology of the films and the composition of the $Zn_{1-x}Mg_xSe$ layers was determined by means of ex-situ HRXRD. Figure 13 shows the typical rocking curve of the (004)-reflex of ZnSe in a similar QW structure as the one described above. The spectrum was fitted by a Gaussian function. The full width of half maximum (FWHM) of this sample was about 8 arcsec. By using Eq. 3 a defect density in the ZnSe layer of $1x10^5$ cm^{-3} was determined from the FWHM of the rocking curve in Figure 13. However, the FWHM of the rocking curve is close to the resolution limit of the equipment, thus the defect density in the layers could be even lower.

The strain status and the chemical composition of the crystal were observed from the reciprocal space map (RSM). Figure 14 shows the HRXRD asymmetric RSM of the (224) reflex of a typical ZnSe/$Zn_{1-x}Mg_xSe$ QW on GaAs. The reflexes plotted in the figure correspond to the GaAs (lattice parameter a_0=0.5653 nm [17]) substrate, the ZnSe (a_0=0.5668 nm [17]) and the $Zn_{1-x}Mg_xSe$ layers. Between these peaks the fringes of the multilayers were detected. The fringes indicate excellent interface quality between $Zn_{1-x}Mg_xSe$ barriers and ZnSe QW. In addition, the position of the Bragg reflexes of strained

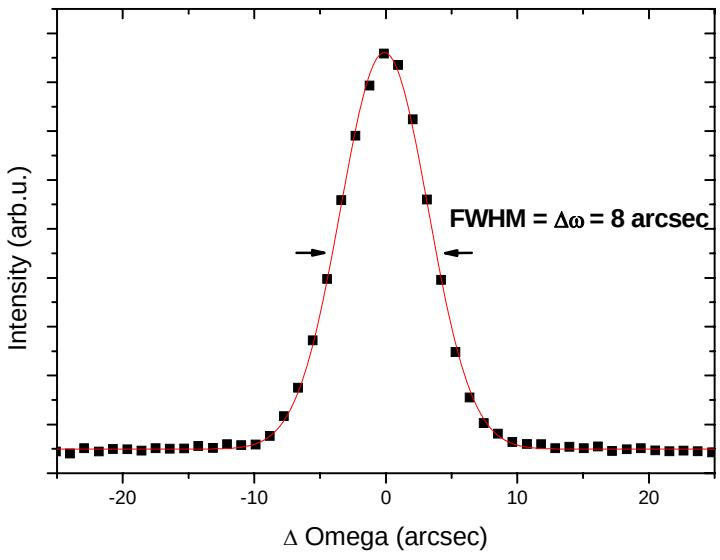

Figure 13. Typical rocking curve of strained ZnSe on GaAs.

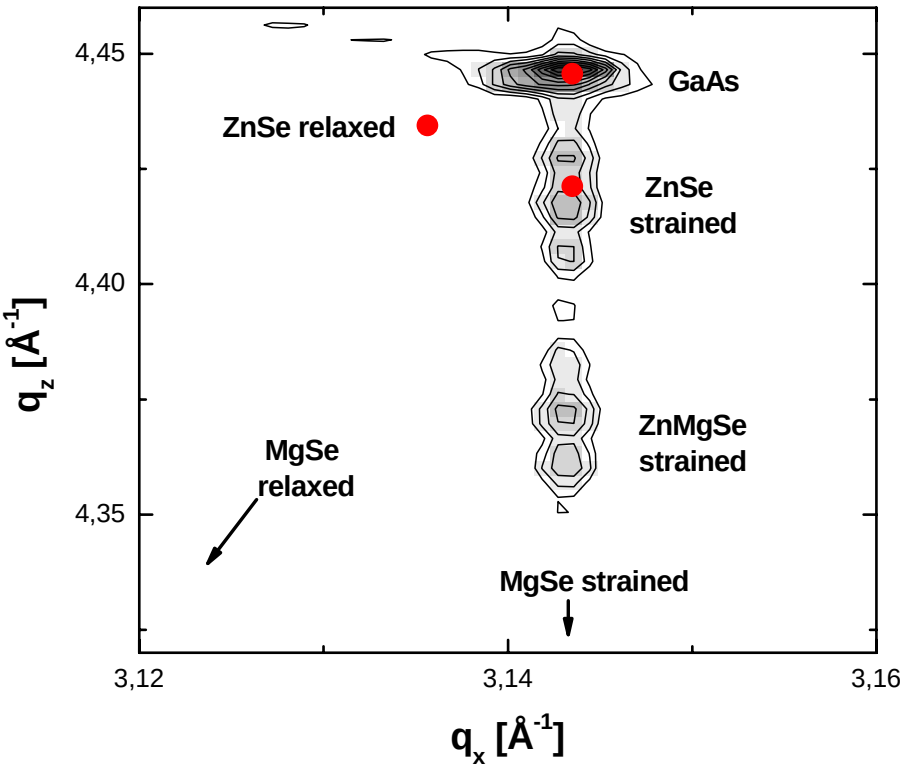

Figure 14. Reciprocal space map around the (224) reflex of an ZnSe/ZnMgSe films on GaAs. Red spots indicate the theoretical positions of the Bragg reflexes.

and relaxed ZnSe and MgSe (a_0=0.589 nm [69]) are indicated. The position of the ZnSe and $Zn_{1-x}Mg_xSe$ reflexes relative to the GaAs reflex shows that the layers are pseudomorphically strained on the GaAs substrate. Furthermore, the composition of $Zn_{1-x}Mg_xSe$ in our samples was determined from the RSM to the Mg mole fraction of about 8-9%.

3.2.2. Photolithography

Photolithography was performed to define round structures with diameters between 1 and 10 µm. Figure 15 a) and b) show the process schematically. First the surface of the sample was cleaned on the spinner by acetone and isopropanol at room temperature, followed by nitrogen gas drying. Photoresist AR-P 3510 diluted by AR 300-12 diluter with 1:1 ratio was then immediately dropped on the sample and spin-coated on the spinner with 6000 rotations per minute (rpm) for 30 s. Finally, it was post-baked on a hotplate at 100°C for 60 s. Inhomogeneous distribution of the resist appeared at the periphery of the sample. Therefore the sample edges were first exposed by the UV-light of a Hg-vapour discharge lamp (wavelength 365 nm) for 30 s, and then dissolved for 30 s in a solution of AR 300-15

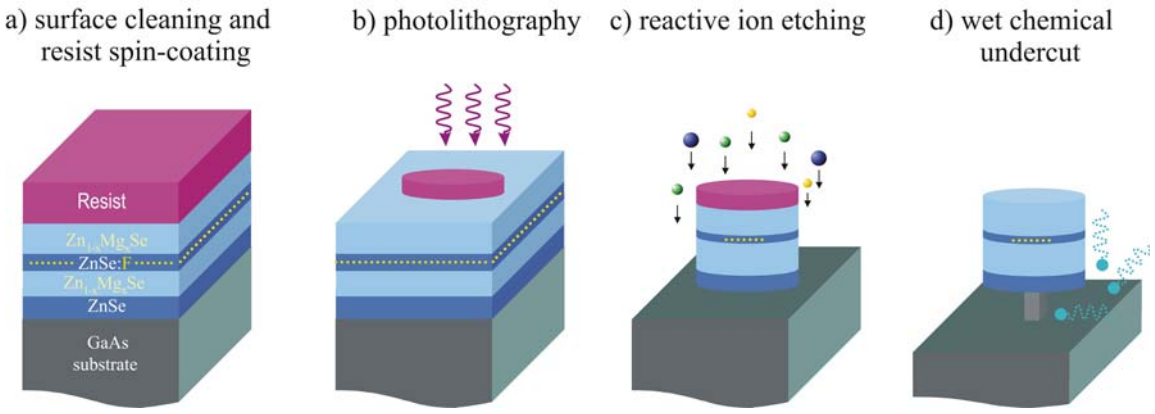

Figure 15. Fabrication steps of the MD device.

developer and deionized-water (DI-H_2O) with ratio 1:4 at room temperature. The DI-H_2O was used as a stop-bath to neutralize the developing reaction. The photomask with microcircle structures was cleaned by acetone, 3% Ticopur and DI-H_2O, followed by nitrogen gas drying. For the exposure, the photomask was in direct contact (so-called hard contact) with the photoresist. The illumination time was 8 s. The round structures were developed in the same developer solution of AR 300-15 developer and deionized-water (DI-H_2O) for 12 s and fixed in the DI-H_2O stop-bath. The thickness of the resist was measured by Alpha-Step and amounts to 500 ± 20 nm.

3.2.3. Reactive ion etching

To transfer the photoresist pattern into the layers reactive ion plasma etching (RIE) was used as shown in Figure 15 c). To define vertical sidewalls anisotropic material removal is possible by RIE. For the etching process gas mixtures of hydrogen (H_2), methane (CH_4) and argon (Ar) were used with typical flow rates of 59.5, 17 and 17 standard cubic centimeter per minute (sccm), respectively. The total chamber pressure was maintained at 35 mTorr, the RF power was 150 W. The etch rate of ZnSe was calculated to 10 nm/min and for diluted AR-P 3510 photoresist to 30 nm/min. To make sure that the multilayers were etched off, the etching was extended to 15 min. An acetone bath and spray were used to remove photoresist residuals.

3.2.4. Wet chemical undercut

Once the mesa structure was fabricated by plasma etching, the undercut could be performed. To undercut the pillar-like structure selective isotropic wet chemical etching

was required as shown in Figure 15 d). For GaAs wet etching a mixture of 41 ml 1M sodium hydroxide (NaOH) and 9 ml 30% peroxide (H_2O_2) solution was used. This solution was kept at 500 rpm at room temperature for 5 min to stabilize the reaction. Afterwards the rotation speed was decreased to 200 rpm and the patterned sample was immersioned into the solution. The etch rate of GaAs was about 50 nm/s in (001), (010) and (100) directions. To undercut a pillar with 3 µm diameter, for example, the sample had to be etched 30 s to define a MD on a 1.5 µm GaAs post.

3.2.5. SEM analysis

To investigate the defined structures in detail, scanning electron microscopy (SEM) analysis of the fabricated structures was performed. Figure 16 a) shows the SEM photographs of an array of MDs of 3 µm in diameter. The disk arrays with other diameters look similar. The majority of the disks is undamaged. The raster with markers and letter-number denotation (not shown here) was defined together with the disks to be able to

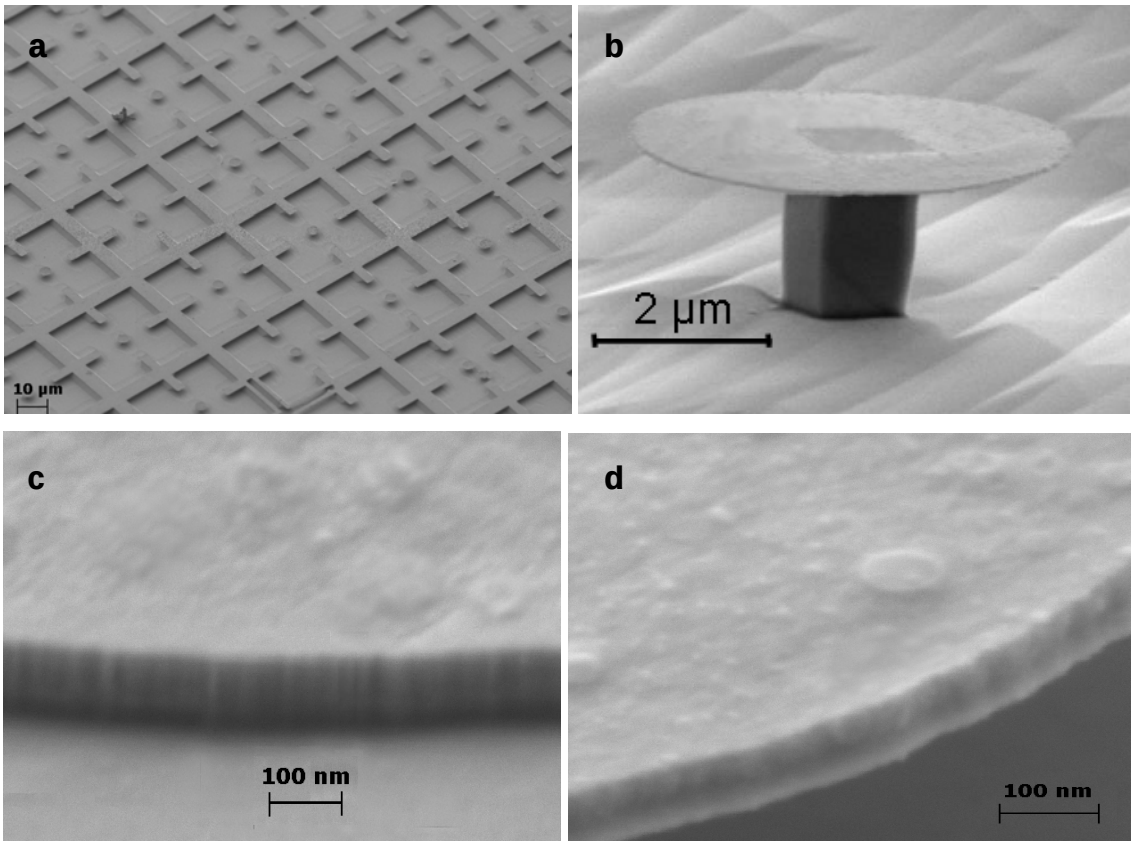

Figure 16. SEM photograph of a) an array of 3 µm MDs, b) a typical MD with 4.5 µm diameter, c) MD sidewalls and the surface after the RIE process and d) after the undercut.

identify the individual disks. Figure 16 b) shows a typical MD of 4.5 μm in diameter. The disk plane consists of ZnSe/ZnMgSe layers and the post under the disk is GaAs. The GaAs post is square shaped due to the selective etching properties of the peroxide solution in the [110] and [-110] crystal orientation. Furthermore, the post has a darker contrast in comparison to the disk due to the fact that the GaAs was n-doped and has a higher conductivity than undoped ZnSe/ZnMgSe layers. Hence, the post could be discharged better. The disk was charged by an electron beam and therefore has a brighter contrast. In most disks no lateral deformation and cracks were observed. The study of the diameter of MDs with different sizes has shown that the MD diameter fluctuations average 2-3%.

Figure 16 c) and d) show the SEM photographs of MD sidewalls and the MD surface after the RIE process and after the undercut. At the end of these processes the surface of the MDs has a low roughness. The sidewall of the disk after the RIE process appears to have some small ridges. After the wet chemical undercut the ridges on the sidewall are smoothed. The low roughness of the MD sidewalls and surface is an advantage concerning the optical properties of the disk to minimize photon losses and achieve a high Q of the disks.

3.3 Structural properties of microdisks

Raman scattering (RS) and photoluminescence (PL) spectroscopy are suitable techniques for non-destructive characterization of the structural properties of semiconductor MD heterostructures. In this section, detailed investigations of the strain and defect distribution along the MDs by means of these two methods are performed.

3.3.1. Micro-Raman spectroscopy

In this section, a detailed study of the strain distribution and extended defects in the MDs performed by high spatial and high spectral resolution μ-RS is presented. The measurements were performed on a commercial Raman spectrometer NTEGRA Spectra (NT-MDT Co., Moscow) with a spectral resolution of less than 1 cm^{-1}.

With changing the strain status in the crystal lattice, the phonon frequencies shift. Thus, by measuring the phonon frequencies, the strain in the lattice can be assessed. To exclude the shift of the Raman lines due to the warming effect from the laser illumination, RS

experiments with different illumination powers were carried out. On n-GaAs substrate the longitudinal optical (LO)-GaAs Raman line was measured at room temperature at excitation levels between 0.08 - 12.7 mW (32 - 5080 kW/cm^{-2}). Figure 17 shows the resulting GaAs Raman spectra under increasing excitation power. The LO Raman line of GaAs at about 292 cm^{-1} was observed. No shift of the line was found for excitation levels between 0.08 mW and 8 mW. Only at the highest excitation level (12.7 mW) a shift of the line position of about 1 cm^{-1} was observed which is within the spectral resolution of the spectrometer. Therefore, the sample heating due to the applied exciting laser radiation of 0.5 mW (200 kW/cm^{-2}) can be neglected.

In ZnSe/ZnMgSe MD structures the shift of the ZnSe LO phonon frequency induced by lattice strain was investigated by µ-RS. Figure 18 shows a series of Stokes-Raman spectra recorded at different spots on a disk with 8 µm diameter. Raman probing locations are schematically shown in the SEM image of such a disk (inset). Several peaks can be distinguished. The peak with a frequency of about 252 cm^{-1} results from the LO mode of the ZnSe layer and the peak at about 292 cm^{-1} corresponds to the LO phonons of GaAs. At 269 cm^{-1} a plasma-phonon coupled mode (L^{-}) at the ZnSe interface is observed. The ZnSe LO phonon frequency in the centre (area 1) of the disk is at 252.8 cm^{-1}. At an intermediate area (area 2) and at the edge of the MD (area 3) corresponding LO frequencies were observed at 251.5 cm^{-1} and at 250.0 cm^{-1}, respectively, yielding a frequency shift of ZnSe

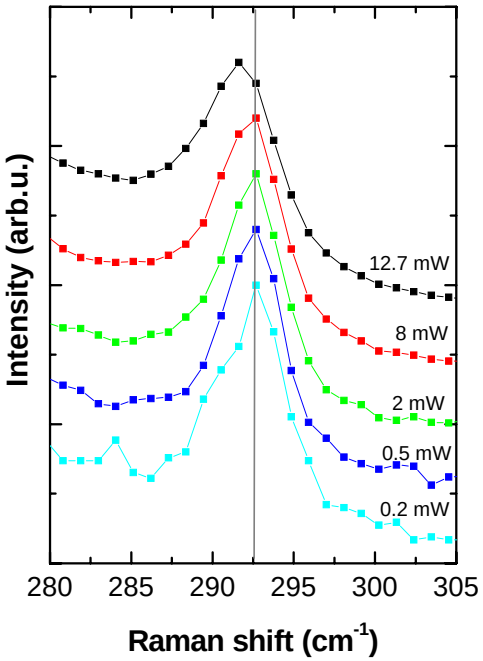

Figure 17. Raman spectra from the n-GaAs substrate at excitation power 0.08 – 12.7 mW.

LO phonons of 2.8±0.5 cm^{-1} from the edge to the centre. For reference the arrow shows the frequency of ZnSe LO phonons at 252.0 cm^{-1} measured with a fully relaxed 2 µm thick "bulk like" ZnSe layer on (001) GaAs. The width of the LO ZnSe Raman line of 7 cm^{-1} in the centre and at the intermediate area of the disk is comparable with the linewidth of strained ZnSe layers [70]. At the edge of the disk we observed a slight increase of the linewidth to 9.5 cm^{-1} due to light scattering at the disk sidewalls.

The shift of the LO phonon peaks of ZnSe to higher frequencies arises from in-plane compressive strain in the ZnSe layers due to the lattice mismatch between the GaAs substrate and the layer. It can be modelled as follows: The lattice parameter of ZnSe (0.5668 nm) is larger than that of GaAs (0.5653 nm). Therefore the pseudomorphic epitaxial growth of ZnSe on (001) GaAs will produce a biaxial compression of the unit cell of ZnSe along the x and y directions which is parallel to the grown surface. The nonzero components of the strain tensor in such a layer are

$$\varepsilon_{xx} = \varepsilon_{yy} = \varepsilon = (a_{\parallel} - a_{ZnSe})/\, a_{ZnSe} \text{ and } \varepsilon_{zz} = \{2S_{12}/(S_{11} + S_{12})\}\varepsilon \qquad \text{Eq. 23}$$

where a_{ZnSe} represents the lattice parameter of bulk ZnSe, $a_{\parallel}$ is the in-plane lattice parameter of the epitaxial layer and S_{ij} are the elastic compliance constants of ZnSe. The strain ε is negative for compressive strain. Under these conditions the LO phonon frequency ω of the strained layer is given by the following expression [71]

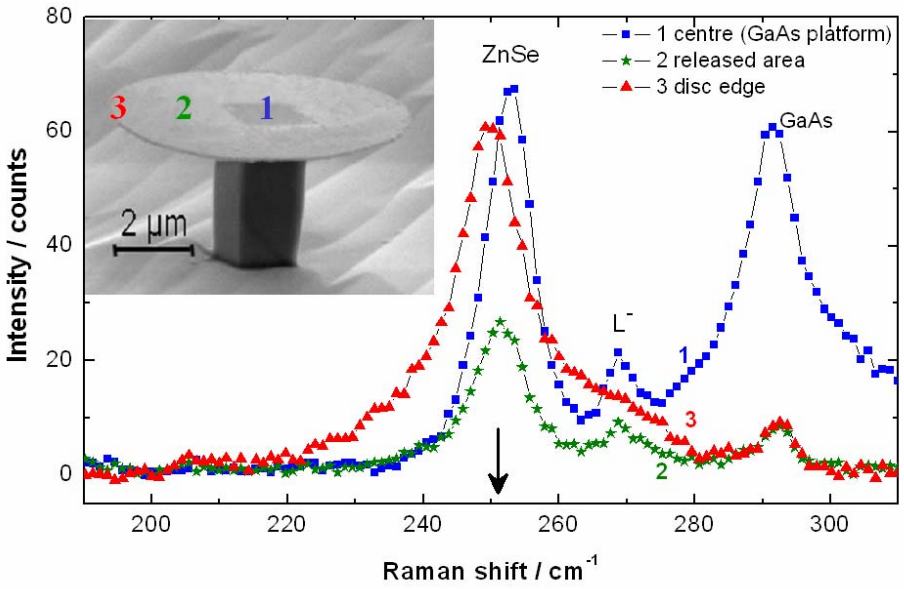

Figure 18. Raman spectra of the LO phonons recorded at thee different spots along the 8 µm diameter MD supported by GaAs post. Schematically Raman probing locations are shown in the insetted SEM image of such a disk. The arrow indicates the LO phonon frequency of bulk ZnSe.

$$\omega = \omega_0 + 2\Delta\Omega_H - \frac{2}{3}\Delta\Omega \qquad \text{Eq. 24}$$

where ω is the undisturbed bulk frequency, $\Delta\Omega_H$ and $\Delta\Omega$ are the shifts due to the present stress. According to [71] these shifts are:

$$\Delta\Omega_H = \frac{p+2q}{6\omega_0^2}\left(\frac{S_{11}+2S_{12}}{S_{11}+S_{12}}\right)\omega_0\varepsilon \qquad \text{Eq. 25}$$

and

$$\Delta\Omega = \frac{p-q}{2\omega_0^2}\left(\frac{S_{11}-S_{12}}{S_{11}+S_{12}}\right)\omega_0\varepsilon \qquad \text{Eq. 26}$$

For ZnSe $S_{11} = 2.26\times10^{-11}$ Pa^{-1} and $S_{12} = -0.85\times10^{-11}$ Pa^{-1} as well as the parameters $-(p+2q)/6\omega_0^2 = 0.93$ and $(p-q)/2\omega_0^2 = 0.64$ are inserted and calculated according to the data given in Refs. [71] and [72]. Hereby, the coefficients p and q describe the changes in the "spring-constant" of the $\vec{k} \approx 0$ optical phonons due to the presence of strain. Using these values and $\omega_0 = 252.0$ cm^{-1} in Eq. 24 to Eq. 26 we obtain the relationship

$$\Delta\omega = \omega - \omega_0 = -428.2\varepsilon \qquad \text{Eq. 27}$$

with ω in units of cm^{-1}. Eq. 27 reveals a blue shift of ω for negative ε, which is in good agreement with the experimentally measured shift of the ZnSe LO phonon as shown in Figure 18. If we assume that the lattice mismatch between ZnSe and GaAs is accommodated by uniform deformation, we get $\varepsilon = -2.29\times10^{-3}$ and a frequency shift of the LO phonon of $\Delta\omega = 0.98$ cm^{-1}. This value is significantly smaller than observed in our experiments. Considering the volume ratio of ZnMgSe to ZnSe in our disks, the ZnSe QW is likely to be tensile strained on ZnMgSe in the periphery of the freestanding material. If we suppose that ZnSe is compressively strained on GaAs at the post position (area 1) and tensile strained on ZnMgSe at the edge (area 3) of the disk, we obtain $\varepsilon = -6.44\times10^{-3}$ and hence $\Delta\omega = 2.76$ cm^{-1}. The lattice parameter of ZnMgSe is calculated using Vegard's law to 0.56906 nm and the Mg concentration was obtained from HRXRD measurements (shown in section 3.2.1.). The calculated value for the ZnSe LO phonon shift is in agreement with the measured value supporting the model of a tensile strained ZnSe layer in the edge region of the disk.

ZnMgSe alloy is expected to have ZnSe-like and MgSe-like LO phonons with 247 cm^{-1} and 308 cm^{-1}, respectively, for 9% Mg concentration [73]. The MgSe-like mode is quasi

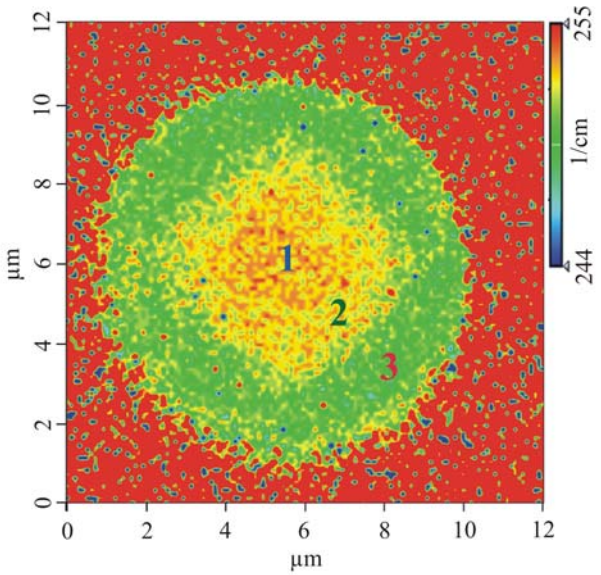

Figure 19. Micro-Raman map of the ZnSe LO phonon peak frequency. Outside the disk area no ZnSe LO phonon was observed.

negligible due to the small fraction of Mg in the crystal, while the ZnSe-like mode is considerably weaker as the ZnSe LO line from ZnSe and could not be resolved in our spectra.

The distribution of strain in the micro-cavity is depicted in Figure 19, where the Raman shift of the ZnSe LO peak is plotted vs. the position on the disk. The intensity of the ZnSe LO Raman line outside the disk area is zero. Three different regions of strain are distinguished: 1) At the intersection of the GaAs post we find clear evidence that the ZnSe/ZnMgSe QW is pseudomorphic strained with the lattice parameter of the GaAs post. 2) In a region which covers about the inner-half of the freestanding part of the disk we observe a phonon frequency which is almost identical to that of relaxed (bulk like) ZnSe. 3) The edge region with a width of about 2 µm shows a radial symmetric distribution of tensile strain. This strain distribution is due to the equilibrium distribution of strain in the ZnSe/ZnMgSe QW with a common lattice parameter.

The distribution of the transverse optical (TO) phonon in the micro-cavity is depicted in Figure 20, where the Raman shift of the ZnSe TO peak is plotted vs. the position on the disk. In relaxed ZnSe the TO line appears at about 208 cm^{-1}. Across the entire area of the disk no TO phonon Raman line was observed. As shown in [74] first-order TO phonon RS with $\vec{k} \approx 0$ from (001) surfaces is forbidden in backscattering geometry. However, TO phonon RS has been observed by several groups in RS experiments with relaxed (001) ZnSe [73, 75, 76]. D. Olego and M. Cardona [77] performed a detailed study of TO phonon RS. They found that the existence of the TO phonon line in the RS spectra of (001)

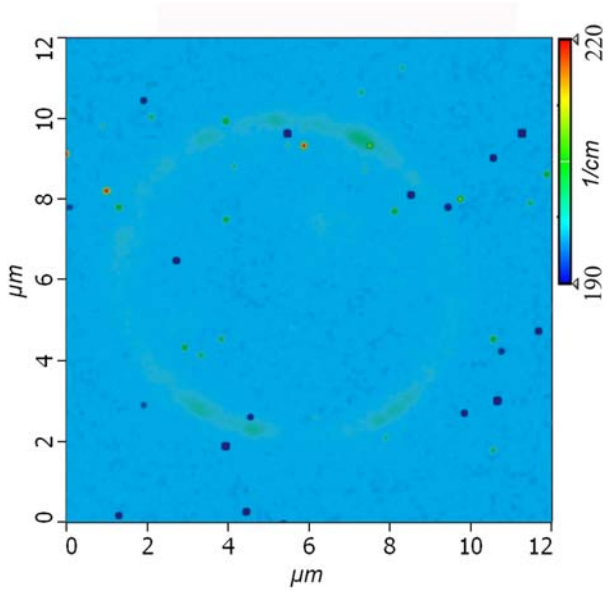

Figure 20. Micro-Raman map of the ZnSe TO phonon peak frequency.

oriented samples is related to defects in the samples rather than to a misorientation of the surface. According to [75] defect scattering lifts the wavevector conservation, which in defect-free samples would not be allowed for TO phonons. This is in good agreement with our investigations [78] that TO phonon lines are absent in the defect-free and strained ZnSe layers but can be observed in ZnSe with a thickness exceeding the critical thickness for lattice relaxation. Thus the absence of TO phonon lines in our Raman spectra of the MD is a strong indication that the density of extended defects in the disk area is negligible.

3.3.2. Micro-photoluminescence

PL spectroscopy is a suitable technique for the characterization of the structural and optical properties of semiconductor heterostructures. In this section a study of the strain distribution and optical transitions in the MDs performed by highly spatial resolved µ-PL is conducted.

First, the optical properties of the unstructured ZnSe/ZnMgSe QW were investigated. Figure 21 a) shows the PL spectrum of an unstructured ZnSe/ZnMgSe multilayer structure with a F:ZnSe δ-doped region in the centre of the ZnSe QW. The inset shows the multilayer sample structure. The emission at 2.812 eV corresponds to the recombination of FX-hh in the compressively strained ZnSe QW. This energy is consistent with the finite barrier model in Refs. [20, 21]. Weak FX-lh emission at 2.829 eV is indicated where the intensity was multiplied by a factor of 10 for convenience. The lower energy peak

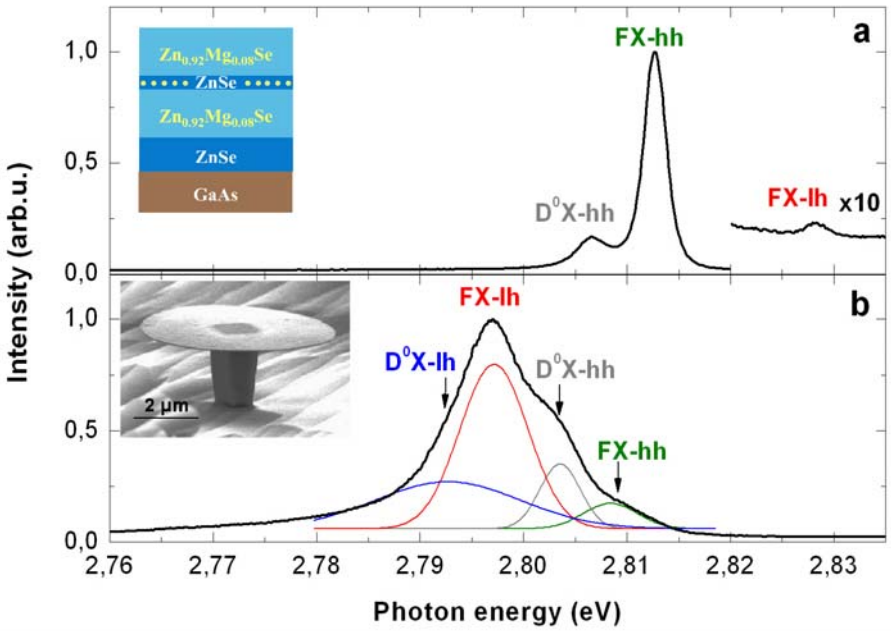

Figure 21 . PL spectra taken at 5K. a) PL for an unstructured F:ZnSe δ-doped QW sample. b) PL of a 6 µm MD structure. Inset: QW sample structure and SEM picture of such a disk.

observed at 2.806 eV in Figure 21 a) is due to the D^0X-hh recombination, about 6 meV separated from the corresponding FX state. The widths of these peaks indicate only small inhomogeneous broadening, most likely due to strain effects.

Next, the PL investigations of the MDs were carried out. Figure 21 b) shows the PL spectrum of a complete disk area made from the same multilayer structure as the one represented in Figure 21 a). The inset shows a SEM picture of such a MD. In the spectrum we observe a broad emission band consisting of several peaks. As was discussed in the previous section, the ZnSe QW is likely to be tensile strained on ZnMgSe in the periphery of the disk. The corresponding transition energies in Figure 21 b) are fitted by four Gaussian peaks. The FX-hh and D^0X-hh transitions at 2.810 and 2.804 eV are only slightly shifted and broadened. These peaks stem from the PL close to the centre of the disk. The D^0X-hh luminescence is stronger than the FX-hh luminescence due to the recombination of FX at the surface. In the released periphery, the FX-lh emission moves to a lower energy of about 2.798 eV. The D^0X-transitions again appear about 6 meV lower than the corresponding FX transitions, but are substantially broadened due to the strain gradient across the disk.

The strain gradient across the disk results in a substantial band gap narrowing effect along the radial direction of the disk from the centre to the edge. Figure 22 shows a schematical sketch of strained multilayers in a MD and the resulting bandgap narrowing

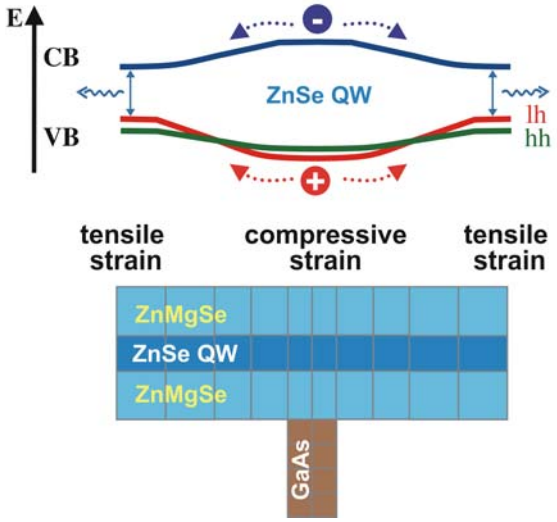

Figure 22. Schematical sketch of strained ZnSe QW in a MD and resulting bandgap narrowing over the MD.

over the MD. In the centre of the disk the ZnSe QW is compressively strained on GaAs and has a larger bandgap than at the edges of the disk, where the ZnSe QW is tensile strained on ZnMgSe. The bandgap narrowing in the direction towards the disk edge enhances the charge carrier transfer to the periphery, where the optical WGMs are localized. This effect reduces the carrier loss and provides a remarkably low threshold in the MD laser as was shown through band and rate equation analyses by M Fujita et al. [79].

To investigate the strain release over the disk in more detail, spatially resolved µ-PL measurements were carried out. Figure 23 shows the PL spectrum of an unstructured ZnSe/ZnMgSe QW sample (black curve A) taken at 5 K for reference and the µ-PL spectra of the 4.5 µm diameter MD, measured at different positions from the centre to the edge, as indicated in the inset. For the unstructured QW, the same three peaks are identified as discussed above for Figure 21 a). The µ-PL spectra of the MD reveal a relative broad emission band consisting of different emission lines. By scanning the excitation spot from the centre to the edge of the disk the emission band reveals an energy redshift. The corresponding transition energies are obtained by fitting the emission band at the edge of the disk by four Gaussian peaks. We assume that at the edge of the disk (point 3) the largest peak at 2.80 eV corresponds to the FX-lh and the peak at 2.807 eV to the FX-hh transition. The hh and lh transitions of D^0X are detected at 2.804 eV and 2.797 eV, respectively. By moving the excitation spot from the centre to the edge of the disk, the intensity of the FX-hh and D^0X-hh transitions is reduced. In contrast, the µ-PL of the FX-lh and D^0X-lh transitions is enhanced resulting in an overall redshift in the PL spectra. This

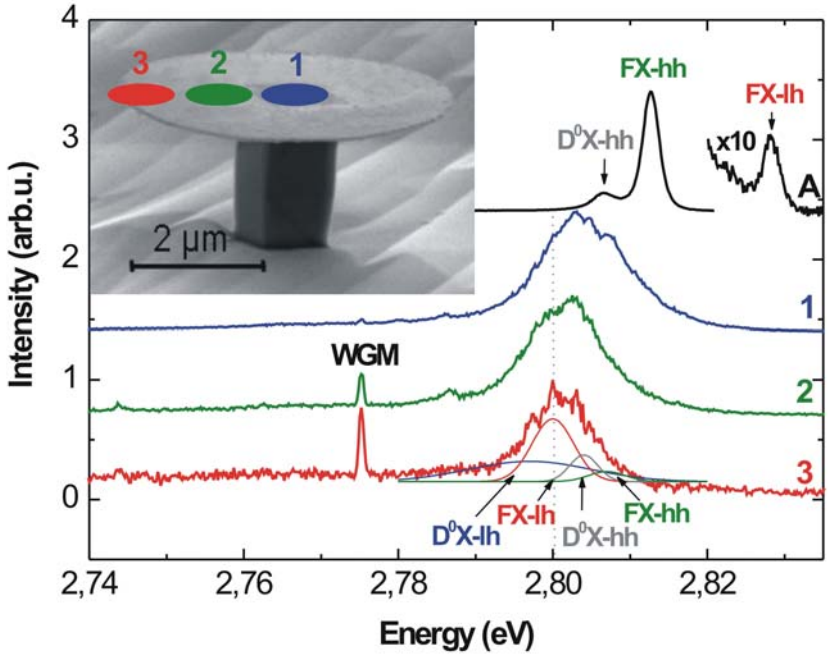

Figure 23. PL spectra taken at 5 K with cw-laser excitation for unstructured ZnSe/ZnMgSe QW (black curve A) and on a disk with 4.5 µm diameter at several points (curves 1-3). Inset: SEM micrograph of the disk. Indicated are the spots of excitation locations.

observation is in good agreement with the assumption that the periphery of the disk is tensile strained. Thus, the lowest energy transitions are the lh-related transitions.

In addition to these results, a WGM with a FWHM of $\Delta E = 0.6$ meV at the mode energy of $E = 2.775$ eV appears and the intensity of this WGM increases towards the edge of the microstructure. The FWHM of the WGM corresponds to a cavity-Q exceeding 4500. This is the highest Q factor achieved with ZnSe MDs until now. Such a high Q factor indicates a high quality of the device assembly.

3.4 Fluorine impurities in microdisks

For the detection of fluorine impurities in the ZnSe QW the PL spectra of unstructured F-doped and undoped QW samples were measured at 5 K with excitation provided by a blue light-emitting diode with a wavelength of 365 nm. Figure 24 a) shows the PL spectra of an unstructured F:ZnSe δ-doped QW (red curve) and undoped QW (black curve). The inset shows the material composition of the unstructured sample. The PL spectra of these strained samples show two characteristic peaks as presented in Figure 21 a). The emission at 2.810 eV corresponds to the recombination of FX-hh excitons in the compressively strained ZnSe QW. The lower-energy peak observed at 2.804 eV is due to D^0X-hh exciton

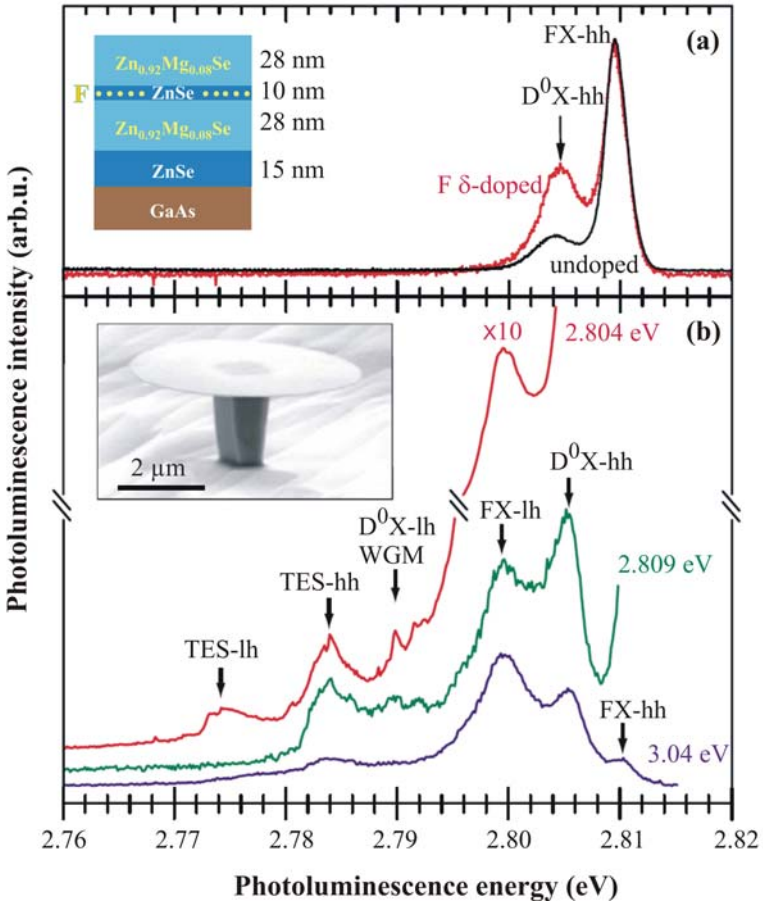

Figure 24. PL and SPL spectra taken at 5 K. a) PL of unstructured F:ZnSe δ-doped QW (red curve) and undoped QW (black curve). Inset: the material composition of the unstructured sample. b) Above-band PL (blue curve) and SPL spectra of a 6 µm disk taken under resonant excitation of the D^0X-hh peak (laser energy of 2.804 eV) and the FX-hh peak (laser energy of 2.809 eV). Inset: scanning electron micrograph of a 6 µm disk.

recombination, as confirmed by the expected 6 meV separation. A significant increase of the intensity of the D^0X-hh line is seen in case of the fluorine δ-doped (red curve) versus the undoped sample (black curve). This demonstrates a clear evidence of the fluorine impurities in the ZnSe QW. The widths of these peaks indicate inhomogeneous broadening likely due to strain effects. However, the broadening is still less than typically seen in ensembles of QDs and may be useful for the isolation of individual impurities.

Thus, a clear evidence of the fluorine impurities in the ZnSe QW was demonstrated. The contribution of the fluorine impurities to the PL of a MD sample (as was shown in previous sections) was studied by measuring the spectral selective photoluminescence (SPL). Figure 24 b) shows the SPL spectra taken at 5 K from a MD with 6 µm diameter. The inset shows a scanning electron micrograph picture of such a MD. First, the emission of the MD (blue curve) was measured with excitation provided by a pulsed laser with an

energy of 3.04 eV, which is close to the resonance of the ZnMgSe barriers (2.91 eV). In comparison to the PL of unstructured QW in Figure 24 a), the PL of the MD is broadened and shifted to lower energies which confirm band-gap narrowing due to the strain relaxation. Another reason could also be the transfer of the FX in direction of the MD boundary due to the bandgap narrowing, whereas the donor-bound excitons are localized. The modified transition energies are found by fitting the above-band PL to five Gaussian peaks. The FX-hh and D^0X-hh transitions at 2.81 and 2.804 eV are only slightly shifted and broadened. These peaks originate from PL around the centre of the disk, where the material remains fully strained. No cavity modes are observed in this region of the spectrum. The D^0X-hh luminescence is stronger than the FX-hh luminescence due to surface recombination of the FX. The satellite transitions (TES) are visible at a position of 21 meV beneath the D^0X-hh luminescence. This energy is in agreement with the calculated position of the TES of the D^0X [19]. In the relaxed periphery, the FX-lh emission is red shifted to an energy of about 2.799 eV. The D^0X transitions again appear 6 meV lower than the corresponding FX transitions, but are substantially broadened due to the strain gradient across the disk.

The FX-hh transition and the D^0X-hh transition were resonantly excited by a scanning narrow-band Ti:Sapphire ring laser doubled by an $LiNbO_3$ crystal in a high finesse cavity. By resonant excitation of the FX-hh transition at 2.809 eV (green curve), the TES-hh lines are enhanced relative to above-band excitation. Resonant excitation of the D^0X-hh peak at 2.804 eV (red curve) results in the appearance of a new satellite peak at 2.774 eV which was identified as the TES-lh transition. This observation of TES lines in SPL strongly confirm the expected contribution of F-donor-bound excitons to the band edge luminescence. At resonant excitation of the QW states the interaction between photons and electrons is stronger as for non-resonant (over-gap) excitation. Hence for the resonant excitation the efficiency of the excitation increases simultaneously with the probability for excitons to be bound to a donor. Thus the probability to observe the TES transitions increases. A sharp peak at 2.79 eV was repeatedly observed when resonantly exciting the D^0X-hh line. This peak corresponds to a WGM of the MD.

The results of the Raman and the PL investigations demonstrate a variation of the strain over the disk from compressive to tensile strain, which results in a substantial band gap narrowing effect along the radial direction of the disk from the centre to the edge. This effect contributes to the additional charge carrier transfer to the periphery, where the

optical WGMs are localized. The absence of the ZnSe TO Raman line in the spectra indicates that strain relaxation in the structure is not accompanied by the generation of extended defects. These findings are in good agreement with the observation of the high Q values (exceeding 4500) in our MDs. Clear evidence of the fluorine impurities in the MD was demonstrated. If an exciton is bound to a donor, the population inversion condition is obtained for the donor state. Thus, in comparison to a QW, the donor-bound excitons could require less excitation power to achieve optical gain. These findings demonstrate an effective preparation process of defect-free MDs for the realization of a low-threshold laser.

3.5 Lasing in ZnSe microdisks

In this section evidence for laser emission from fluorine-doped ZnSe QWs in MD cavities with 3 and 6 μm diameter is presented [80, 81].

Low temperature PL spectra of F-doped single MDs were measured at 5K, using pulsed excitation by a frequency doubled mode-locked Ti:Sapphire laser operated at 409 nm wavelength (3.031 eV), a pulse repetition rate of 82 MHz, and a pulse width of 1.5 ps. The FWHM diameter of the focused laser spot on the sample was about 15 μm.

To determine the laser threshold, the spectra of disks with 3 and 6 μm diameter were recorded at varying excitation power. Figure 25 shows a series of PL spectra taken from a MD with 6 μm diameter and measured with different average excitation intensities varying between 36 and 136 Wcm^{-2}. Due to the reflection, only 50% of the excitation power was assumed to be absorbed in the disk. For clarity, the intensities were normalized to the particular maximum of the spectra and the spectra have been shifted by vertical offsets. For all excitation densities a broad emission band at about 2.80 eV is observed, consisting of different emission lines: FX-hh transition at 2.809 eV, D^0X-hh transition at 2.804 and FX-lh transition at 2.799 eV. The transitions were discussed in detail in the previous sections. At higher pumping power (> 36 Wcm^{-2}) emission from the MD cavity modes becomes significant and eventually dominates the entire spectrum. For small power densities exceeding 36 Wcm^{-2} the superlinear increase of a group of two sharp peaks close to 2.79 eV is observed. These peaks correspond to a WGM of the MD resonant with the D^0X-lh emission. This mode group is here named M1. Additional group of modes (M2) emerge at the energies 2.783 eV and 2.785 eV for pump power densities larger than 52 Wcm^{-2}.

Further modes (M3) appear at 2.777 eV and 2.773 eV for pump power densities larger than 100 Wcm^{-2}. The energies of both modes M2 and M3 are resonant with the observed D^0X-hh and the D^0X-lh TES transition energies [19] (s. section before). Multiple modes are observed more likely due to higher order radial modes of the disk. However, some modes are inhomogeneously broadened and thus compose of mode doublets that are too closely spaced to correspond to the free spectral range of the WGMs. The characteristics of the WGMs are the clockwise and counterclockwise propagating modes, which have the same frequency for the ideal case. However, in a real device with fabrication imperfections, as backscattering caused by the sidewall roughness, strain gradient and possible slight warping of the disk, the degeneracy of counter-propagating modes can be lifted. This effect can be observed in the occurring closely spaced mode doublets.

For the theoretical calculations of the modes by FIT, the ideal disk geometry was assumed with a multilayer structure as shown in Figure 11 but without GaAs substrate. For ZnSe and ZnMgSe the permittivity of 8.9 and 9.02, respectively, was applied. The

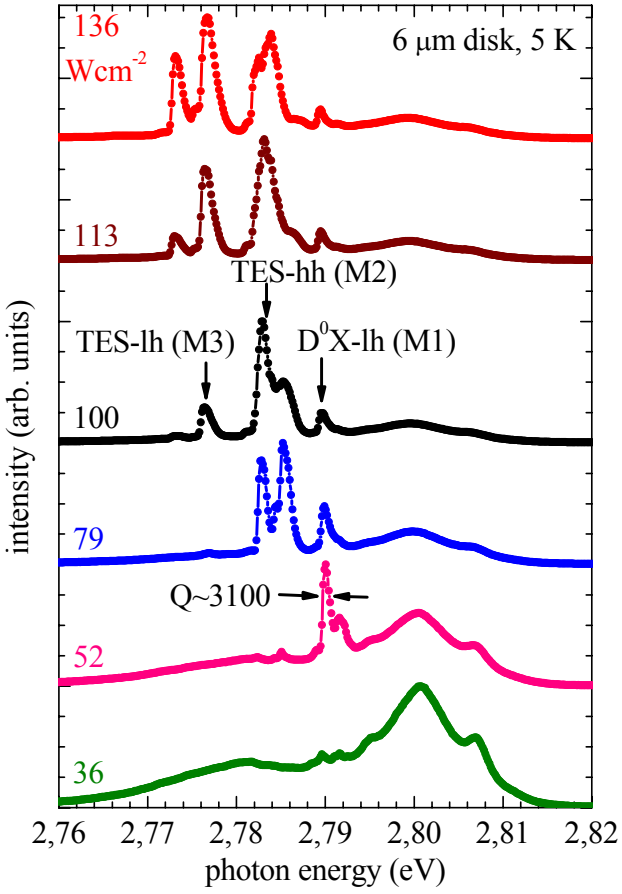

Figure 25. Power-dependent PL spectra and lasing of a MD with 6 µm diameter. The excitation density was varied between 36 and 136 Wcm^{-2}. For low excitation, the first WGM (mode M1) emerges at 2.79 eV and has a cavity-Q of about 3100. Further modes (M2 and M3) are observed with increasing excitation density.

permittivity of 1 (air) was taken for the ambience. In our calculations the losses and the effect of the supporting GaAs pedestal were neglected.

The calculated spectra for TE and TM modes of a disk with 6 µm diameter are shown in Figure 26. The amplitude was normalized to the particular maximum for convenience. However, the absolute amplitude values vary depending on the recording position on the disk, and are not of relevance here. The spectra display a superposition of several series of resonances, each corresponding to modes with a fixed radial quantum number n_r and azimuthal quantum number m. The modes with an order higher than 3 ($n_r>3$) were not determined. The high mode volume of the high order modes results in a low photonic density of states in these modes. Hence, higher order modes have a week contribution to the amplification. The energy positions of the experimentally observed mode groups (M1, M2 and M3) are indicated. A number of closely spaced modes was observed. Taking into account the spontaneous emission transitions in our MDs, we observe an overlap of the mode H2.92 with D^0X-lh transition (M1). In the area of M2 three TM modes were found. Two of the modes were defined as E1.76 and E2.70. The field distribution of these two modes is shown in the inset of Figure 26. Thereby red corresponds to the highest field density and blue is the lowest field density. The black

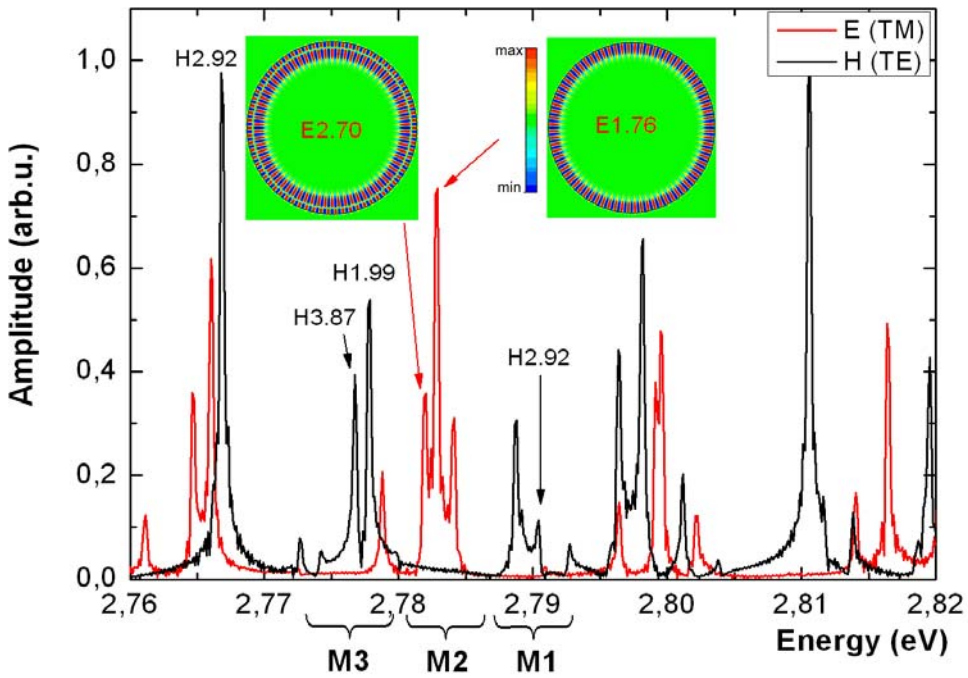

Figure 26. Simulated mode spectrum of the disk with 6 µm diameter. The resonances are labeled with TE and TM to indicate their polarization as well as their azimuthal and radial quantum numbers m and n_r respectively. The field distribution of the modes E2.70 and E1.76 is insetted. Thereby red corresponds to the highest field density and blue is the lowest field density. The black circle indicates the edge of the microdisk.

circle indicates the edge of the microdisk. In the area M3 the modes H1.99 and H3.87 were determined. Further modes with higher radial number are arranged in the areas M1, M2 and M3 and have most likely some week contribution to the emission.

Figure 27 shows the integrated intensity of the strongest lasing modes in groups M1 (a), M2 (b) and M3 (c) for a 6 µm disk plotted versus the excitation power density in a double-logarithmic scale. The curves show the typical intensity jump $\propto\beta^{-1}$ from below to above threshold. The observed super-linear increase and corresponding threshold start at approximately 40 Wcm^{-2} for the higher energy mode 1 and at around 70 Wcm^{-2} for the lower energy mode 2. Mode 3 with an even higher threshold appears at much stronger excitation of about 100 Wcm^{-2}, as can be seen in the spectrum in Figure 27 (c). The guided modes seem to compete for gain. At the lower excitation power mode 1 is dominating. As the pump power exceeds 80 Wcm^{-2}, the main intensity of the primary mode 1 is transferred to mode 2. Thereby intensity saturation of M1 and an increase of the intensity of mode 2 are observed. For the excitation density exceeding 100 Wcm^{-2}, the intensity of mode 2 is transferred to mode 3. The intensity of mode 2 first saturates and then decreases slowly, while the intensity of mode 3 rises. Hence, lower energy modes with even higher

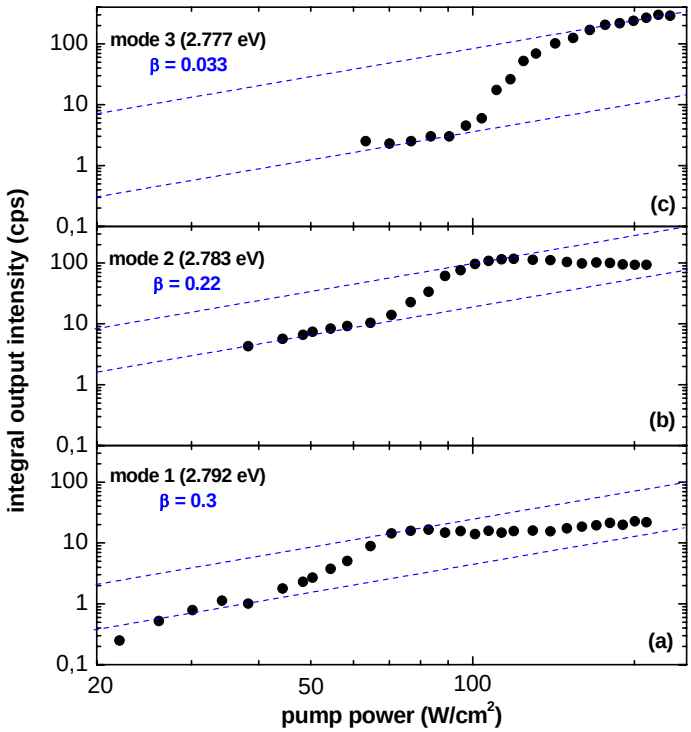

Figure 27. Integrated intensity of the three lasing modes of a 6 µm disk vs. the excitation power density in a double-logarithmic scale. Filled circles are the measured data and the blue dashed lines are asymptotes for low and high power. The onset of lasing of mode 3 is observed at a threshold of about 100 Wcm^{-2}.

thresholds come up for much stronger excitation. With increasing excitation power the electronic density of states in the QW increases. Thus, the probability for D^0X excitons and with it for TES transition rises and lower energy modes come up. Furthermore, the shift of the cavity mode energies with increasing excitation power can have an impact. The blue shift of the cavity modes is associated to a carrier-induced change of the refractive index, which, in turn, modifies the energy position of the cavity modes [82]. Therefore, the increase of the excitation power, results in a shift of the lower energy modes into resonance with TES transitions and out of the maximal resonance condition with the D^0X-lh transition.

The slope of output power vs. input power indicates the fraction of spontaneous emission coupled into the lasing mode. For small β (close to zero) a sharp threshold for lasing is expected, whereas for large β (close to unity) the transition from spontaneous to stimulated emission is smeared out and very low laser thresholds can be achieved. For the modes 1, 2 and 3, β was found to be 0.3, 0.22 and 0.03, respectively.

Figure 28 shows the integrated intensity fitted theoretically (red curve) of the strongest lasing modes in groups M1 (a), M2 (b) and M3 (c) for a 6 μm disk plotted versus the excitation power density in a double-logarithmic scale. The relationship of emitted intensity and excitation power for semiconductor microlasers was theoretically derived by using the rate equation model from Björk and Yamamoto [83]. Denoting p the mean photon number in the cavity and I the pumping rate of the exciton states, we get the following expression:

$$I = \frac{q\gamma}{\beta}\left[\frac{p}{1+p}(1+\xi)(1+\beta p) - \xi\beta p\right] \qquad \text{Eq. 28}$$

where γ is the photon escape rate from the cavity, β is the fraction of spontaneous emission coupled into the cavity mode, ξ represents the mean number of emistted photons in the cavity at the gain medium frequency. The input-output characteristics are best reproduced with parameters shown in Table 1. Mode 1 has the major number of emitted photons in the cavity and the highest fraction spontaneous emission coupled ilhnto the lasing mode, which explains the lowest threshold of the lasing. However, this mode has also the highest losses from the cavity indicated by highest γ. Mode 3 has lower losses, but also a lower number of photons. This results in the higher threshold for mode 3. For mode 2 the fit parameter were found between the parameters of modes 1 and 3. This is in agreement with

the observed value of the threshold for mode 2. However, the experimental characteristic is not

Parameter	Mode 1	Mode 2	Mode 3
γ	0.9	0.24	0.24
β	0.5	0.15	0.03
ξ	25.5	22	6.3

Table 1. Parameter for the fits calculated using Eq. 28 for the input-output characteristics of the strongest lasing modes observed in 6 µm disk.

perfectly reproduced by this model. The β-factor for mode 1 is theoretically bigger and for mode 2 is smaller, as experimentally determined. The model for the input-output characteristic implies a microcavity laser based on a two- or multi-level system. The microcavity supports only one mode within its gain bandwidth. However, in our system semiconductor effects, such as a modified source term (impurities instead of a bulk material) of spontaneous emission and Coulomb effects, multimodes and possible full inversion lead to novel effects in the emission properties. This explains the deviation of theoretical model and experimental results.

The energy positions and the linewidth of the modes 1, 2 and 3 were analyzed as a

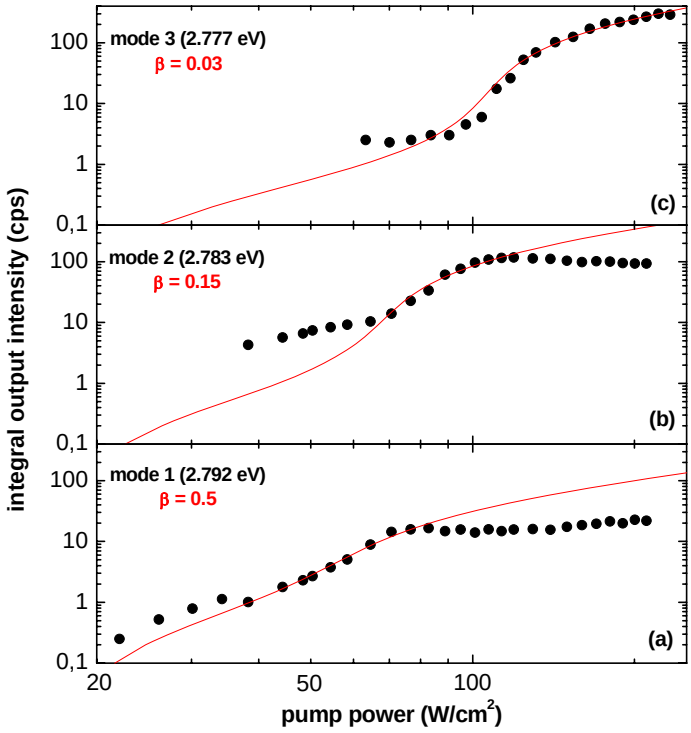

Figure 28. Integrated intensity of the three lasing modes of a 6 µm disk vs. the excitation power density in a double-logarithmic scale. Filled circles are the measured data and red solid lines are the fit curves according to Eq. 28.

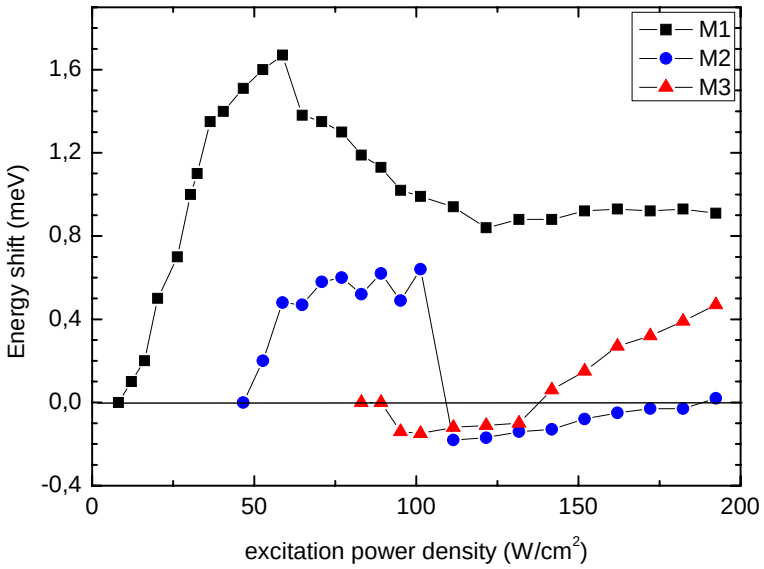

Figure 29. Energy shift of modes 1, 2 and 3 as in 6 µm disk a function of pump power density.

function of the pump power. Figure 29 shows the energy shift of the three modes as a function of the excitation power. At lower excitation the energy of mode 1 rises until an excitation of 59 Wcm^{-2}. After this the energy of mode 1 decreases until an excitation of 121 Wcm^{-2} and then increases slowly again. The energy of mode 2 also first rises until an excitation of 59 Wcm^{-2} and remains nearly constant until 101 Wcm^{-2}, where a sharp energy decrease is observed. Further, the energy of mode 2 increases to the initial energy value. The energy of mode 3 first decreases slightly until 89 Wcm^{-2} and remains nearly constant until 131 Wcm^{-2}, and afterwards increases by about 500 µeV. We suppose that mode hopping takes place for all three modes. With increasing excitation power, the modes obtain an energy blue shift. Hence, modes with lower energy are shifting into resonance with spontaneous emission whereas modes with higher energy are shifting out of the resonance. This is consistent with the simulation of the modes (s. Figure 26), where several closely spaced modes were observed in the spectral area of spontaneous emission transitions.

Figure 30 shows the linewidth (FWHM) of the modes 1, 2 and 3 in a 6 µm disk as a function of the pump power density. For mode 1 the linewidth increases from 0.61 to 0.98 meV until 59 Wcm^{-2}, then decreases to the initial value and remains constant within the error limits. At 121 Wcm^{-2} the linewidth of mode 1 increases to the value 0.85 meV. The linewidth of mode 2 rises at small pump power whereas the linewidth has a small jump in the area of 59 Wcm^{-2}. At 101 Wcm^{-2} the linewidth of mode 2 reduces considerably from 1.42 meV to 0.66 meV and after that rises slowly with increasing pump power. The

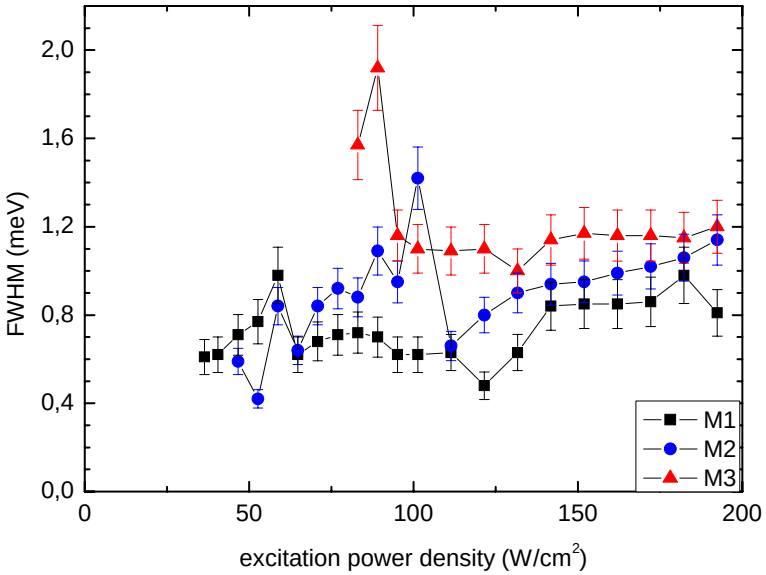

Figure 30. Full width of half maximum (FWHM) of modes 1, 2 and 3 in 6 µm disk as a function of pump power density.

linewidth of mode 3 also increases first to the value of 1.92 meV at 89 Wcm^{-2}, and after that drops to the value of 1.1 meV, and then remains constant within the error limits. The sharp decrease in the linewidth of modes 2 and 3 at the excitation of around 100 Wcm^{-2} proves the existence of amplified spontaneous emission within the PL line in this excitation density regime. This is an indication of the lasing onset.

The linewidth of the modes indicates a cavity Q that reaches values exceeding 4500 in a 6 µm disk. The cavity Q values, measured as $Q = E/\Delta E$, vary depending on modes and device quality. Our MDs typically show Q>2000. In comparison to the ideal disk Q values in the real disk are smaller due to the absorption and scattering in the cavity. Additionally, an effect of the GaAs pedestal results in optical losses for disk modes that overlap the pedestal. This limits the number of low-loss modes and leads to the coupling of radiation into the vertical direction, perpendicular to the plane of the disk [37].

The experimentally observed Q values and the mode volume allows to estimate the Purcell factor f_p, which is proportional to Q/V (s. Eq. 22), of the microdisk cavities. Since, it is not possible to measure the volume of a cavity mode, numerical simulations were done for assessment. Hence, the mode volume was calculated from the field distribution of the modes using the theory given in [84]. The Purcell enhancement factor for a 6 µm disk, based on experimentally determined Q and calculated mode volume was found to be about 3.2.

Lasing was also observed with smaller MDs with 3 µm diameter. Figure 31 shows a series of PL spectra taken from a MD with 3 µm diameter and measured with different

average excitation intensities varying between 9 and 32 Wcm^{-2}. For small power densities exceeding 5 Wcm^{-2}, a broad emission band at about 2.8 eV is observed consisting of different emission lines that were discussed in detail in the previous sections. Firstly, a superlinear increase of a mode at 2.790 eV (M1) was observed. This peak corresponds to a WGM of the MD excited by D^0X-lh emission as was discussed for Figure 24 b). Additional modes emerge at energies of 2.783 and 2.785 eV (M2) and at 2.776 eV (M3) for pump power densities larger than 12 Wcm^{-2}. Mode M2 consists of two competing modes, which appear more likely due to higher order radial modes of the disk. At higher excitation densities, the overall intensity of M1 and M2 is transferred to M3, which is resonant with the TES-lh transition energies of the bound exciton states.

The peaks corresponding to WGMs are not visible in low power PL by using either a continuous wave 405 nm diode laser or the doubled 408 nm output of a mode-locked

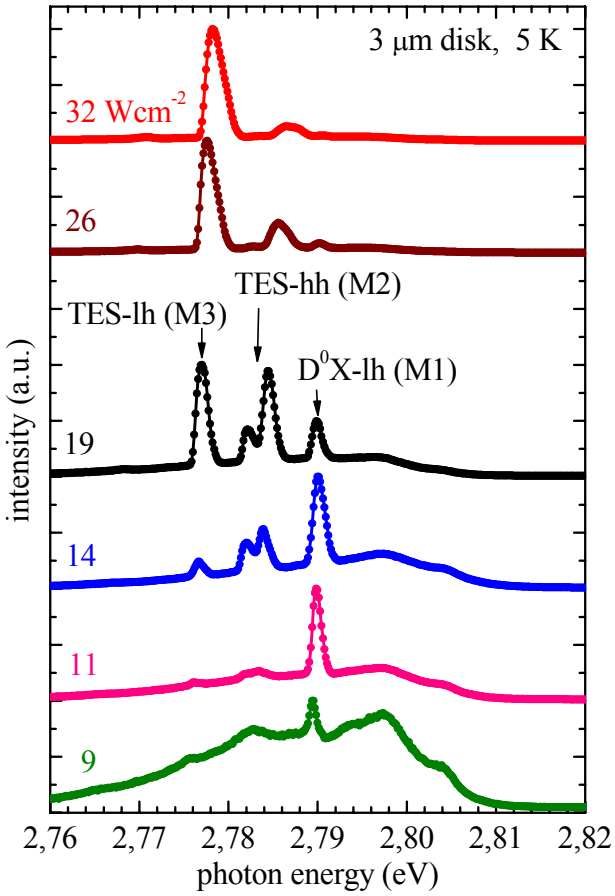

Figure 31. Power-dependent PL spectra and lasing of a MD with 3 µm diameter. The excitation density was varied between 9 and 32 Wcm^{-2}. For low excitation, the WGM (mode M1) emerges at 2.790 eV. The energies of the relevant heavy-hole and light-hole transitions are indicated by dashed lines. Further modes (M2 and M3) are observed at moderate excitation densities.

Ti:sapphire laser. The reason most likely is absorption due to lower-energy transitions in the inhomogeneously broadened emission distribution that damps the cavity Q. However, at higher excitation powers, these lower-energy transitions saturate and the cavity modes appear.

The calculated spectra for TE- and TM-modes of a disk with 3 µm diameter are shown in Figure 32. The amplitude was normalized to the particular maximum for convenience. However, the absolute amplitude values vary depending on the recording position on the disk, and are not of relevance here. The spectra display a superposition of several series of resonances, each corresponding to modes with a fixed radial quantum number n_r and azimuthal quantum number m. The 3 µm disk shows fewer modes than the 6 µm disk. This is in good agreement with the theory of cavity modes where the mode spacing increases with decreasing resonator diameter. The D^0X-lh transition couples most likely with a mode H2.42. The mode H1.47 overlaps with the spontaneous emission of the TES-lh transition (M3). The TES-hh transition (M2) overlaps with the mode E1.36. The other mode in the group M2 (named M2a) is most likely a mode of higher order, which is not resolved in the calculated spectra. However, we find an amplification for this mode although it has a lower photonic density than first and second order modes. This indicates a high electronic density

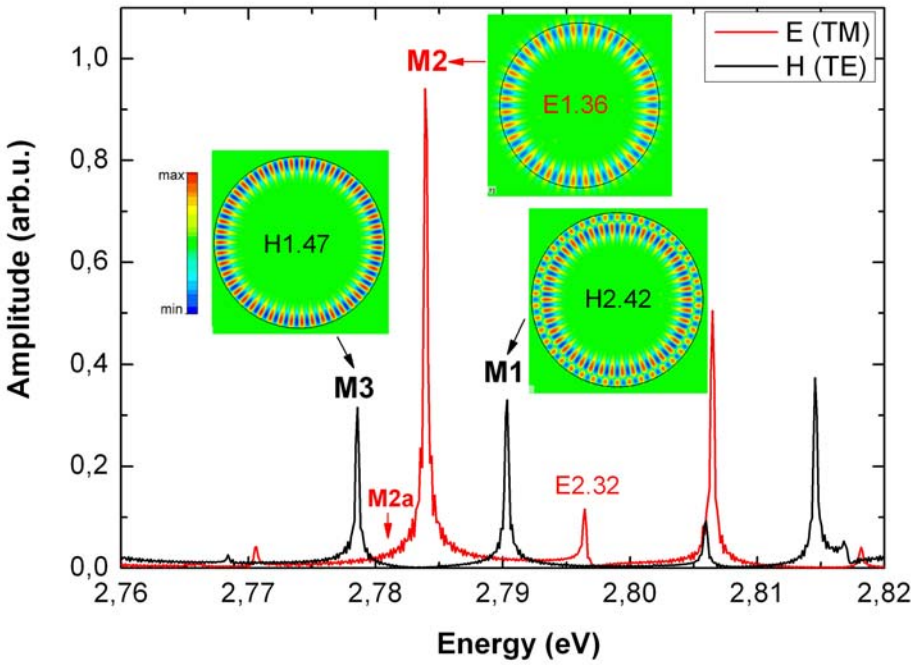

Figure 32. Simulated mode spectra of an ideal disk with 3 µm diameter. The resonances are labeled with TE and TM to indicate their polarization as well as their azimuthal and radial quantum numbers m and n_r respectively. The field distributions of the modes are insetted. Thereby red corresponds to the highest field density and blue is the lowest field density. The black circle indicates the edge of the microdisk.

of states for TES transition. The field distribution of the modes is insetted. Red corresponds to the highest field density and blue is the lowest field density. The black circle indicates the edge of the microdisk. In summary, the observed emission of the disk is in quite good agreement with the calculated modes.

Also for a 3 µm disk, the intensity of the lasing modes was determined and plotted versus the excitation power in a double-logarithmic scale. Figure 33 shows the integrated intensity of the lasing modes M1 (a), M2 (b), and M3 (c) for the disk with 3 µm diameter versus the excitation power density. The curves show the typical intensity jump $\propto\beta^{-1}$ from below to above threshold. The observed super-linear increase starts at the lowest excitation power for modes M1 and M2. The corresponding threshold of M1 and M2 was below 8 Wcm^{-2}. The mode M3 with an even higher threshold comes up for a stronger excitation of about 15 Wcm^{-2} as can be seen from the spectrum (c) in Figure 33. Also in this disk, higher order guided modes compete for gain. At the lower excitation intensity mode M1 is dominant. As the pumping intensities exceed 14 Wcm^{-2}, the main intensity of the primary mode M1 is transferred to mode M2. Thereby the decrease of intensity of M1 and the increase of intensity of M2 is observed. For the excitation density exceeding 17 Wcm^{-2}, the

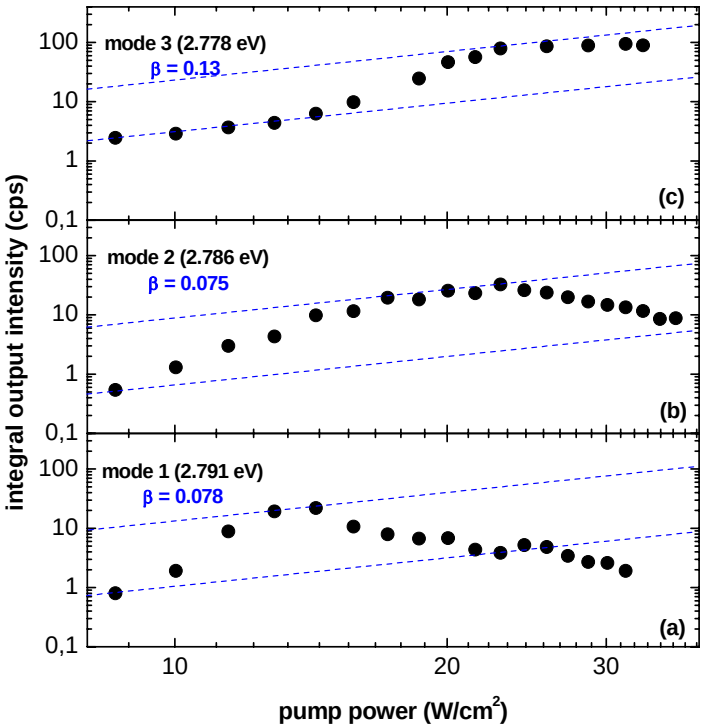

Figure 33. Integrated intensity of the three lasing modes of a 3 µm disk vs. the excitation power density in a semi-logarithmic scale. Filled circles are the measured data, red solid lines are the fit curves according to Eq. 28 and the blue dashed lines are asymptotes for low and high power. The onset of lasing of mode 3 is observed at a threshold of about 15 Wcm^{-2}.

transfer of the intensity from M2 into M3 is assessed. The intensity of M2 first saturates and then decreases slowly whereas the intensity of M3 rises. Lower energy modes with even higher thresholds come up for higher excitation. This dependence of the laser threshold on the mode energy can be explained by the shift of the cavity mode energies into resonance with spontaneous emission and by increasing of the probability of TES transitions with increasing excitation power. This was discussed in detail for a 6 µm disk. The β factor was found to be 0.13, 0.075 and 0.078 for modes M1, M2 and M3, respectively.

The relationship of emitted intensity and excitation power for semiconductor microcavity lasers was derived by using Eq. 28 and is shown in Figure 34. The input-output characteristics are best reproduced with the parameters shown in Table 2.

Parameter	Mode 1	Mode 2	Mode 3
γ	0.05	0.01	0.07
β	0.09	0.1	0.095
ξ	12	10	13,8

Table 2. Parameter for the fits of the threshold using Eq. 28 for the modes observed in 3 µm disk.

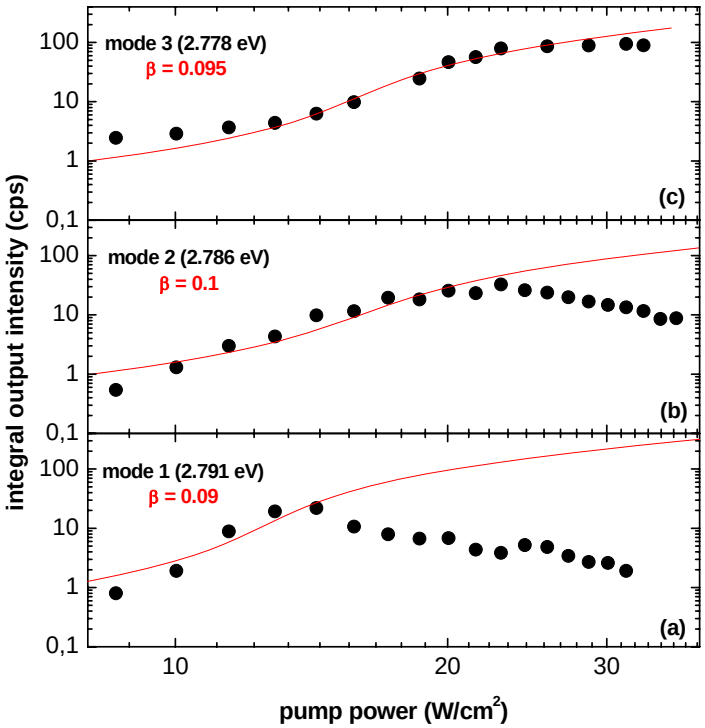

Figure 34. Integrated intensity of the three lasing modes of a 3 µm disk vs. the excitation power density in a semi-logarithmic scale. Filled circles are the measured data, red solid lines are the fit curves according to Eq. 28 and the blue dashed lines are asymptotes for low and high power. The onset of lasing of mode 3 is observed at a threshold of about 15 Wcm^{-2}.

The parameter values of the three fits lying very close to each other as well as the measured thresholds for the modes. Again the experimental characteristic is not perfectly reproduced by this model due to a modified source term of spontaneous emission and Coulomb effects, multimodes and possible full inversion. This explains the deviation of theoretical model and experimental results

The energy positions and the linewidth of the modes were analyzed as a function of the pump power density. Figure 35 shows the energy shift of the three modes as a function of the excitation power. At lower excitation the energy of M1 increases until an excitation of 15 Wcm^{-2}. After this the energy of M1 decreases to an initial value and from about 21 Wcm^{-2} rises again. This indicates mode hopping to higher order modes. The energy of M2 and M3 increases continuously by about 2.2 meV and 4.6 meV, respectively. Here no mode hopping was observed. The blue shift of the cavity modes is associated with a carrier induced change of the refractive index, which, in turn, modifies the energy position of the cavity modes [82].

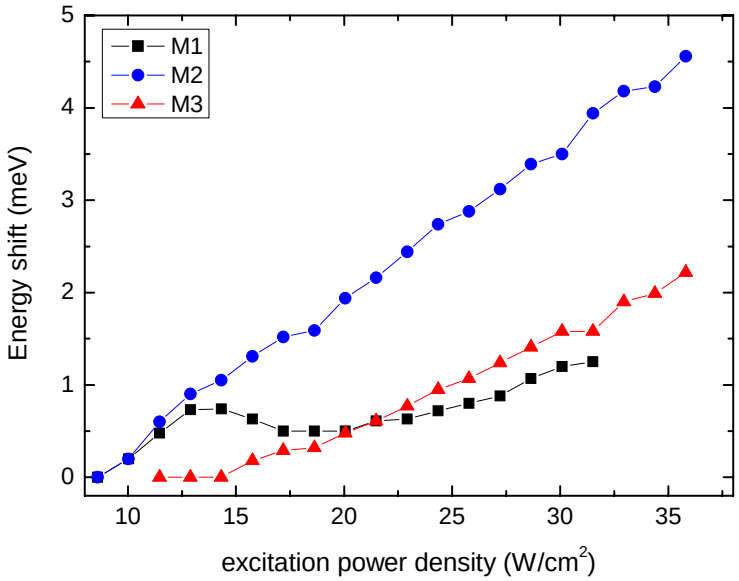

Figure 35. Energy shift of the modes 1, 2 and 3 of a 3 µm disk as a function of pump power density.

Figure 36 shows the linewidth of the modes as a function of the pump power density. The linewidth of M1 rises from 0.92 to 1.53 meV until 15 Wcm^{-2}, then decreases about 20% and then rises continuously to a value of about 2 meV. The linewidth of M2 rises at small pump power, until 11 Wcm^{-2}, where 40% decrease of the linewidth was observed. With a further increase of the excitation power the linewidth of M2 increases continuously to a value of about 3 meV. At about 11 Wcm^{-2} the linewidth of M3 drops from 2.23 meV to 0.83 meV and afterwards rises slowly with increasing pump power. The significant

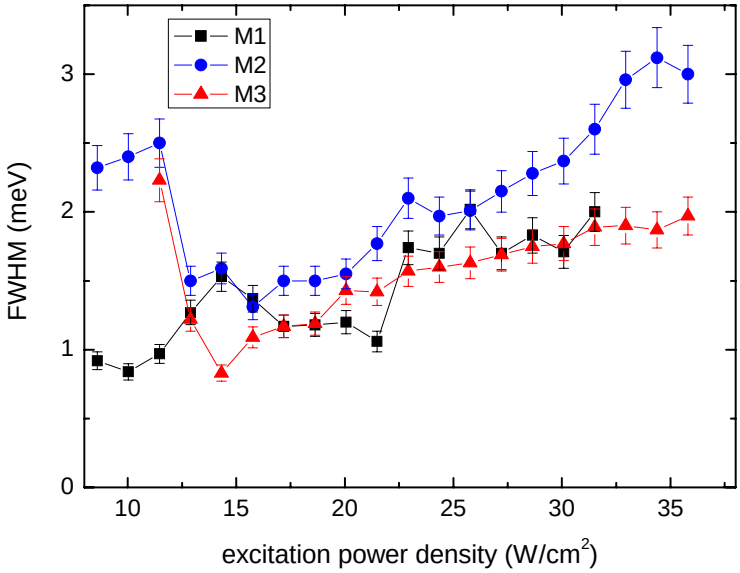

Figure 36. Full width of half maximum (FWHM) of modes 1, 2 and 3 of a 3 µm disk as a function of pump power density.

decrease of the linewidth of the modes indicates the onset of lasing. The linewidth of the modes yields a maximal cavity Q up to 3300. The Purcell factor f_p of the microdisk cavity was calculated using Eq. 22 with experimentally observed Q values and calculated modal volume. The Purcell enhancement factor for a 3 µm disk was found to be about 10.5

In comparison, the cavity modes in the 6 µm disk have smaller energy separation than in the 3 µm disk. This is indicated by mode hopping observed in the 6 µm disk for all lasing modes. These results are in good agreement with the theoretical calculations. We observed $\beta = 0.03$ for a 6 µm and $\beta = 0.13$ for a 3 µm disk for the strongest lasing modes. Hence, the fraction of spontaneous emission coupled into the laser mode in 3 µm disk compared to 6 µm disk, increases about 4 times. The cavity Q value for the 6 µm disk is in the order of 4500 and is higher as for the 3 µm disk, where Q is in the order of 3300. Furthermore, for the 6 µm disk a clear lasing threshold was observed at about 100 Wcm^{-2} and for the 3 µm disk at about 15 Wcm^{-2} for the D^0X-lh TES transition. These thresholds are much lower than for any previous report on lasing in a ZnSe microdisk. The reduction of the threshold for the 3 µm disk relates to the smaller mode volume that increases the Purcell factor from 3.2 for the 6 µm disk to 10.5 for the 3 µm disk.

4 The ZnSe Micro-Membranes

Driven by the proposal of the quantum network [26], the construction of microphotonic circuits, consisting of quantum information devices, enables even more complex functionality. Such circuits consist of arrays of cavities and waveguide structures for interconnection. Nanofabrication makes it possible to realize optical microcavity disk resonators that can serve as low-threshold lasers, as demonstrated in the previous chapter. These resonators can be integrated with other components to form photonic integrated circuits.

High-Q WGM resonances are not accessible by free-space beams and therefore require employment of near-field couplers [85]. Numerous coupling devices, such as high-index prisms [86], side-polished fiber [87], optical fiber tapers [88], and waveguides [89, 90], have been considered for interconnection of MD resonators with other devices in integrated circuits. The principle of all these devices is based on providing efficient energy transfer to the resonant electromagnetic waves in the resonator through the evanescent field of a guided wave or a total internal reflexion spot in the coupler. It is evident, a priori, that efficient coupling can be expected on fulfilment of two main conditions: phase synchronism and significant overlap of the two evanescent fields in the gap between the microcavity and the coupler.

In this thesis, a waveguide structure for ZnSe/ZnMgSe MD was investigated. In this context a fabrication process for ZnSe/ZnMgSe free standing micro-membrane structures was developed. Investigations of the strain and optical properties in such membranes were performed by atomic force microscopy (AFM), μ-RS, and μ-PL measurements. These preliminary investigations demonstrate a step towards the fabrication of membranes for integrated optical waveguide systems. With an additional photonic crystal the membranes have applications like bending waveguides [91], a nanoscale laser with even lower-threshold as MD laser [92, 93], and single photon sources [94].

4.1 Fabrication of membranes

The fabrication process of the membranes consists of several steps. The first step of the device fabrication is the deposition of the ZnSe and ZnMgSe layers on a GaAs substrate by MBE. The detailed growth and characterization of the layers is presented in the previous chapters and will not be discussed here. Based on the experience with the MD fabrication, a similar process was used for the structuring of the micro-membranes. After deposition of the QW films the sample surface was covered with resist, which was structured using electron-beam (e-beam) lithography. Then reactive ion etching and wet chemical etching were used to define the membrane structures. In the following sections the fabrication procedure for membranes is described in detail.

4.1.1. Electron-beam lithography

The e-beam lithography was performed to define the membrane structures. The surface of the sample was cleaned on the spinner by acetone and isopropanol solvents at room temperature followed by nitrogen gas drying. The positive photoresist PMMA8 was then immediately dropped on the sample and spin-coated on the spinner with 5000 rpm for 60 s. Finally, it was post-baked for 90 s on a hotplate at 190°C. The photoresist was exposed by the e-beam in the SEM, where the e-beam was scanned over the resist at 30 kV accelerating voltage, 140 pA current and a spot size of 38 nm. The resist was developed for 35 s in isopropanol and methylisobutylketon (MIBK) solution with a 3:1 ratio respectively. Isopropanol and then DI-H_2O were used as stop-bath.

Rectangular structures with different sizes were defined in the resist. The structures were 20 µm long and 15 µm, 10 µm or 5 µm wide. The length of the rectangles defines the length of the membrane. The distance between two rectangles amounts to 2.5 µm, which defines the width of the membrane.

4.1.2. Reactive Ion Etching

RIE was used to transfer the photoresist pattern into the layers. The applied process parameters are the same as for MD structuring and are described in chapter 3.2.3. Figure 37 shows the SEM photographs of the structures defined by RIE. On the left side, an array

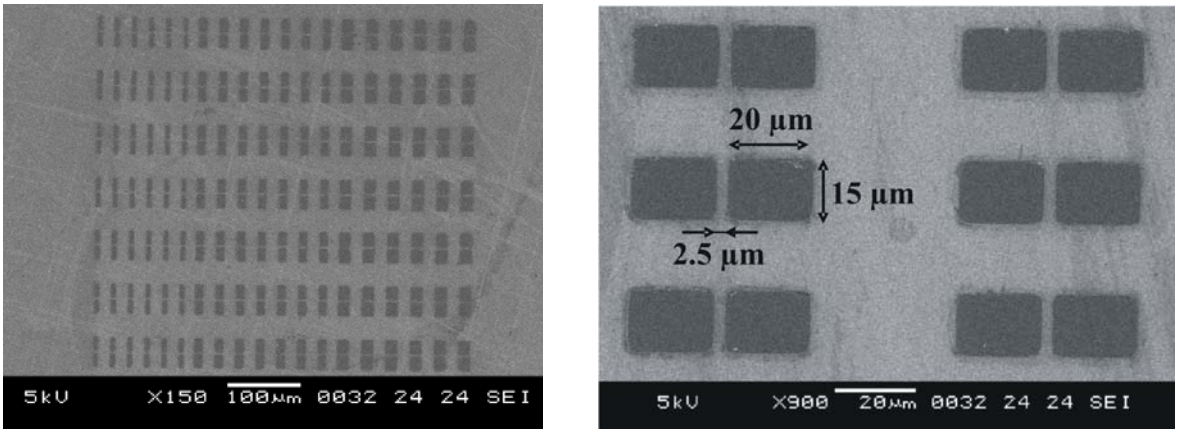

Figure 37. SEM photographs of the structures in ZnSe/ZnMgSe after RIE. On the left side an array of the structures of different sizes is presented. On the right side the pre-membrane structures of 2.5 µm x 15 µm are presented.

of pre-membrane structures of three different lengths (5 µm, 10 µm and 15 µm) is presented. On the right side, the etched grooves (20 x 15 µm) are shown. The pre-membranes between the grooves have a width of 2.5 µm. The SEM analysis of the structures shows that the structures were transferred into the semiconductor layer. The sizes of the structures are consistent with the planned sizes.

4.1.3. Wet chemical undercut

Isotropic selective etching as wet chemical etching is required to undercut the structures. The same undercut process as for MDs was used. For GaAs wet etching, a mixture of 41 ml 1M sodium hydroxide (NaOH) and 9 ml 30% peroxide (H_2O_2) solution was used. This solution was kept at 500 rpm at room temperature for 5 min to stabilize the reaction. Afterwards the rotation speed was decreased to 200 rpm and the patterned sample was immersioned into the solution. The undercut of the membrane structures was carried out in several steps with SEM analysis of the structures between the steps. For every etch step a new etch solution was used. Figure 38 shows the SEM photographs of the 15 µm long membrane after four undercut steps: (a) after 30 s, (b) after additional 10 s (overall time 40 s), (c) after additional 8 s (overall time 48 s), (d) after additional 8 s (overall time 56 s). After the first etch step (a) a free standing structure is observed with a thickness larger than 1 µm. The lower part of the structure has a darker contrast in comparison to the upper surface layer due to the n-GaAs substrate. After the second and third etch step (b,c) the GaAs rest layer under the free standing membrane becomes thinner. After the last etch step (d) the ZnSe/ZnMgSe membrane is free standing and has no GaAs at the bottom side.

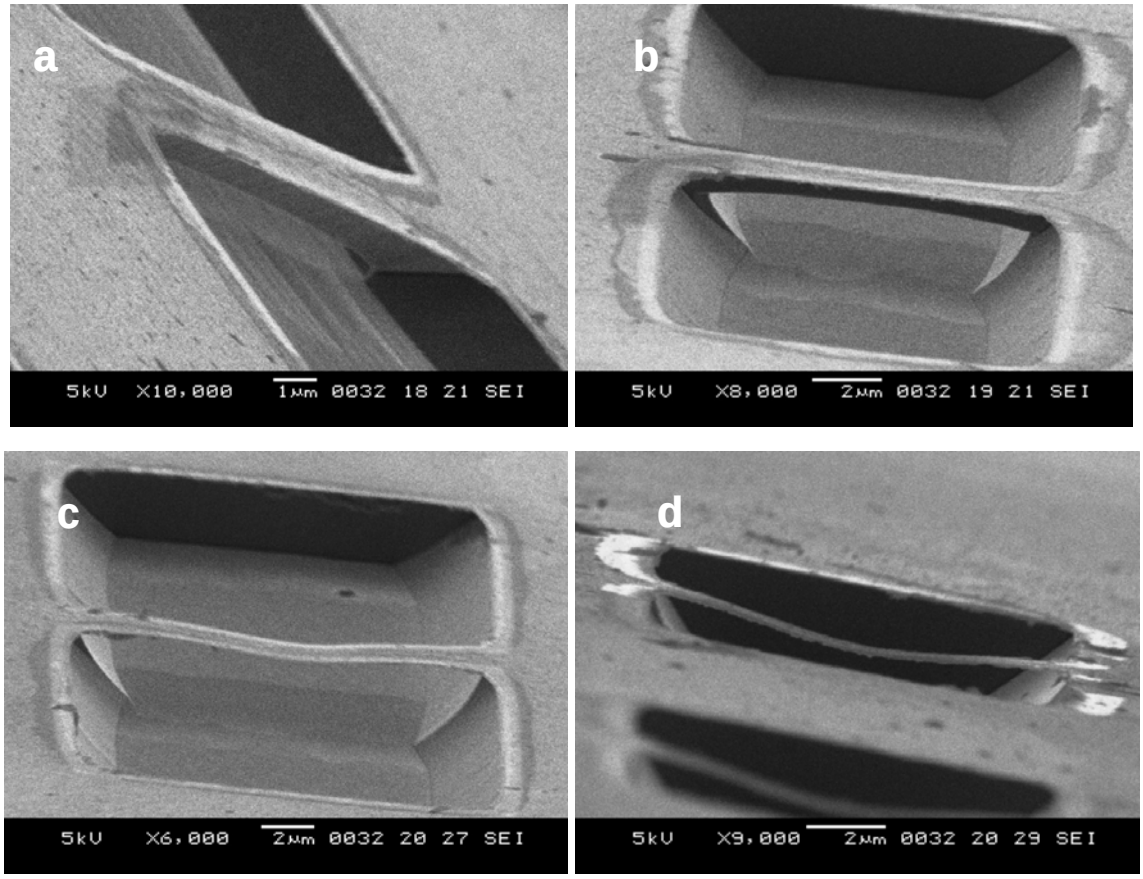

Figure 38. SEM photographs of the 15 µm long membrane after four undercut steps: (a) after 30 s, (b) after additional 10 s (overall time 40 s), (c) after additional 8 s (overall time 48 s), (d) after additional 8 s (overall time 56 s).

Figure 39 shows SEM photographs of the 5 µm long membranes after the fourth undercut step, measured perpendicular to the surface. On the left side, the ZnSe/ZnMgSe layers are not completely free standing and the membrane has GaAs at the bottom. The membrane has the same contrast as the unetched material on the sides of the groove. On the right side, themembrane is brighter as the ambient material due to the higher charging effect and thus

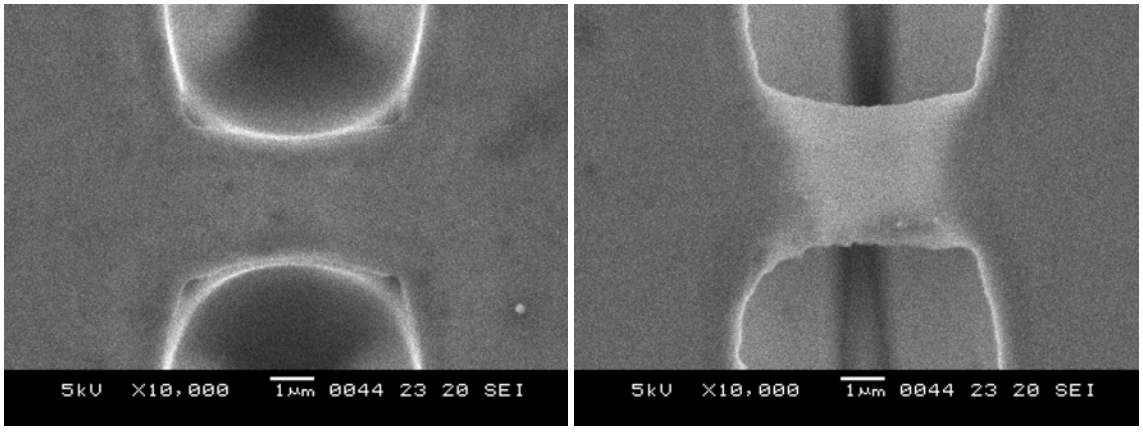

Figure 39. SEM photographs of the 5 µm long membranes after the fourth undercut step. On the left side the membrane has a rest of GaAs at the bottom. On the right side the membrane is free standing.

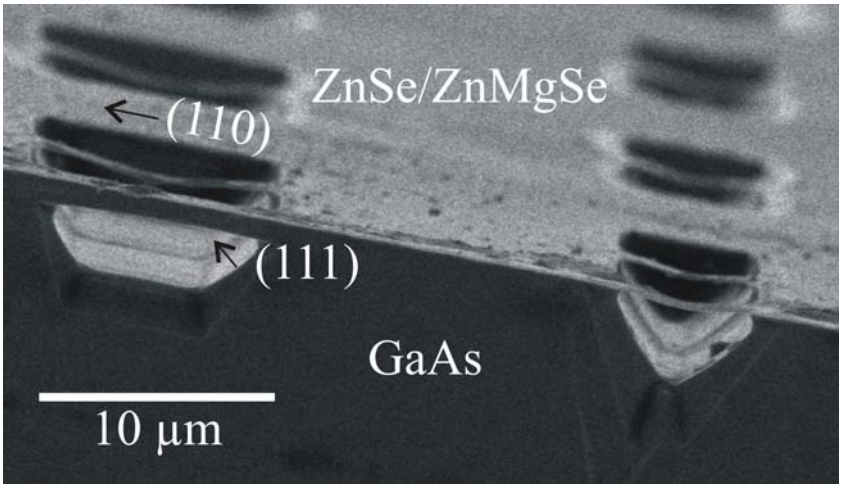

Figure 40. SEM photograph of the ZnSe/ZnMgSe membranes after undercut. The sidewalls of the GaAs grooves are (111) and (-111) oriented.

can be identified as free standing.

Due to the alignment of the membrane structures along the (110), direction the etching was anisotropic. Figure 40 shows the SEM photograph of the ZnSe/ZnMgSe membranes after undercut. The V-shaped grooves were formed in GaAs under the membranes. The sidewalls of the GaAs in the grooves are oriented towards the (111) and (-111) direction.

The free standing membranes reveal a clear bending. This indicates an increase of the membrane size due to the strain release in the layers. To define the degree of relaxation of the layers, further investigations were performed and are discussed in the next sections.

4.2 Structural and optical properties of the membranes

Strain release in semiconductor layers may enhance the performance of the devices due to band gap narrowing as was shown for the MDs. The strain of the membranes is discussed in this section.

4.2.1. Investigations by atomic force microscopy

The bending of the membrane layers were investigated by atomic force microscopy (AFM). The measurements along the structures were carried out at NT-MDT on 15 µm, 10 µm and 5 µm long membranes. Figure 41 shows an example of an AFM line scan along a 10 µm long membrane. A clear bending of the membrane of about 570 nm depth in the middle was observed. For the 15 µm and 5 µm long membranes, the bending depth in the

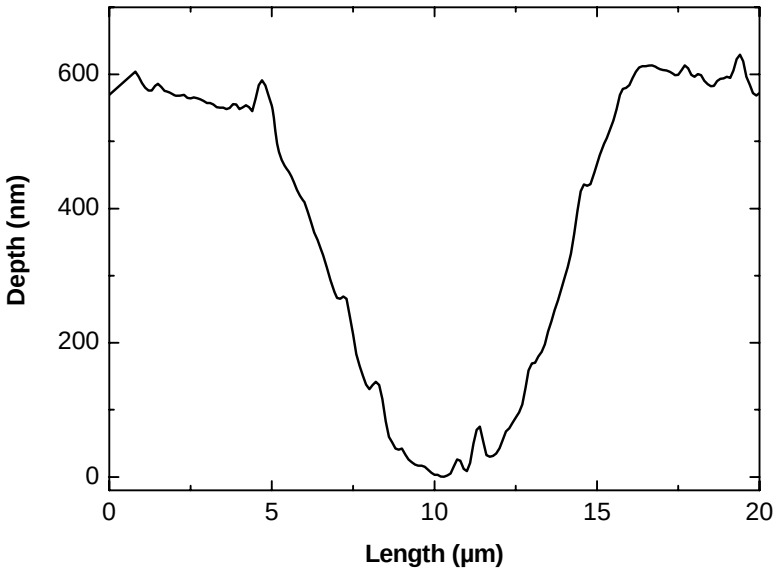

Figure 41. AFM line scan along the 10 µm long membrane.

middle was measured to be 850 nm and 350 nm, respectively. Hence, the bending increases linearly with the membrane length.

The lattice parameter of ZnSe (a_{ZnSe} = 0.5668 nm) and of ZnMgSe (a_{ZnMgSe} = 0.56906 nm) with a Mg content of about 9% is larger than that of GaAs (a_{GaAs} = 0.5653 nm). Therefore the epitaxial growth of ZnSe and ZnMgSe on (001) GaAs will produce a biaxial compression of the unit cell of ZnSe and ZnMgSe along the x- and y-directions, which are parallel to the grown surface. By removing the GaAs, the strain in the membrane structure is released resulting in a lattice parameter between a_{ZnSe} and a_{ZnMgSe}. Due to the larger lattice constant of ZnSe and ZnMgSe in comparison to GaAs, relaxation leads to an increase of the membrane volume. Thus, the length of the membrane increases resulting in the observed bending.

From the amount of the increased membrane length the lattice parameter a_{free} of the free standing membrane can be calculated from the relation:

$$\frac{l}{a_{GaAs}} = \frac{l_{free}}{a_{free}} \qquad \text{Eq. 29}$$

where l is the length of the strained membrane, l_{free} is the length of the freestanding membrane. Thus, with the measured membrane length l and l_{free} by AFM the pseudomorph lattice parameter for a released membrane was calculated. In Table 3 the results of the AFM measurements for the membrane length and the calculated lattice parameter are presented.

Strained membrane length l	Released membrane length l_{free}	Lattice parameter a_{free}
5 µm	5.05 µm	0.5706 ± 0.005 nm
10 µm	10.08 µm	0.5700 ± 0.005 nm
15 µm	15.12 µm	0.5699 ± 0.005 nm

Table 3. Measured membrane length l and l_{rel} and calculated lattice parameter of a free standing membrane.

For all membranes we obtained a lattice parameter that is nearly identical with the ZnMgSe lattice parameter with a Mg content of about 9% within the experimental error, indicating full relaxation of the ZnMgSe layer in the freestanding membranes. Considering the volume ratio of ZnSe and ZnMgSe, ZnSe seems to be tensile strained on ZnMgSe. This is a similar effect as was shown for the MDs in the previous chapter, which results in a substantial band gap narrowing of a ZnSe QW.

4.2.2. Micro-Raman spectroscopy

Raman spectroscopy is a suitable technique for strain investigations in semiconductor microstructures as shown for MDs in chapter 3. In this section, a detailed study of the strain distribution and extended defects in the membranes performed by high spatial and high spectral resolution µ-RS is performed.

Figure 42 shows a series of Stokes-Raman spectra recorded at different spots on a 10 µm long membrane. Schematically Raman probing locations are shown in the insetted SEM image of the membrane. Several peaks can be distinguished. The peak at a frequency of about 252 cm^{-1} results from the LO mode of the ZnSe layer and the peak at about 292 cm^{-1} corresponds to the LO phonons of GaAs. At about 269 cm^{-1} the plasma-phonon coupled mode (L^-) at the ZnSe interface is observed. The ZnSe LO phonon frequency outside the membrane (area 1) and at the edge of the membrane (area 2) is at 253.6 cm^{-1} and 252.2 cm^{-1}, respectively. At the intermediate area (area 3) and in the middle of the membrane (area 4) corresponding LO frequencies were observed at 251.4 cm^{-1} and at 251.1 cm^{-1}, respectively, yielding a frequency shift of ZnSe LO phonons of 2.5±0.5 cm^{-1} from the centre to the edge area of the membrane. For reference, the arrow shows the frequency of ZnSe LO phonons at 252.0 cm^{-1} measured with a fully relaxed 2 µm thick "bulk like" ZnSe layer on (001) GaAs. The width of the LO ZnSe Raman line in the centre and at the intermediate area of the membrane is comparable with the line width of strained ZnSe layers in the order of 7 cm^{-1}.

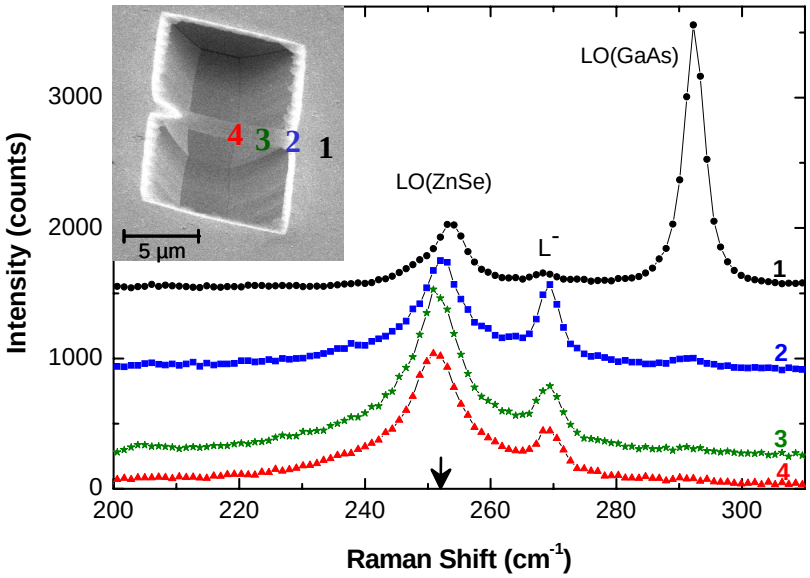

Figure 42. Raman spectra of the LO phonons recorded at four different spots along the 10 µm long membrane. Schematically Raman probing locations are shown in the insetted SEM image of such a membrane. The arrow indicates the LO phonon frequency of bulk ZnSe.

We suggest that the shift of the LO phonon peaks of ZnSe to higher frequencies arises from in-plane compressive strain in the ZnSe layers due to the lattice mismatch between the GaAs substrate and the layer. A model for calculation of the shift was presented in chapter 3. Thereby the relationship between strain and Raman frequency shift was deduced to Eq. 27 $\Delta\omega = -428.2\varepsilon$. By considering that ZnSe is a) compressively strained on GaAs at the area 1, and b) tensile strained on ZnMgSe in the middle (area 4) of the membrane, we obtain $\varepsilon = -6.44\times10^{-3}$ and hence $\Delta\omega = 2.76$ cm^{-1} for ZnMgSe barriers with a mole fraction of 9% Mg. In our experiment we observed a slightly smaller frequency shift of the LO phonons probably due to a slightly lower Mg content in the barrier layers. However, the calculated value for the LO phonon shift is in agreement with the measured value within the experimental error, supporting the model of a relaxed free standing layer system in the middle of the membrane.

The ZnMgSe alloy with 9% Mg concentration is expected to have ZnSe-like and MgSe-like LO phonons with 247 cm^{-1} and 308 cm^{-1} frequency, respectively [73]. The MgSe-like mode is quasi negligible due to the small fraction of Mg in the crystal, while the ZnSe-like mode is considerably weaker as the ZnSe LO line from ZnSe and could not be resolved in our spectra.

The distribution of strain in the micro-cavity is depicted in Figure 43, where the Raman shift of the ZnSe LO peak is plotted vs. position on the 10 µm long membrane. Four

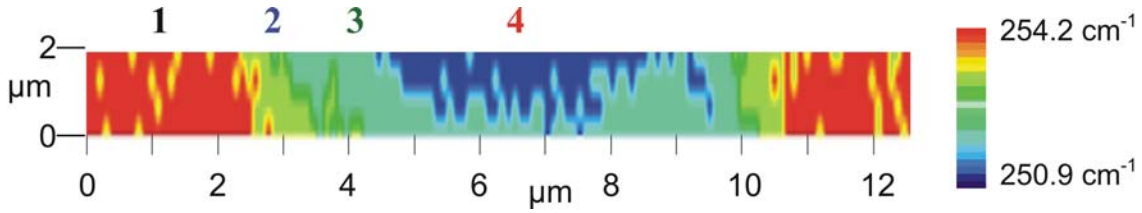

Figure 43. Micro-Raman map of the ZnSe LO phonon peak frequency vs. position on the 10 µm long membrane.

different regions of strain are distinguished. 1) Outside the membrane we find a Raman frequency of pseudomorph strained ZnSe on GaAs. 2) At the intersection of the GaAs we observe a clear frequency redshift of the ZnSe LO phonons. 3) In a region which covers about the inner-half of the freestanding part of the membrane we observe a phonon frequency which corresponds to tensile strained ZnSe on 70% relaxed ZnMgSe. 4) The centre region with a length of about 3 µm shows a distribution of tensile strained ZnSe on fully relaxed ZnMgSe. Therefore we observe a continuous strain release towards the centre part of the membrane.

Furthermore, no TO phonon Raman line across the whole area of the membrane was observed. As was shown by D. Olego and M. Cardona [77], the existence of the TO phonon line in the RS spectra of (001) oriented samples is related to defects in the samples. Thus the absence of TO phonon lines in the Raman spectra is a strong indication that the density of extended defects in the membrane area is negligible.

4.2.3. Micro-photoluminescence

The previous investigations show that the ZnSe QW is tensile strained on ZnMgSe in the central part of the freestanding membranes. As a result of the strain variation from compressive to tensile, the relative positions of the FX-lh and FX-hh energies are reversed and a substantial band gap narrowing of the ZnSe QW along the membrane from the edge to the centre part occurs as is shown schematically in Figure 44. The bandgap narrowing in the direction of the membrane centre can enhance the charge carrier transfer to the central part of the. The PL investigations can give more information about these effects.

The µ-PL spectroscopy was performed for the optical characterization of the membranes. Figure 45 shows µ-PL spectra taken at 5K of an ZnSe/ZnMgSe QW membrane with 10 µm length measured at different positions from outside to the centre, as indicated in the SEM image (inset). For clarity, the intensities were normalized to the

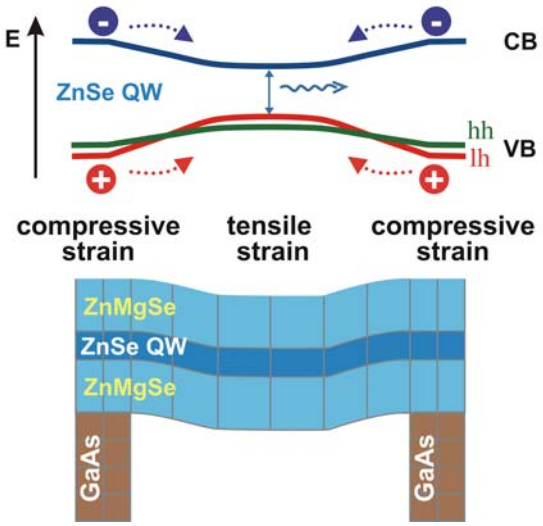

Figure 44. Schematical sketch of the strain in the multilayers in the membrane and resulting bandgap narrowing over the membrane.

particular maximum of the spectra and the spectra have been shifted by vertical offsets. At the unstructured part (position 1) we observe typical peaks for the ZnSe/ZnMgSe QW pseudomorph on GaAs. The peaks at 2.8067 eV and 2.8018 eV correspond to the FX-hh and D^0X-hh transitions, respectively. By scanning the excitation spot from the edge to the centre of the membrane (positions 2 to 4) the emission bands are red shifted. The corresponding transition energies are obtained by fitting the emission band in the centre of

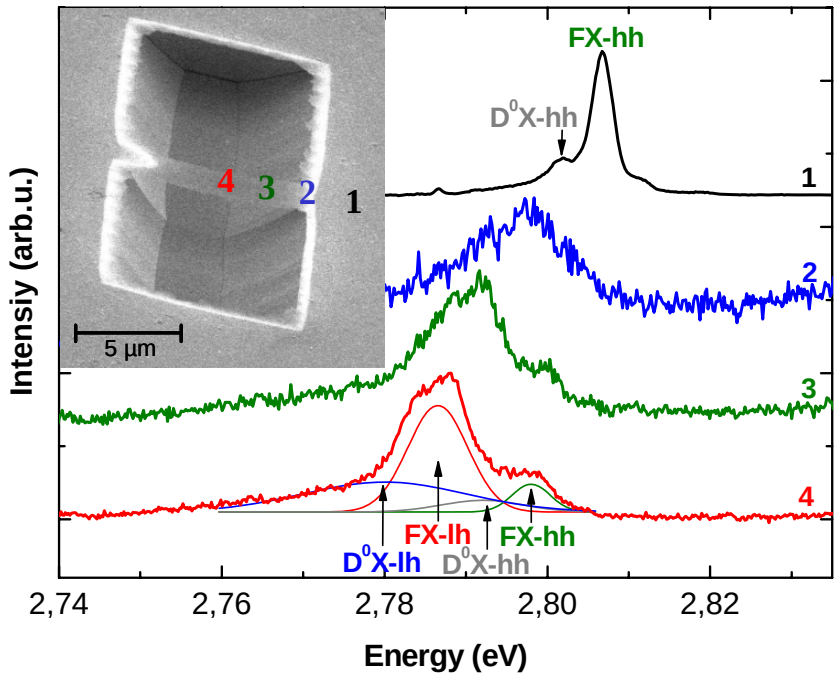

Figure 45. PL spectra taken at 5 K with cw-laser excitation for a membrane with 10 µm length. Inset: SEM micrograph of such a membrane. The areas of excitation locations are indicated.

the membrane by four Gaussian peaks. We assume that the largest peak at 2.786 eV corresponds to the FX-lh and the peak at 2.798 eV to the FX-hh transition. The hh and lh transitions of D^0X are detected at 2.792 eV and 2.78 eV.

By moving the excitation spot from position 1 to the centre of the membrane, the intensity of the FX-hh and D^0X-hh transitions is reduced. In contrast, the emission intensity of the FX-lh and D^0X-lh transitions is enhanced resulting in an overall redshift of the PL spectra. This observation is in good agreement with the assumption that ZnSe in the central part of the membrane is tensile strained, thus the lowest energy transitions are the lh-related.

The emission intensity varies with the position on the membrane. Figure 46 shows the energy (black) and the intensity (blue) of the FX-hh and FX-lh transitions as a function of the position on the membrane. The hollow circles/squares indicate the FX-hh and the filled circles/squares FX-lh transitions. The intensity is normalized to the values of the strained ZnSe QW on GaAs outside the membrane (position 1). At this position the FX-hh transition is dominating. At the membrane edge (position 2) we observe the broad emission band where FX-hh as well as FX-lh transitions contribute to the PL. The FX-hh energy is redshifted by 2 meV. The FX-lh transition has a lower energy than the FX-hh, which indicates a tensile strained ZnSe QW. The intensity of FX-hh transition measured outside

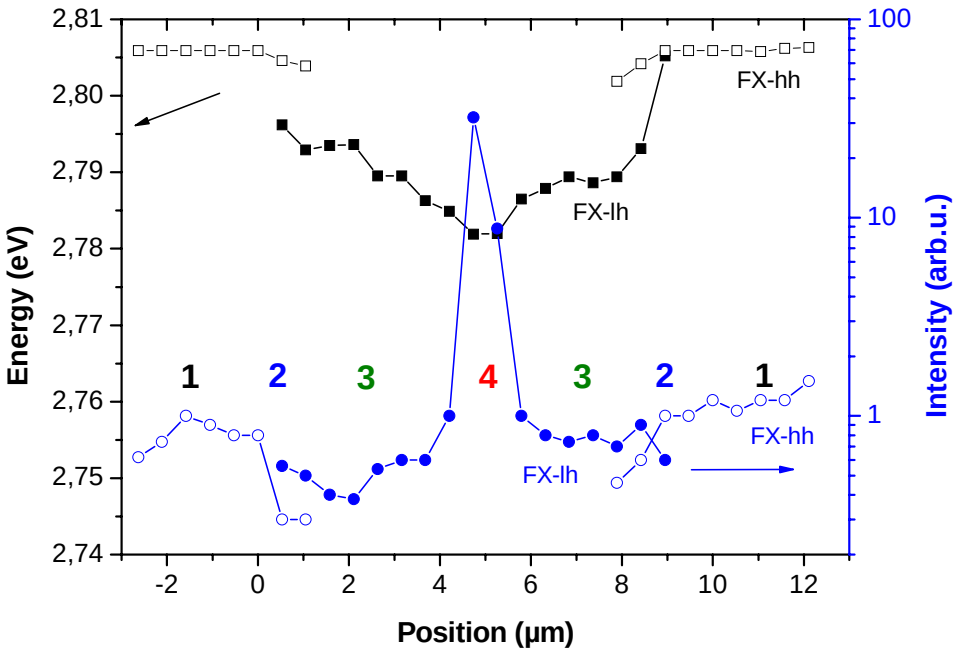

Figure 46. FX-lh (filled circles/squares) and FX-hh (hollow circles/squares) energy shift (black) and intensity (blue) as a function of the position on the 10 µm long membrane taken at 5 K with cw-laser excitation of 7 kW/cm^2. The intensity is normalized to the values outside the membrane (position 1).

the membrane splits at the edge of the membrane into FX-lh and FX-hh transitions, where the FX-lh transition becomes dominating. At the intermediate part (position 3) of the membrane the FX-lh transition dominates in the spectrum. The energy of the transition shifts to lower energies, indicating further release of the strain. The intensity of the transition is about 50% lower than the intensity of the FX-hh transition outside the membrane, since excess carriers are transported from this area into the direction of the lower energy in the centre of the membrane. The most interesting part occurs in the middle of the membrane (position 4). At this position the FX-lh transition has the largest redshift and the highest intensity. An increase of the intensity by one and a half order of magnitude is observed. This effect results most likely from carrier transport towards the middle of the membrane due to the bandgap narrowing as shown schematically in Figure 44. More detailed investigations of this effect can be done by exciting the charged carriers in position 1, 2 or 3 and measuring the PL at position 4 in the middle of the membrane. However, this requires a special experimental setup with a spatial resolution down to a focus with 1 μm diameter and independently for the excitation as well as the detection. The realization of this experiment is in the progress.

In summary, freestanding ZnSe/ZnMgSe membranes with a length of up to 15 μm and a width of 2.5 μm were successfully fabricated. The investigations of the strain distribution in these membranes by μ-RS and μ-PL indicate the release of strain without generation of defects towards the centre of the membrane. The strain release results in a bandgap narrowing and thus in an enhanced carrier transport towards the centre of the membrane, which enhances the PL efficiency. These preliminary investigations demonstrate a step towards integrated optical waveguide systems. With an additional photonic crystal the membranes are suitable for fabrication of a nanoscale laser with even lower-threshold as MD laser [92, 93] and single photon sources [94].

5 The ZnSe/CdSe Nano-Photodiode

The concept of the optical and electrical manipulation of quantum-states on the nano-scale and their applications in quantum information systems has recently become a challenging topic in physics. One approach to investigate semiconductor qubits makes use of a two-level system which is formed by the exciton ground state in a single quantum dot (QD). With individual QDs enclosed in a Schottky photodiode (PD) with a near-field shadow masks on a semi-transparent contact, electrical and optical access is provided to probe and to modify the quantum state of QD excitons. With a well-defined resonant laser pulse (i.e., a π-pulse) acting on the ground state of a QD, the exciton-qubit can be controlled, as shown in Figure 47. Hence, the qubit can be switched from the initial state $|0\rangle$ (no exciton) to $|X\rangle$ (one exciton). Transitions between both states can be induced by resonant optical driving fields, where the energy ħω of the optical excitation corresponds to the energetic level spacing between the states $|0\rangle$ and $|X\rangle$. Coherent optical π-pulse excitation in particular then results in an inversion of the two-level system with respect to its initial state: $|0\rangle \leftrightarrow |X\rangle$. Furthermore, by modification of the laser pulse parameters (between 0 and π) an arbitrary superposition of the two final states $a * |0\rangle + b * |X\rangle$ can be prepared. After the qubit preparation, a readout of the quantum state is possible by measuring the resulting photocurrent (PC) of the PD when a reverse bias is applied to the diode. Thereby the QD is resonantly excited, but instead of a radiative recombination, the charge carriers are forced to tunnel out of the QD and contribute to a PC which is detected with a high resolution current measurement. The key-feature of this proposed device is the performance as a quantum gate, which provides extremely fast quantum state manipulation

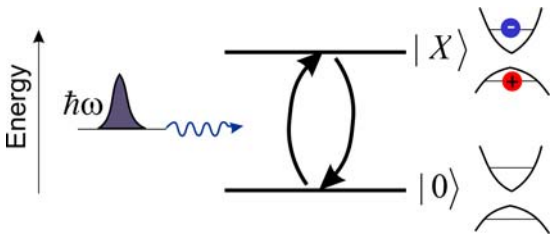

Figure 47. Schematic view of an excitonic two-level system in the ground state of a semiconductor QD. The state $|0\rangle$ corresponds to an empty QD, $|X\rangle$ to a one-exciton occupancy.

with photons as well as an electrical read-out within several picoseconds.

Recently, clear evidence for the successful manipulation and readout of the quantum state of an exciton in a single InGaAs/GaAs QD PD was demonstrated [95, 96, 97]. The relevant time scale for the coherent manipulations is basically determined by the dephasing time τ_2, the radiative recombination time τ_{rec} and the time constant of the tunneling escape τ_{esc}. For an efficient electric readout, the tunneling process must be significantly faster than the radiative recombination ($\tau_{esc} < \tau_{rec}$). In the InGaAs/GaAs QD photodiode system, the exciton lifetime is about $\tau_{rec} = 1$ ns and the dephasing time is between $\tau_2 = 600$ ps at 4 K and several picoseconds at higher temperatures (up to 77 K) [98]. Due to those time parameters, a sufficient conservation of the quantum state and its manipulation via laser pulses is limited to temperatures well below 77 K (liquid nitrogen). Furthermore, to perform a maximum number of coherent manipulations within the dephasing time, the duration of the excitation pulse has to be as short as possible. Hereby, simultaneous resonant pumping of the exciton and biexciton transitions has to be avoided to preserve the integrity of the single exciton qubit, which is considered here. Therefore, the spectral linewidth of the excitation pulse has to be significantly smaller than the exciton/biexciton energy splitting. However, the spectral line width of the light pulse increases with decreasing pulse duration. Thus, the excitation laser pulse width is limited to 2-4 ps in InGaAs/GaAs QD PDs (corresponding to a typical biexciton binding energy of about 3 meV).

In CdSe QDs the biexciton binding energy is known to be considerably higher, about 25 meV [99]. This allows a significant decrease of the excitation pulse duration by nearly a factor of ten, without any perturbation of the two-level-system qubit. Due to the higher confinement energies in CdSe/ZnSe QDs [100], the operation of such a device may also be possible at higher temperatures [101] as compared to typical GaAs-based III-V quantum systems. In this work, a detailed study of the general parameters of CdSe/ZnSe QD PDs is presented. In particular, we determined the critical electric field for the transition from PL to PC in CdSe/ZnSe QD PDs.

5.1 Fundamentals of single quantum dot photodiodes

In this section, the basic properties of a PD device are presented. As an example of the used CdSe QD PD.

5.1.1. Sample structure and electric field

Figure 48 (a) shows the schematic structure of a typical photodiode with CdSe QDs. Above the n-doped GaAs substrate, an n-doped ZnSe layer was deposited to reduce the band bending at the heterojunction, followed by an intrinsic ZnSe layer with embedded CdSe QDs. On top of these layers a semitransparent gold Schottky contact was processed. To address only a single QD by laser excitation, a near field aluminium shadow mask restricts the excitation region. Figure 48 (b) shows the calculated (1D Poisson solver) band diagram of the photodiode with applied bias voltage of –1V. The electric field applied to the QD is an important feature of the photodiode. For an n-i-Schottky diode, the electric field can be calculated as a function of the bias voltage V_{bias} and the distance d between the back contact and the Schottky contact:

$$F = \frac{V_{build-in} + V_{bias}}{d} \qquad \text{Eq. 30}$$

This equation is only correct for moderate voltages and as long as there is no current flow and no charges are trapped inside the QDs or the wetting layer. However, for the interesting reverse bias voltage region (here between 0V and -5V) the Eq. 30 can certainly

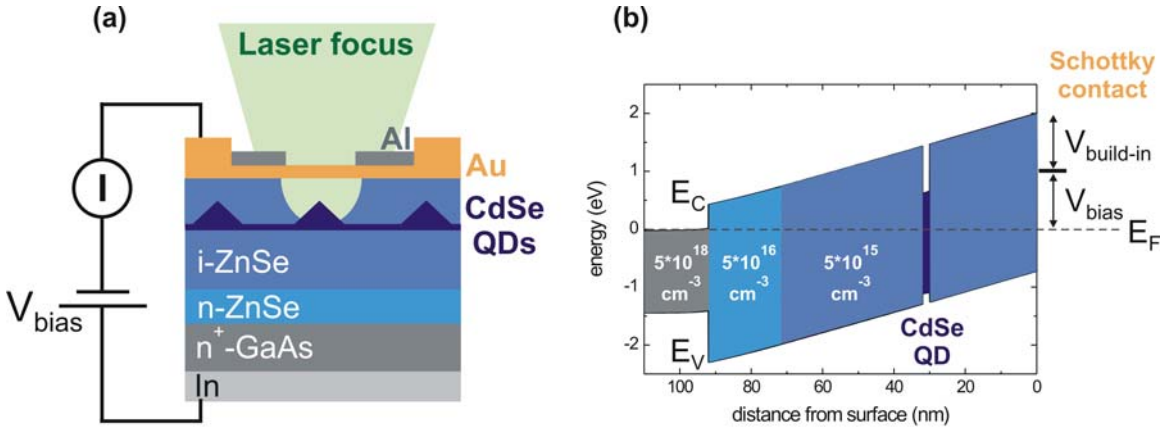

Figure 48. (a) Schematic cross section of a layer structure of the photodiode based on CdSe QDs for the voltage dependent PL. (b) The calculated band diagram of the photodiode with CdSe QD with an applied reverse bias voltage of –1V.

be applied.

5.1.2. Quantum confined Stark effect

The quantum confined Stark effect (QCSE) describes the redshift of the exciton energy due to the presence of an external electric field. The electron and hole which form the exciton are pulled in opposite directions by the applied electric field, as shown in Figure 49. The applied electric field normal to the QDs has several effects [102, 103]; firstly the decrease of the energy of the carrier wave function due to the "tilt" of the confinement potential. Therefore the wave functions of electron and hole are spatially separated, the exciton is polarized and forms a dipole. Secondly the decrease of the exciton binding energy based on the reduced overlap of the electron and hole wave functions. Thirdly the change in the exciton oscillator strength due to the modified overlap between the wave functions. And the last impact is the broadening of the absorption line at high applied fields due to field ionization processes.

In a first approximation, the decrease of the exciton energy is proportional to electric Field square (F^2):

$$E_X = E_X(F=0) - \mu_{el} F - \alpha F^2 \qquad \text{Eq. 31}$$

where μ_{el} is the permanent dipole moment and α the polarizability of the exciton [104]. At high electric fields the induced dipole moment is limited due to the confinement of the electron and hole inside the dimensions of the QD. Then the QCSE becomes linear with increasing electric field.

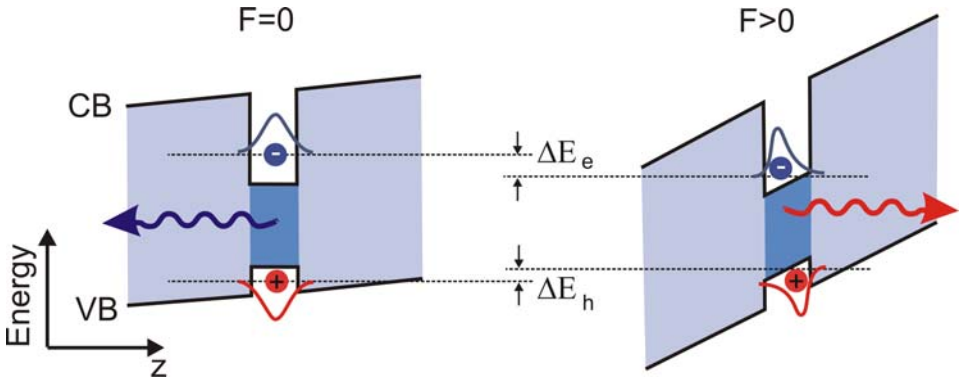

Figure 49. Schematic view of the quantum confined Stark effect. Left: without applied electric field; right: applied electric field. Deformation of the electron and hole wave functions due to the external electric field causes the reduced transition energy of the exciton.

5.1.3. Tunneling

An exciton in the QD located in the photodiode can decay via two competing processes: radiative recombination and tunneling. The radiative recombination time of an exciton (in CdSe QDs about 290 ps [105]) does not depend very strongly on the electric field and can be assumed constant for a specific QD. Instead of recombining, the electron and hole can tunnel through the barrier to the back contact or the Schottky contact, respectively, as shown in Figure 50. The corresponding photocurrent can be detected. At a certain electric field, the tunneling time becomes shorter than the radiative recombination time. This means that the tunnelling of the exciton from the QD becomes more probable than the radiative recombination. The ratio between tunneling decay and radiative recombination is simply determined by the according time constants. The tunneling time depends on the barrier width, which is strongly field-dependent, and on the effective mass of the charge carrier. The tunneling time of the electron and the hole can differ due to the higher effective mass of the hole. Nevertheless, after one of the charged particles has tunneled, the other charged particle has no counterpart to recombine and therefore tunnels subsequently.

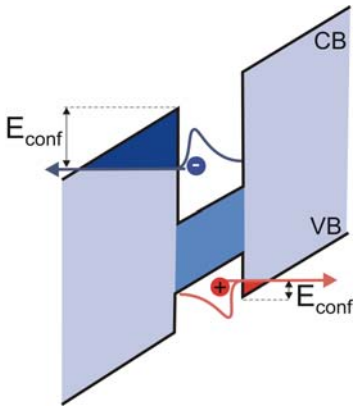

Figure 50. Tunneling of electron and hole from a QD.

A rough estimation of the tunneling rate can be modelled by using an adiabatic approximation with decoupled z (parallel to the field) and x, y (in the growth plane) motion. Within this approximation, the tunnelling probability depends only on the z part of the wave function, and can be modelled using a one-dimensional (1D) Wentzel-Kramer-Brillouin approximation. For a 1D confining potential of width *a* in a perpendicular field F, the tunnelling rate is given by [106]:

$$\frac{1}{\tau_t} = \frac{\hbar\pi}{2m^* a^2} \exp\left(\frac{-4}{3eF\hbar}\sqrt{2m^* E_{conf}^3}\right) \qquad \text{Eq. 32}$$

where τ_t is the tunneling time, $\hbar$ the Planck's constant, m^* the effective mass of the charged particle, e the elementary charge, F the applied electric field, and E_{conf} the confinement energy.

5.2 Fabrication of CdSe QD photodiodes

Samples with the CdSe QDs were grown in the MBE system as described in chapters 2 and 3. Figure 51 (a) shows a schematic view of the multilayer structure. The n-doped (2×10^{18} cm^{-3}) (001) GaAs substrate was overgrown with a 150 nm thick GaAs buffer to achieve a good surface quality. Then a 20 nm ZnSe buffer was deposited. The ZnSe buffer layer was doped by fluorine at a cell temperature of 325°C which results in n-doping of about 5×10^{16} cm^{-3}. This doping concentration is important to reduce band bending at the heterojunction. After that a 40 nm undoped ZnSe layer was grown. After the growing of ZnSe, the sample remained under a selenium atmosphere until the growth of the CdSe layer for the formation of CdSe Stransky-Krastanov QDs [107].

A CdSe layer with a thickness of 2.1 monolayers was deposited on top of the ZnSe layer at a substrate temperature of 270°C. The growth process was monitored by RHEED intensity oscillations of the specular spot in the [-110]-azimuth. This procedure was the same as for the ZnSe layer. At the end of the deposition, the cadmium cell was closed and the layer remained under selenium atmosphere. A highly strained two-dimensional wetting layer was formed. Raising the substrate temperature increases the overall energy of the system, which can be divided into surface energy and strain energy. At a sufficient substrate temperature it becomes more favorable for the system to form three-dimensional (3D) islands with reduced strain than to remain two-dimensional. This phase change can be observed in-situ: the RHEED pattern changes significantly and additional 3D-reflexes occur. The increase of the temperature was done step-by-step by 10°C every 5 minutes until 340°C was reached. The 3D-QDs were then overgrown with a 30 nm thick ZnSe layer at a substrate temperature of 290°C.

For the 2.1 monolayers of the CdSe wetting layer, the QD island density is about to 10^9 cm^{-2} [108]. For this QD density the use of a shadow mask is essential to select individual QDs for a detailed photocurrent spectroscopy. Figure 51 (b)-(f) shows schematic cross-section drawings of the processing steps of a QD PD, that are described in detail below.

Figure 51 (b): To decrease the Schottky diode area, 100 nm silicon dioxide (SiO_2) was deposited by plasma enhanced chemical vapor deposition (PECVD). A gas mixture of 2% silane (SiH_4) and 98% argon (Ar), and nitrous oxide (N_2O) were induced into the reactor chamber. The gas fluxes were 425 sccm for SiH_4/Ar and 710 sccm for N_2O. The chamber pressure was kept at 1000 mTorr and the power at 20 W, the substrate temperature was

300°C during the deposition time of 1 minute. The following chemical reaction is took place during deposition of SiO_2 [109]:

$$SiH_4(g)+2N_2O(g)\rightarrow SiO_2(s)+2N_2(g)+2H_2(g)$$

with (g) for the gas phase and (s) for the solid phase of educts and products. The gaseous products are pumped off during SiO_2 precipitation on the substrate.

To perform the lithography on SiO_2, the surface of oxide was roughened in the RIE chamber with CHF_3 (10,5 sccm) and Ar (10,5 sccm) gases at 30 mTorr pressure and 150 W

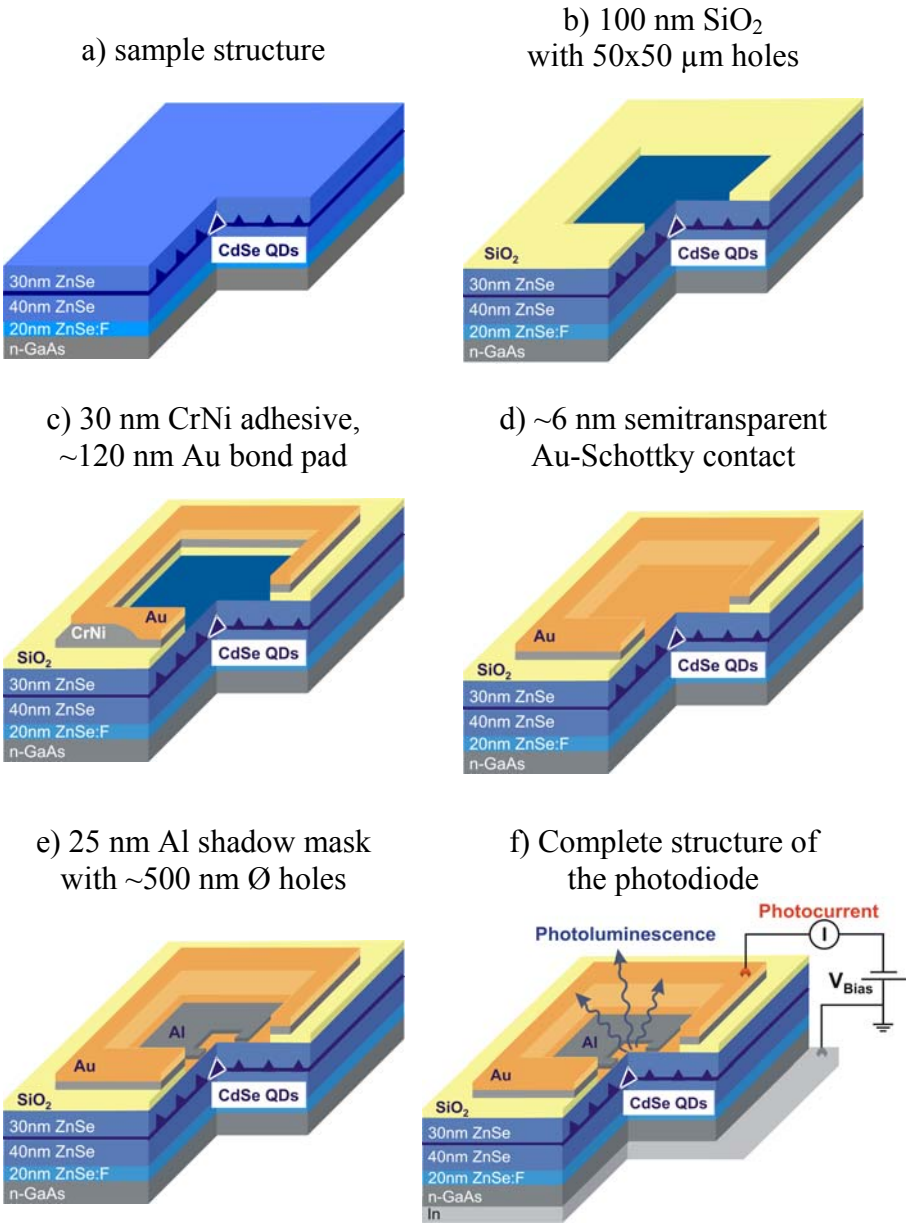

Figure 51. Schematic cross-section drawings of the processing steps of a single QD PD on the basis of a n-i-Schottky diode. Optical access to single QDs is provided by a shadow mask.

power for 5 s. The oxide surface was cleaned with acetone, isopropanol and DI-H_2O. During this process the sample was mounted on the spinner. The AZ 1518 photoresist was spinned for 60 s at 5000 rpm and prebaked on the 105°C hotplate for 60 s. The resist was exposed for 25 s by using a structure projection by a beamer. The resist was developed for 35 s in diluted developer AZ 351 by DI-H_2O with ratio 1:4. The developing reaction was neutralized by DI-H_2O and the sample was dried in nitrogen gas flow. Finally the resist was postbacked for 50 s on the 120°C hotplate.

The obtained structures were transferred into the oxide by wet chemical etching. The following etching solution was used: 2700 ml DI-H_2O, 435 ml hydrofluoric acid (HF) and 900 g ammonium floride (NH_4F) as bumper. The chemical reaction taking place is:

$$SiO_2(s) + 6HF(l) \rightarrow H_2SiF_6(l) + 2H_2O(l)$$

with (l) for the liquid phase and (s) for the solid phase of educts and products. The etch rate of SiO_2 for the given solution is about 12 nm/s, the ZnSe is not affected by the etchant. With this process, holes of about 50 x 50 µm size were etched into the oxide.

Figure 51 (c): For the electrical contact, a bond pad was fabricated as follows. The photolithography was performed as described for Figure 51 (b). For better adhesion of the gold (Au) on the oxide, firstly 30 nm CrNi was deposited by thermal metal evaporation follows by 120 nm Au. Afterwards the lift-off process was performed.

Figure 51 (d),(e): For formation of the Schottky contact and the shadow mask, again first photolithography was performed followed by metal thermal evaporation and the lift-off process. The Schottky barrier was formed by an approximately 6 nm thick semi-transparent Au layer and the shadow mask by 25 nm aluminium (Al) layer on top of the structures. For the spatial isolation of individual QDs, holes with a diameter of about 100 - 500 nm were fabricated in an Al shadow mask using e-beam lithography. The following parameters were used: cleaning with acetone, isopropanol and DI-H_2O; dehydration for 10 min on 130°C hotplate; PMMA 950 A2 resist coating at 5000 rpm for 60s; 90 s pre-bake at 192°C hotplate; e-beam exposure at a bias voltage of 30 kV, 650-fold magnification, working distance of 12 mm, exposure current 80 nA for a spot size of 34 nm, exposure time 64 µs; 20-30 s developing in isopropanol:methylisobutylketon (MIBK) with 3:1 ratio; 30 s post-bake on 125°C hotplate; 10-20 s Al etching in 1% KOH with following neutralisation in DI-H_2O; resist removing with acetone and isopropanol.

Figure 51 (f): The Ohmic back contact was processed by depositing indium (In) on the GaAs substrate on the hotplate. The ohmic and Schottky contacts were bonded with Au wires using ultrasonic bonding.

5.3 Optical characteristics of the photodiodes

The optical properties of the CdSe QDs were investigated by means of μ-PL spectroscopy. Figure 52 (a) shows the typical PL observed in the unstructured region of the sample, where an ensemble of CdSe QDs is excited. The PL of the ensemble of QDs at about 2.28 eV is inhomogeneously broadened to 70 meV. This emission results from a superposition of radiative recombination of shallow (activation energy of 18 meV [110]) and deep (activation energy of 88 meV [110]) localized excitons. The smaller QDs with shallow localized excitons mostly dominate the luminescence on the high energy side, whereas deep localized excitons in bigger dots dominate the luminescence on the low energy side of the spectrum. Some separated lines appear at the low-energy tail of the PL spectrum due to the lower density of the bigger QDs. Figure 52 (b) shows the PL spectrum recorded through a shadow mask. A clearly separated line of an individual QD was observed. The peak at 2.2192 eV labeled (X) is the strongest exciton line, which is assigned to the ground state of an individual QD. The linewidth of the excitonic transition is in the range of 800 μeV. The small peak at 2.2246 eV could arise from one exciton state of a nearby QD. In II-VI semiconductors the Coulomb correlation energies are high enough so that different states of a single QD cover a large energy range. This increases the probability that the emission from different dots is overlapping.

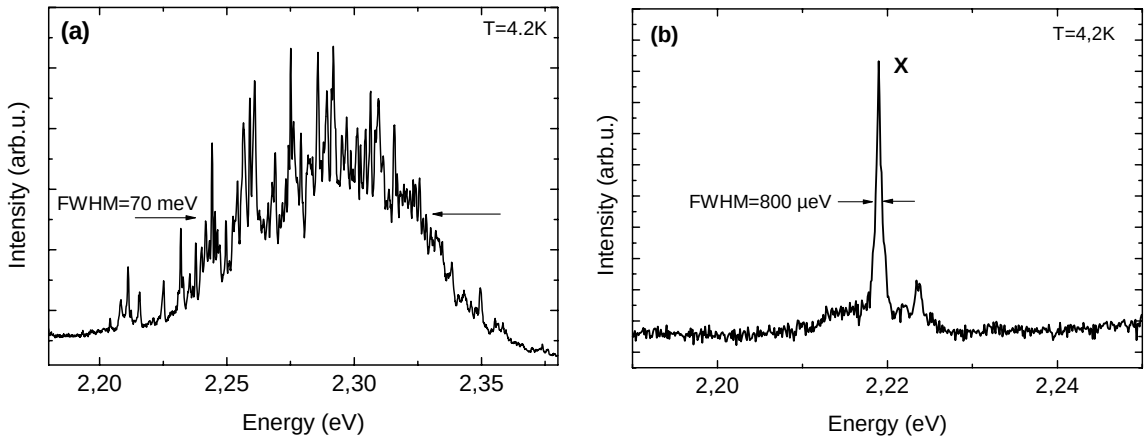

Figure 52. (a) PL spectrum of the QD ensemble in the unstructured region of the sample. (b) PL spectrum of individual QD recorded through a shadow mask.

PL measurements with different bias voltages applied to the diode were performed to investigate the quantum confined Stark shift of QD excitons and the transition from the PL to the tunneling regime. The shift and tuning behavior of the PL signal was found to depend on the excitation energy. Under the condition of cw excitation by a diode laser with an emission wavelength of 404 nm (corresponds to 3.07 eV, above the bandgap of ZnSe) no Stark shift of the exciton lines and no tunneling of the carriers out of the QD were observed for reverse bias voltages between 0 V and -4 V. This effect is most likely caused by screening off the internal electric field. The exact mechanism for this screening (internal charge accumulation, lateral potential drop etc.) remains unclear until now. However, for the interesting regimes of nearly resonant excitation (typically 200 meV above the ground state of the QD) or resonant excitation of the CdSe QDs, the above-described screening effects are almost absent. Figure 53 shows a two-dimensional map of the PL energy of the QD excitons for nearly resonant excitation at 515 nm (2.41 eV) as a function of the bias voltage. Several transition lines with different intensities, most likely caused by contributions from exciton states of different dots, were observed. In the following the strongest exciton line labeled (X), which is assigned to the ground state of an individual QD, is discussed.

Figure 54 shows the QCSE and the intensity of the exciton ground state (X) emission as a function of the applied negative bias voltage and the resulting electric field. The QCSE of

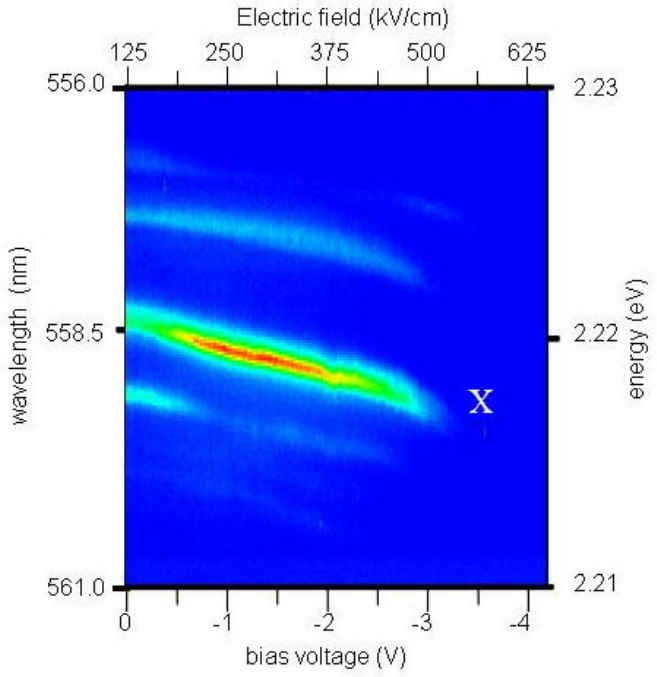

Figure 53. Voltage dependent photoluminescence of an individual QD (some weaker line may arise from a different QD) at different excitation power. The color coding constitutes the luminescence intensity.

the exciton transition causes an almost linear redshift of the QD ground state with increasing reverse bias voltage. The Stark effect becomes linear for very high electric fields. Between 0 V and -3 V bias, we observe a Stark shift of about 4.4 meV. Since this Stark shift is almost linear, we can further conclude that the QD exciton has an almost constant induced dipole moment $\mu_{el}=er$, where e is the elementary charge and r is the separation between the centres of gravity of the electron and hole probability distributions. Based on the model by Skolnick et al. [106] we calculate this separation to be about 0.13 nm from the observed Stark shift. This value is considerably smaller than the previously observed value of about 0.4 nm in typical InAs/GaAs devices [111].

In Figure 54 the intensity of X is normalized for convenience. The intensity of the neutral exciton firstly increases up to a reverse bias voltage of about -1V and then decreases for higher reverse bias voltage. The initial increase of intensity could be caused by charging effects. The charged states of the excitons, e.g. states shown in Figure 8 may have competing emissions. For example the charges from a p-shell exciton would tunnel out of the QD with increasing applied electric field or relax into the s-shell contributing to the neutral exciton transition. For even larger reverse bias voltages, the intensity of the neutral exciton is reduced, since tunneling of carriers out of the QD is now competing with the radiative decay of the excitons. For reverse bias conditions exceeding -3 V, which corresponds to an internal electric field in the order of 500 kV/cm, the PL is effectively quenched due to tunneling of carriers out of the QD. At these voltages the transition to the

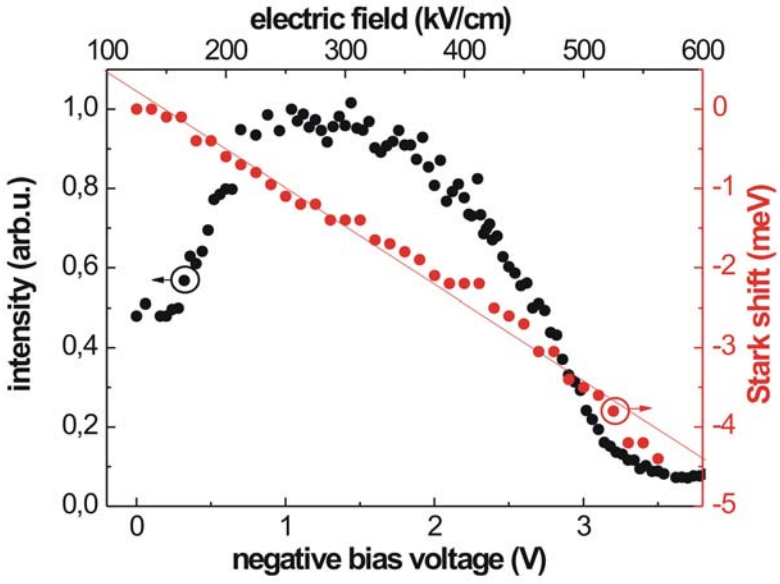

Figure 54. The QCSE and the intensity of the exciton ground state (X) as a function of applied negative bias voltage and resulting electric field. The intensity is normalized and the Stark shift is fitted lineary.

photocurrent regime is taking place and the photocurrent can be measured.

The tunnelling time τ_t of carriers out of the CdSe QD was modelled using the approximation described by Eq. 32. The bandgap structure and the tunnelling potential width at different bias voltages were calculated by using 1D Poisson. The QCSE was considered. Figure 55 shows the results of the calculated tunnelling time and barrier width for electrons and holes as a function of the electric field. The potential barrier width drops exponentially with the increase of the applied electric field. The band offset for CdSe in ZnSe was assumed to be 20% for the valence band and 80% for the conduction band, resulting in a smaller tunnelling barrier for holes than for electrons. Consequently, the tunnelling time for holes is smaller than for electrons, despite the higher effective mass of holes. The tunnelling time also drops exponentially with increasing electric field. At an applied electric field of about 500 kV/cm the dot PL is effectively quenched as shown in Figure 54. At this field the tunnelling time of electrons is in the order of several ns, whereas the holes tunnel much faster within split ps. However, the confinement energy of the QD can not be measured directly and small variations of this parameters result in a considerable change of the tunnelling time. The spontaneous radiative recombination lifetime of excitons in CdSe QDs is in the order of 300 ps [99]. Thus we assume that at higher electric fields the hole tunnels before recombination can occur. The electron has no counterpart to recombine and therefore tunnels subsequently. Both processes contribute to the photocurrent which can be measured.

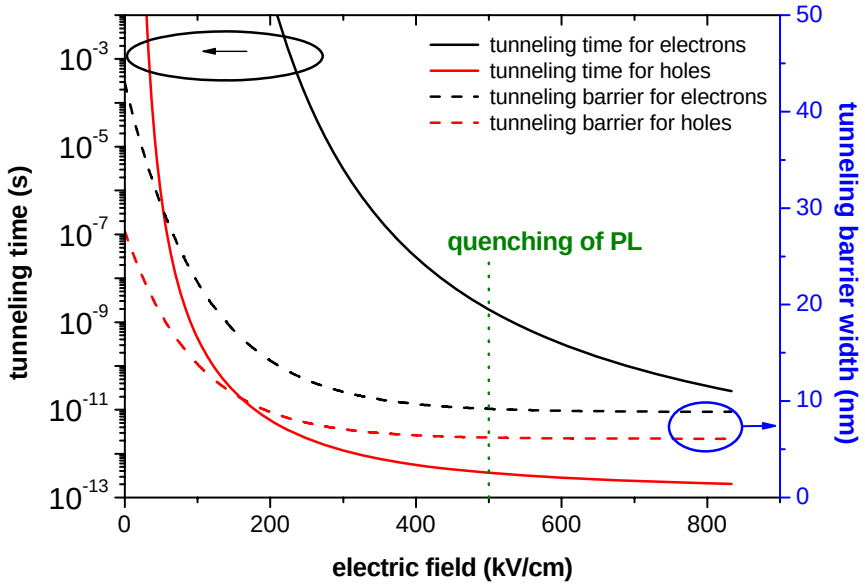

Figure 55. Calculated tunnelling barrier width and tunneling time out of the CdSe QDs for electrons and holes as a function of the electric field.

5.4 Photocurrent spectroscopy

The basic principle of the photocurrent spectroscopy is the resonant absorption of photons and subsequent tunnelling of the charge carriers out of the QD. The tunnelling charges contribute to a photocurrent which is detected by a high resolution current measurement. The photoionization of the excitation leads then to the separation of (in the ideal case) exactly one electron-hole pair, and hence by tunnelling to the net transport of elementary charges between the contacts of the photodiode. The photocurrent from the QD after a coherent state preparation is given by the key formula

$$I_{PC} = fe\rho \qquad \text{Eq. 33}$$

where f is the laser repetition frequency, e the elementary charge and ρ represents the occupancy of the intermediate states. In this equation it is assumed that all excitons tunnel out of the QD (i.e. no radiative recombination) considerably faster than the laser repetition time. This equation gives the maximum expected current from the QD if the system is prepared in the upper state ρ = 1 (|X⟩, QD is occupied with one exciton). For a laser repetition frequency of 160 MHz used in our experiments, this results in a maximum current of $I_{PC_{\max}} = 25\,pA$.

For the photocurrent detection the leakage current of the Schottky diode has to be lower than the expected maximum photocurrent. Using the diode design described above we have obtained leakage currents of less than 10 pA at room temperature and less than 0.5 pA at 4 K up to a reverse bias voltage of -5 V, corresponding to an internal electric field of approximately 700 kV/cm.

For resonant excitation of the QDs, a laser-pumped optical parametric oscillator (OPO) was used for pulsed and tunable excitation between 515 nm and 560 nm. The laser pulses had a repetition frequency of 160 MHz, a width of about 3 ps, and a spectral width of about 3 meV. The experimental setup for the photocurrent measurements is explained in detail in the thesis of S. J. Michaelis de Vasconcellos [112]. It allows high resolution measurements of the photocurrent, only limited by the accuracy of the applied bias voltage of the diode and the line width of the resonant laser excitation.

Figure 56 shows the results of photocurrent measurements taken at the same aperture of the shadow mask as the PL data in Figure 53. The grey curve shows a very low leakage current without excitation. For a resonant excitation condition of a QD exciton at 0V bias voltage (blue curve), we observe a photocurrent of less than 10 pA. The same applies even

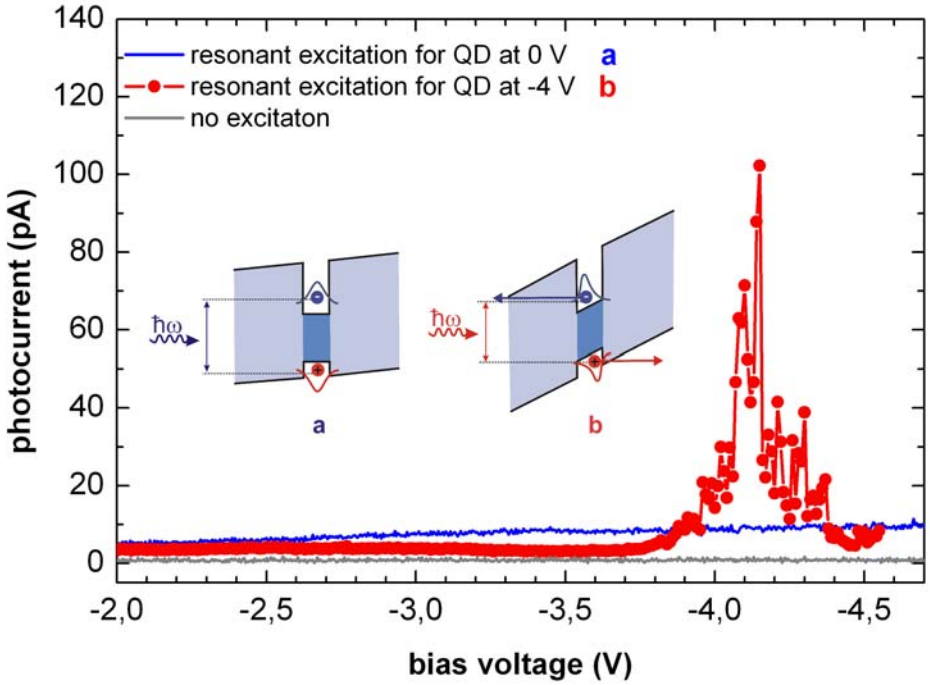

Figure 56. Photocurrent spectra of an individual QD when excited resonantly to the ground state energy at -4 V (red curve). The blue curve corresponds to the photocurrent of non-resonant excitation of the QD and the grey curve is the resulting dark current without excitation.

to a reverse bias voltage up to -5 V. This background photocurrent is most likely due to the contribution of QDs, which are more remote from the aperture. The red curve shows the photocurrent for resonant excitation of the one QD exciton at -4V bias voltage. Using the QCSE, the QD exciton transition energy was tuned into resonance with the laser energy by increasing the negative bias voltage. A strong photocurrent signal at about -4.1 V applied bias voltage was observed. This signal has, as a matter of fact, a clear resonant signature as expected for a QD exciton. The peak amplitude of this photocurrent signal (about 100 pA) is considerably higher than expected even for π-pulse excitation (about 25 pA). The enhanced peak amplitude of the photocurrent signal is interpreted as a strong evidence for the appearance of avalanche multiplication of photoelectrons and holes in the depletion layer of our device. In our experiment the field-induced ionization of QD excitons occurs at an internal electric field of about 600 kV/cm, thus making the subsequent avalanche multiplication of the photocurrent very likely. In comparison to the well-known InGaAs/GaAs [113] structures, CdSe/ZnSe PDs require internal electric fields, which are almost 20 times larger, for photocurrent extraction.

In summary, the optoelectronic properties of ZnSe Schottky diodes containing Stransky-Krastanov self assembled CdSe QDs were investigated. Several fundamental effects were found: observation of the QCSE and a reduction of the luminescence due to tunnelling. For resonant excitation of the QDs by 3 ps laser pulses, we observe a pronounced photocurrent signal at a bias voltage of about -4.1 V, which we consider as a first demonstration of an electric readout of the charge state of widegap CdSe QDs incorporated in a ZnSe based Schottky diode. Both, the low leakage current of 12 pA up to a bias voltage of -5 V at room temperature and the photocurrent readout make widegap CdSe/ZnSe PDs attractive for future coherent applications.

6 Conclusions and Outlook

Many research groups around the world are working towards the highly ambitious technological goal of quantum information technology. The major topic is here the developing of active key components. In this thesis, preliminary devices for quantum information technology based on II-VI semiconductor systems which include fluorine impurities and CdSe quantum dots (QDs) have been demonstrated.

One of the beneficial devices is the microdisk (MD) laser, which combines the in-plane emission and ease of fabrication, with the key advantages of small volume, high quality factor and low threshold. In this work, the fabrication process of MDs based on strained fluorine-doped ZnSe QWs between ZnMgSe barriers on a GaAs pedestal was developed. The structural properties of these ZnSe microstructures were investigated by high resolution micro-photoluminescence and micro-Raman scattering experiments. Micro-photoluminescence spectra, measured at different positions of our MDs revealed a clear emission shift to lower energies when moving the excitation from the centre to the edge of the disk. Micro-Raman measurements reveal a redshift of the ZnSe LO phonon frequency. The modelling of these experimental results showed that the shift can be explained by the homogeneous release of strain along the radial direction of the disk from the centre (ZnSe compressively strained on GaAs) to the edge (ZnSe tensile strained on ZnMgSe). This results in a substantial band gap narrowing effect along the radial direction of the disk from the centre to the edge, which enhances the charge carrier transfer to the periphery, where the optical whispering gallery modes are localized. Furthermore, the absence of the ZnSe TO Raman line in the spectra indicates that strain relaxation in the structure is not accompanied by the generation of extended defects. These findings are in good agreement with the observation of relatively high Q values (up to 4500) of our disks.

The appearance of low-threshold lasing in fluorine-doped ZnSe QW MDs with 3 and 6 μm diameter indicates that small ensembles of fluorine donors have been successfully coupled to a cavity with Purcell factors high enough to achieve laser thresholds of less than 100 Wcm^{-2}. Such a reduced threshold also facilitates some schemes for quantum communication and quantum computation based on donor-bound exciton transitions. Further, the reduction in inhomogeneous broadening by preserving the uniform strain

acquired during molecular beam epitaxy growth may allow such applications as lasing without inversion.

In addition, a waveguide for ZnSe/ZnMgSe MDs in form of a freestanding micro-membrane based on the same structure as MDs was developed. The investigations of the strain distribution in such membranes by atomic force microscopy, μ-Raman scattering and μ-photoluminescence indicated the defect free release of strain in the direction of the centre of the membrane. Again, the strain release results in a bandgap narrowing and thus in the carrier transport to the centre of the membrane, which enhances the emission efficiency. These preliminary investigations demonstrate an important step towards integrated optical waveguide systems with II-VI compound semiconductors. With an additional photonic crystal the membranes are suitable for further applications as bending waveguides, nanoscale laser with an even lower threshold than MD lasers and single photon sources in quantum information technology.

Another important component for quantum information technology is the qubit. One approach to investigate semiconductor qubits makes use of a two-level system, which is formed by the exciton ground state in a single QD. With individual QDs enclosed in a Schottky photodiode with near-field shadow mask on a semi-transparent contact, electrical and optical access is provided to probe and to modify the quantum state of QD excitons. In this thesis, ZnSe photodiodes containing self assembled CdSe QDs have been fabricated and analyzed. The optoelectronic properties of the diode were investigated. At quasi-resonant excitation of individual QDs, we observed a pronounced redshift of the luminescence emission with increasing negative bias voltage due to the quantum confined Stark effect. At a bias voltage exceeding -3 V (corresponding to an applied electric field of about 500 kV/cm) the PL was quenched due to depletion of the exciton ground state by tunnelling. For resonant excitation of the QDs, we observed a pronounced photocurrent signal at a bias voltage of about -4.1 V, which we consider as first demonstration of an electric readout of widegap CdSe QDs incorporated in a ZnSe based Schottky diode. However, the material system is not easy to handle regarding processing and spectroscopy, but high confinement, high Coulomb correlation energies, and the enhanced photocurrent output makes widegap CdSe/ZnSe photodiodes very attractive for future coherent applications.

The presented examples of components for quantum information technology demonstrate that there are many open questions and interesting new concepts. The challenge for the years to come will be the engineering of devices based on quantum principles that are actually more powerful, more efficient or less costly than their classical counterparts.

Symbols and Abbreviations

Symbols

a_0	lattice constant
$\boldsymbol{b}$	Burgers vector
D^0X	donor-bound exciton
DD	dislocation density
d_{hkl}	spacing of the lattice planes
e	representation for an electron or the elementary charge (1.6022×10^{-19} C)
F	electric field
f	laser repetition frequency
f_p	Purcell factor
FX	free exciton
(hkl)	Miller indices
h	Planck's constant (4.1357×10^{-15} eVs)
$\hbar$	$h/2\pi$ (6.5821×10^{-16} eVs)
hh	heavy hole
I_{PC}	photocurrent
$\boldsymbol{k}$	wave vector
L^-	plasma-phonon coupled mode
lh	light hole
m^*	effective mass
n	refractive index
$\boldsymbol{q}$	crystal momentum vector
Q	quality factor
$q_\perp$, $q_\parallel$	reciprocal lattice constants
TES	two electron satellite (transition)
V	mode volume
V_{bias}	bias voltage of the photo diode
β	fraction of spontaneous emission coupled into a lasing mode
δ-$doped$	one monolayer doped
ε	strain tensor
λ	wavelength
μ_{el}	dipole moment
τ_t	tunnelling time
ω	frequency
$\|0\rangle$, $\|X\rangle$	qubit initial states

Abbreviations

AFM	atomic force microscope
CCD	charge coupled device
CdSe	cadmium slenide
cw	continuous excitation (continuous wave)
Eq.	equation
FWHM	full width half maximum
GaAs	gallium arsenide
HRXRD	high-resolution X-ray diffraction
InGaAs	indium gallium arsenide
LO	longitudinal optical (phonon)
MBE	molecular beam epitaxy
MD	microdisk
ML	monolayer
OPO	optical parametric oscillator
PC	photocurrent (spectroscopy)
PD	photodiode
PID	proportional-integral-derivative (controller)
PL	photoluminescence (spectroscopy)
QCSE	quantum confined Stark effect
QD	quantum dot
QW	quantum well
RF	radio frequency
RHEED	reflection high energy electron diffraction
RIE	reactive ion etching
RS	Raman scattering (spectrometry)
RSM	reciprocal space map
SEM	scanning electron microscope (microscopy)
SPL	selective photoluminescence
TE	transverse electric (mode)
TM	transverse magnetic (mode)
TO	transverse optical (phonon)
UHV	ultra high vacuum
WGM	whispering gallery mode
ZnMgSe	zinc magnesium selenide
ZnSe	zinc selenide
NA	numerical aperture

Bibliography

[1] Gordon E. Moore, *Cramming more components onto integrated circuits*, Electronics **38** (1965) Nr. 8

[2] R.P. Feynman: *Quantum Mechanical Computers*, Otp. News **11** (1985) 11

[3] L. DiCarlo, J. M. Chow, J. M. Gambetta, Lev S. Bishop, B. R. Johnson, D. I. Schuster, J. Majer, A. Blais, L. Frunzio, S. M. Girvin, et al.: *Demonstration of two-qubit algorithms with a superconducting quantum processor*, Nature **460** (2009) 240

[4] Alberto Politi, Jonathan C. F. Matthews and Jeremy L. O'Brien, Shor's: *Quantum Factoring Algorithm on a Photonic Chip*, Science **325** (2009) 1221

[5] T. D. Ladd, F. Jelezko, R. Laflamme, Y. Nakamura, C. Monroe and J. L. O'Brien: *Quantum computers*, Nature **464** (4 March 2010) 45

[6] K. Sanaka, A. Pawlis, T. D. Ladd, K. Lischka and Y. Yamamoto: *Indistinguishable Photons from Independent Semiconductor Nanostructures*, Phys. Rev. Lett. **103** (2009) 053601

[7] W. Braun: *Applied RHEED,* Springer Verlag, Heidelberg, 1999

[8] W.L. Bragg: *The diffraction of short electromagnetic waves by a crystal*, Proc. Cambridge Phil. Soc. **17** (1913) 43

[9] P. Gay, P.B. Hirsch and A.Kelly: *The estimation of dislocation densities in metalsfrom X-ray data*, Acta Metal **1** (1953) 315

[10] Y. Chen, X. Liu, E. Weber, E. D. Bourret, Z. Liliental-Weber, E. E. Hailer, J. Washburn, D. J. Olego, D. R. Dorman, J. M. Gaines and N. R. Tasker*: Structures and electronic properties of misfit dislocations in ZnSe/GaAs(001) heterojunctions*, Appl. Phys. Lett. **65** (1994) 549

[11] T. Ruf: *Phonon Raman scatterin in semiconductors, quantum wells and superlattices*, edited by G. Höhler, Vol. 142 of Springer Tractst in Modern Physics, (Springer-Verlag, Berlin 1998)

[12] M. Cardona: *Light scatterin in Solids*, edited by M. Cardona, Vol. 8 of Topics in Applied Physics, (Springer-Verlag, Berlin, 1975)

[13] V.V. Tishchenko, Y.S. Raptis, E. Anastassakis and N.V. Bondar: *Optical studies of ZnSe-ZnS/GaAs(100) single quantum wells grown by photo-assisted vapor phase Epitaxy,*Sol. State Comm. **96** (1995) 793

[14] N. V. Bondar', V. V. Tishchenko and M. S. Brodin*: Exciton Energy States and Photoluminescence Spectra of the Strained-Layer ZnS–ZnSe superlattices*, Semiconductors, **34** (2000) 568

[15] J.L. Merz, H. Kukimoto, K. Nassau, and J.W. Shiever, *Optical Properties of Substitutional Donors in ZnSe*, Phys. Rev. B **6** (1972) 545

[16] A.M. Stoneham, Theory of Defects in Solids: *Electronic Structure of Defects in Insulators and Semiconductors*, Great Britain, J.W. Arrowsmith Ltd, Bristol, 1975

[17] Landolt-Börnstein III, "*Zahlenwerte und Funktionen aus aturwissenschaften und Technik*", Band 17, Teilband a,b, edited by O. Madelung (Springer-Verlag, Berlin 1982).

[18] A Pawlis 1,2, K Sanaka 1, S Götzinger 1, Y Yamamoto 1 and K Lischka: *Investigation of excitons bound to fluorine donors in ZnSe*, Sem. Sci. Tech. **21** (2006) 1412

[19] P. J. Dean, D. C. Herbert, C. J. Werkhoven, B. J. Fitzpatrick, and R. N. Bhargava: *Donor bound-exciton excited states in zinc selenide*, Phys. Rev. B **23** (1981) 4888

[20] K.L. Teo, Y.P. Feng, M.F. Li, T.C. Chong, J.B. Xia: *Band structure of* $Mg_{1-x}Zn_xS_ySe_{1-y}$, Semicond. Sci. Technol. **9** (1994) 349

[21] T.-Y. Chung, J.H. Oh, S.-G. Lee, J.-W. Jeong, K.J. Chang: *Optical properties of ZnSSe/ZnMgSSe quantum wells*, Semicond. Sci. Technol. **12** (1997) 701

[22] V. Kulakovskii, G. Bacher, R. Weigand, T. Kümmell, A. Forchel, E. Borovitskaya, K. Leonardi, and D. Hommel: *Fine structure of biexciton emission in symmetric and asymmetric CdSe/ZnSe single quantum dots*, Phys. Rev. Lett. **82** (1999) 1780

[23] H.H. von Grünberg, Energy levels of CdSe quantum dots: *Wurtzite versus zinc-blende structure*, Phys. Rev. B **55** (1997) 2293

[24] M. O. Scully and M. Fleischhauer: *Lasers Without Inversion,* Science **263** (1994) 337

[25] S. E. Harris, J. E. Field, and A. Imamoglu: *Nonlinear optical processes using electromagnetically induced transparency*, Phys. Rev. Lett. **64** (1990) 1107

[26] J. I. Cirac, P. Zoller, H. J. Kimble, and H. Mabuchi: *Quantum State Transfer and Entanglement Distribution among Distant Nodes in a Quantum Network*, Phys. Rev. Lett. **78** (1997) 3221

[27] W. Yao, R.-B. Liu, and L. J. Sham: *Theory of Control of the Spin-Photon Interface for Quantum Networks*, Phys. Rev. Lett. **95** (2005) 030504

[28] L. I. Childress, J. M. Taylor, A. Sørensen, and M. D. Lukin: *Fault-tolerant quantum repeaters with minimal physical resources and implementations based on single-photon emitters*, Phys. Rev. A **72** (2005) 052330

[29] E. Waks and J. Vuckovic: *Dipole Induced Transparency in Drop-Filter Cavity-Waveguide Systems,* Phys. Rev. Lett. **96** (2006) 153601

[30] S. M. Clark, Kai-Meis C. Fu, T. D. Ladd, and Y. Yamamoto: *Quantum Computers Based on Electron Spins Controlled by Ultrafast Off-Resonant Single Optical Pulses*, Phys. Rev. Lett. **99** (2007) 040501

[31] T. D. Ladd, P. van Loock, K. Nemoto, W. J. Munro, and Y. Yamamoto: *Hybrid quantum repeater based on dispersive CQED interactions between matter qubits and bright coherent light,* New J. Phys. **8** (2006) 184

[32] V. A. Karasyuk, D. G. S. Beckett, M. K. Nissen, A. Villemaire, T. W. Steiner, and M. L. W. Thewalt: *Fourier-transform magnetophotoluminescence spectroscopy of donor-bound excitons in GaAs,* Phys. Rev. B **49** (1994) 16381

[33] A. Yang, M. Steger, D. Karaiskaj, M. L. W. Thewalt, M. Cardona, K. M. Itoh, H. Riemann, N. V. Abrosimov, M. F. Churbanov, A. V. Gusev A. D. Bulanov, A. K. Kaliteevskii, O. N. Godisov, P. Becker, H.-J. Pohl, J. W. Ager, and E. E. Haller: *Optical Detection and Ionization of Donors in Specific Electronic and Nuclear Spin States*, Phys. Rev. Lett. **97** (2006) 227401

[34] K. M. C. Fu, C. Santori, C. Stanley, M. C. Holland, and Y. Yamamoto*: Coherent Population Trapping of Electron Spins in a High-Purity n-Type GaAs Semiconductor*, Phys. Rev. Lett. **95** (2005) 187405

[35] R. de Sousa and S. Das Sarma: *Theory of nuclear-induced spectral diffusion: Spin decoherence of phosphorus donors in Si and GaAs quantum dots,* Phys. Rev. B **68** (2003) 115322

[36] A. M. Tyryshkin, S. A. Lyon, A. V. Astashkin, and A. M. Raitsimring: *Electron spin relaxation times of phosphorus donors in silicon,* Phys. Rev. B **68** (2003) 193207

[37] S. L. McCall, A. F. J. Levi, R. E. Slusher, S. J. Pearton, and R. A. Logan: *Whispering-gallery mode microdisk lasers*, Appl. Phys. Lett. **60** (1992) 289

[38] X. Liu, W. Fang, Y.H. Wu, S.T. Ho, H. Cao and R.P.H. Chang: *Optically pumped ultraviolet microdisk laser on a silicon substrate,* Appl. Phys. Lett. **84** (2004) 2488

[39] A.C. Tamboli, E.D. Haberer, R. Sharma, K.H. Lee, S. Nakamura and E.L. Hu: *Room-temperature continuous-wave lasing in GaN/InGaN microdisks,* Nat. Photonics **1** (2007) 61

[40] P. Michler, A. Kiraz, L. Zhang, C. Becher, E. Hu and A. Imamoglu: *Laser emission from quantum dots in microdisk structures,* Appl. Phys. Lett. **77** (2000), 184

[41] H. Cao, J.Y. Xu, W.H. Xiang, Y. Ma, S.-H. Chang, S.T. Ho and G.S. Solomon*: Optically pumped InAs quantum dot microdisk lasers*, Appl. Phys. Lett. **76** (2000) 3519

[42] T.J. Kippenberg, J. Kalkman, A. Polman and K.J. Vahala: *Demonstration of an erbium-doped microdisk laser on a silicon chip,* Phys. Rev. A **74** (2006) 051802

[43] M. Hovinen, J. Ding, A.V. Nurmikko, D.C. Grillo, J. Han et al.: *Blue-green laser emission from ZnSe quantum well microresonators*, Appl. Phys. Lett. **63** (1993) 3128

[44] U. Mohideen, W.S. Hobson, S.J. Pearton, F. Ren, R.E. Slusher: *GaAs/AlGaAs microdisk lasers*, Appl. Phys. Lett. **64** (1994), 1911

[45] B. Corbett, J. Justice, L. Considdine, S. Walsh, W.M. Kelly*: Low-threshold lasing in novel microdisk geometries*, IEEE Photonics Technol. Lett. **8** (2004) 855

[46] J. Faist, C. Gmachl, M. Striccoli, C. Sirtori, F. Papasso*: Quantum cascade disk laser*, Appl. Phys. Lett. **69** (1996) 2456

[47] K.C. Zeng, L. Dai, J.Y. Lin, H.X. Jiang: *Optical resonance modes in InGaN/GaN multiple-quantum-well microring cavities,* Appl. Phys. Lett. **75** (1999), 2563

[48] Gayral, B., Gerard, J.M., Lemaitre, A., Dupuis, C., Mamin, L., Pelouard, J.L.,: *High-Q wet-etched GaAs microdisks containing InAs quantum boxes,*Appl. Phys. Lett. **75** (1999) 1908

[49] D.M. Bagnall, B. Ullrich, H. Sakai, Y. Segawa: *Micro-cavity lasing of optically excited CdS thin films at room temperature,* J. Cryst. Growth **214–215** (2000), 1015

[50] Zwiller, V., Falth, S., Persson, J., Seifert,W., Samuelson, L., Bjork, G.: *Fabrication and time-resolved studies of visible microdisk lasers,* J. Appl. Phys. **93** (2003a) 2307

[51] Gianordoli, S., Hvozdara, L., Strasser, G., Schrenk, W., Faist, J., Gornik, E.,: *Long-wavelength (λ=10 μm) quadrupolar-shaped GaAs-AlGaAs microlasers*, IEEE J. Quantum Electron. **36** (2000) 458

[52] Fasching, G., Tamosiunas, V., Benz, A., Andrews, A.W., Unterrainer, K., Zobl, R., Roch, T., Schrenk, W., Strasser, G., Terahertz quantum-cascade

lasers IEEE J. Quantum Electron. **43** (2007) 687
[53] T. Baba, M. Fujita, M. Kihara, R. Watanabe: *Lasing characteristics of GaInAsP-InP strained quantum-well microdisk injection lasers with diameter of 2-10 μm,* IEEE Photonics Technol. Lett. **9** (1997) 878
[54] Fujita, M., Sakai, A., Baba,T.,: *Ultrasmall and ultralow threshold GaInAsP-InP microdisk injection lasers: design, fabrication, lasing characteristics, and spontaneous emission factor*, IEEE J. Select. Top. Quantum Electron. **5** (1999) 673
[55] Fujita, M., Ushigome, R., Baba, T.: *Continuous wave lasing in GaInAsP microdisk injection laser with threshold current of 40μA*, Electron. Lett. **36** (2000) 9
[56] Zhang, L., Hu, E.: *Lasing from InGaAs quantum dots in an injection microdisk,* Appl. Phys. Lett. **82** (2003) 319
[57] Ide, T., Baba, T., Tatebayashi, J., Iwatomo, S., Nakaoka, T., Arakawa: *Room temperature continuous wave lasing in InAs quantum-dot microdisks with air cladding*, Y., Opt. Express **13** (2005) 1615
[58] L. L. Chao, G. S. C. III, C. Kothandaraman, T. Marshall, E. Snoeks, M. Buijs, K. Haberern, J. Petruzzello, G. M. Haugen and K. K. Law: *Activation energy of nonradiative processes in degraded II–VI laser diodes*, Appl. Phys. Lett. **70** (1997) 535
[59] Okuyama H, Nakano K, Miyajima T and Akimono K: *Epitaxial growth of ZnMgSSe on GaAs substrate by molecular beam Epitaxy,* J. Cryst. Growth **117** (1992) 139
[60] Y. Yamamoto, S. Machida, and G. Björk: *Microcavity semiconductor laser with enhanced spontaneous emission,*Phys. Rev. A **44** (1991) 657
[61] J. Renner, L.Worschech, A. Forchel, S. Mahapatra, and K. Brunner: *Whispering gallery modes in high quality ZnSe/ZnMgSSe microdisks with CdSe quantum dots studied at room temperature*, Appl. Phys. Lett. **89** (2006) 091105
[62] J. Renner, L.Worschech, A. Forchel, S. Mahapatra, and K. Brunner: *CdSe quantum dot microdisk laser*, Appl. Phys. Lett. **89** (2006) 231104
[63] J.-M. Gérard and B. Gayral: *Strong Purcell Effect for InAs Quantum Boxes in Three-Dimensional Solid-State Microcavities*, J. Lightw.Technol. **17** (1999) 2089
[64] L. Rayleigh: *Further applications of Bessel's functions of high order to the whispering gallery and allied problems*, Philos. Mag. **27** (1914) 100
[65] A. Yariv: *Optical Electronics*, Oxford University Press, USA, 1991
[66] R. E. Slusher, A. F. J. Levi, U. Mohideen, S. L. McCall, S. J. Pearton, and R. A. Logan: *Threshold characteristics of semiconductor microdisk lasers*, Appl. Phys. Lett. **63** (1993) 1310
[67] S. Bittner, B. Dietz, M. Miski-Oglu, P. Oria Iriarte, A. Richter, and F. Schäfer: *Experimental test of a two-dimensional approximation for dielectric microcavities*, Phys. Rev. A **80** (2009) 023825
[68] K. Wolf, S. Jilka, A. Rosenauer, G. Schütz, H. Stanzl, T. Reisinger and W. Gebhardt: *High-resolution x-ray diffraction investigations of epitaxially grown ZnSe/GaAs layers*, J. Phys. D **28** (1995) A120
[69] H. Okuyama et al., IEICE Trans. Electron. E83-C, 536 (2000)
[70] T. Matsumoto, T. Kato, M. Hosoki and T. Ishida*: Raman Study of Misfit Strain and Its Relaxation in ZnSe Layers Grown on GaAs Substrates,* J.J. Appl. Phys. **26** (1987), L576

[71] F. Cerdeira, C.J. Buchenauer, F.H. Pollak and M. Cardona: *Stress-Induced Shifts of First-Order Raman Frequencies of Diamond- and Zinc-Blende-Type Semiconductors*, Phys. Rev. B **5** (1972), 580

[72] B. Weinstein and R. Zallen, in *Light Scattering in Solids IV*, (Eds:. M. Cardona and G. Grüntherodt), Springer, Heidelberg, (1982), p.463

[73] D. Huang, C. Jin, D. Wang, X. Liu, J. Wang and X. Wang*: Crystal structure and Raman scattering in* $Zn_{1-x}Mg_xSe$ *alloys*, Appl. Phys. Lett. **67** (1995) 3611

[74] W. Richter, in *Solid State Physics*, Vol 78 of Springer Tracts in Modern Physics, ed. by G. Höhler (Springer, Berlin, 1976), p. 121

[75] O. Pages, M.A. Renucci, O. Briot and R.L. Aulombard, *Anomalous behaviour of optical phonon modes in ZnSe epitaxial layers*, J. Raman Spec. **28** (1997) 551

[76] O. Pages, H. Erguid, J.P. Laurenti, M. Certier, D. Bormann, B. Khelifa, O. Briot: *Inhomogeneous electric field-induced Raman scattering at ZnSe/GaAs interfaces,* J. Appl. Phys. **85** (1999) 2371

[77] D. Olego and M. Cardona: *Raman scattering by coupled LO-phonon—plasmon modes and forbidden TO-phonon Raman scattering in heavily doped p-type GaAs,* Phys. Rew. B **24** (1981) 7217

[78] Panfilova M, Pawlis A, Arens C, Michaelis de Vasconcellos S, Berth G, Hüsch K P, Wiedemeier V, Zrenner A and Lischka K: *Micro-Raman imaging and micro-photoluminescence measurements of strain in ZnMgSe/ZnSe microdiscs,* Microelectron. J. **40** (2009) 221

[79] M. Fujita, R. Ushigome and T. Baba*: Strain relaxation effect in microdisk lasers with compressively strained quantum wells*, Appl. Phys. Lett. **80** (2002) 1511

[80] A. Pawlis, M. Panfilova, D. J. As, K. Lischka, K. Sanaka, T. D. Ladd and Y. Yamamoto: *Lasing of donor-bound excitons in ZnSe microdisks*, Phys. Rev. B **77** (2008) 153304

[81] A.Pawlis, M.Panfilova, K.Sanaka, T.D.Ladd, D.J.As, K.Lischka, Y.Yamamoto: *Low-threshold ZnSe microdisk laser based on fluorine impurity bound-exciton transitions,* Microel. J. **40** (2009) 256

[82] U. T. Schwarz, E. Sturm, W. Wegscheider, V. Kümmler, A. Lell, and V. Härle, *Optical gain, carrier-induced phase shift, and linewidth enhancement factor in InGaN quantum well lasers,* Appl. Phys. Lett. **83** (2003) 4095

[83] G. Björk and Y. Yamamoto: *Analysis of semiconductor microcavity lasers using rate equations,* IEEE J. Quantum Electron. **27** (1991) 2386

[84] Oxborrow, M.: *Traceable 2-D Finite-Element Simulation of the Whispering-Gallery Modes of Axisymmetric Electromagnetic Resonators*, IEEE Transactions on Microwave Theory and Techniques **55** (2009) 1209

[85] Z. Guo and H. Quan: *Energy Transfer to Optical Microcavities With Waveguides*, Journal of Heat Trans, **129** (2007) 44

[86] Gorodetsky, M. L., and Ilchenko, V. S: *Optical Microsphere Resonators: Optimal Coupling to High-Q Whispering-Gallery Modes*, J. Opt. Soc. Am. B, **16** (1999) 147

[87] Serpenguzel, A., Arnold, S., and Griffel, G.: *Excitation of Resonances of Microspheres on an Optical Fiber*, Opt. Lett. **20** (1995) 654

[88] Knight, J. C., Cheung, G., Jacques, F., and Birks, T. A.: *Phase-Matched Excitation of Whispering Gallery Mode Resonances Using a Fiber Taper*, Opt. Lett. **22**(1997) 129

[89] Klunder, D. J. W., Krioukov, E., Tan, F. S., van Der Veen, T., Bulthuis, H. F.,

Sengo, G., Otto, C., Hoekstra, H. J. W. M., and Driessen, A.: *Vertically and Laterally Waveguide-Coupled Cylindrical Microresonators in Si3N4 on SiO2 Technology*, Appl. Phys. B **73** (2001) 603

[90] Guo, Z., Quan, H., and Pau, S., : *Optical Resonance in Fabricated Whispering-Gallery Mode Microcavity*" ASME J. Heat Transfer, **127** (2005) 808.

[91] M. Loncar, D. Nedelijkovic, T. Doll, J. Vuckovic, A. Scherer, and T. P.Pearsall: *Probing Lepton Flavor Violation at Future Colliders,* Appl. Phys. Lett. **77** (2000) 1937

[92] O. Painter, R. K. Lee, A. Scherer, A. Yariv, J. D. O'Brien, P. D. Dapkus, and I. Kim: *Two-Dimensional Photonic Band-Gap Defect Mode Laser,* Science **284** (1999) 1819

[93] J.-R. Cao, P.-T. Lee, S.-J. Choi, R. Shafiiha, S.-J. Choi, J. D. O'Brien, and P. D. Dapkus: *Nanofabrication of photonic crystal membrane lasers*, J. Vac. Sci. Technol. B **20** (2002) 618

[94] V. S. C. Manga Rao and S. Hughes: *Single Quantum Dot Spontaneous Emission in a Finite-Size Photonic Crystal Waveguide: Proposal for an Efficient "On Chip" Single Photon Gun*, Phys. Rev. Lett. **99** (2007) 193901

[95] A. Zrenner, E. Beham, S. Stufler, F. Findeis, M. Bichler, and G. Abstreiter: *Coherent properties of a two-level system based on a quantum-dot photodiode,*Nature **418** (2002) 612

[96] A. Zrenner, P. Ester, S. Michaelis de Vasconcellos, M.C. Hübner, L. Lackmann, S. Stufler and M. Bichler: *Coherent optoelectronics with single quantum dots*, J. Phys.: Condens. Matter **20** (2008) 454210

[97] S. J. Boyle, A. J. Ramsay, A. M. Fox, and M. S. Skolnick, A. P. Heberle and M. Hopkinson: *Beating of Exciton-Dressed States in a Single Semiconductor InGaAs/GaAs Quantum Dot,* Phys. Rev. Lett. **102** (2009) 207401

[98] P. Borri, W. Langbein, S. Schneider, U. Woggon, R. L. Sellin, D. Ouyang and D. Bimberg*: Ultralong Dephasing Time in InGaAs Quantum Dots*, Phys. Rev. Lett. **87** (2001) 157401

[99] B. Patton, W. Langbein, and U. Woggon: *Trion, biexciton, and exciton dynamics in single self-assembled CdSe quantum dots*, Phys. Rev. B **68** (2003) 125316

[100] X. Zhong, R. Xie, Y. Zhang, T. Basche and W. Knoll: *High-Quality Violet- to Red-Emitting ZnSe/CdSe Core/Shell Nanocrystals,* Chem. Mater. **17** (2005) 4038

[101] K. Sebald, P. Michler, T. Passow, D. Hommel, G. Bacher and A. Forchel: *Single-photon emission of CdSe quantum dots at temperatures up to 200 K*, Appl. Phys. Lett. **81** (2002) 2920

[102] D. A. B. Miller, D. S. Chemal, T. C. Damen, A. C. Gossard, W. Wiegmann, T. H. Wood, C. A. Burrus: *Band-Edge Electroabsorption in Quantum Well Structures: The Quantum-Confined Stark Effect,* Phys. Rev. Lett. **53** (1984) 2173

[103] D. A. B. Miller, D. S. Chemla, T. C. Damen, A. C. Gossard, W. Wiegmann, T. H. Wood, C. A. Burrus: *Electric field dependence of optical absorption near the band gap of quantum-well structures,* Phys. Rev. B **32** (1985) 1043

[104] J. Seufert, M. Obert, M. Scheibner, N. Gippius, G. Bacher, A. Forchel, T. Passow, K. Leonardi, and D. Hommel: *Stark effect and polarizability in a single CdSe/ZnSe quantum dot*, Appl. Phys. Lett. **79** (2001) 1033

[105] G. Bacher, R. Weigand, J. Seufert, V. D. Kulakovskii, N. A. Gippius, A. Forchel K. Leonardi and D. Hommel: *Biexciton versus Exciton Lifetime in a Single Semiconductor Quantum Dot*, Phys. Rev. Lett. **83** (1999) 4417

[106] R. Oulton, J.J. Finley, A.D. Ashmore, I.S. Gregory, D.J. Mowbray, M.S. Skolnik, M.J. Steer, S.-L. Liew, M.A. Migliorato and A.J. Cullis: *Manipulation of the homogeneous linewidth of an individual In(Ga)As quantum dot,* Phys. Rev. B **66** (2002) 045313

[107] T. Makino, R. André, J.-M. Gérard, R. Romestain, Le Si Dang, M. Bartels, K. Lischka and D. Schikora: *Single quantum dot spectroscopy of CdSe/ZnSe grown on vicinal GaAs substrates*, Appl. Phys. Lett. **82** (2003) 2227

[108] D. Schikora, S. Schwedhelm, D.J. As, K. Lischka, D. Litvinov, A. Rosenauer, D. Gehrtsen, M. Strassburg, A. Hoffmann, D. Bimberg: *Investigations on the Stranski–Krastanow growth of CdSe quantum dots*, Appl. Phys. Lett. **76** (2000) 418

[109] F. Völklein and T. Zetterer: *Praxiswissen Mikrosystemtechnik*. Vieweg Verlag, 2. edition, 2006

[110] M. Strassburg: *Energietransfer von Exzitonen in ZnCdSe Quantenpunkt Ensembles*, Dissertation, Technische Universität Berlin (2002).

[111] Jin, Peng Li, C. M. Zhang, Z. Y. Liu, F. Q. Chen, Y. H. Ye, X. L. Xu, B. Wang, Z. G.: *Quantum-confined Stark effect and built-in dipole moment in self-assembledInAs/GaAs quantum dots*, Appl. Phys. Lett. **85** (2004) 2791

[112] S. J. Michaelis de Vasconcellos, *Coherent Optoelectronic Control of Single Excitons*, doctoral thesis, Paderborn (2009)

[113] A. Zrenner, S. Stufler, P. Ester, S. Michaelis de Vasconcellos, M.C. Huebner, M. Bichler: *Recent developments in single dot coherent devices,* Phys. Stat. Sol. (b) **243** (2006) 3696

List of Publications

- M. Panfilova, A. Pawlis, A. Shchekin, S. Lemeshko and K. Lischka: "Investigations of strain in ZnMgSe/ZnSe micro-discs by means of the micro-Raman imaging", Phys. Stat. Sol. (c) 1–3 (2010) /DOI10.1002/pssc.200983210

- M. Panfilova, S. Michaelis de Vasconcellos, A. Pawlis, K. Lischka and A. Zrenner: "Photocurrent-spectroscopy of CdSe quantum dot photodiodes", Physica E (2010), doi:10.1016/j.physe.2010.01.013

- K. Lorenz, I.S. Roqan, N. Franco, K.P. O´Donnell, E. Alves, C. Trager-Cowan, R.W. Martin, D.J. As, M. Panfilova: "Europium doping of cubic (zinkblende) GaN by ion implantation" J. Appl. Phys. **105** (2009) 113507

- A. Pawlis, M. Panfilova, K. Sanaka, T.D. Ladd, D.J. As, K. Lischka, Y. Yamamoto: "Low-threshold ZnSe micro-disc laser based on fluorine impurity bound-exciton transitions", Microelectron. J. **40** (2009) 256

- S.M. de Vasconcellos, A. Pawlis, C. Arens, M. Panfilova, A. Zrenner, K. Lischka: "Exciton spectroscopy on single CdSe/ZnSe quantum dot photodiodes", Microelectron. J. **40** (2009) 221

- A. Kabir, M. Panfilova, A. Pawlis, H.P. Wagner, K. Lischka: "Well-width dependence of the phase coherent photorefractive effect in ZnSe quantum wells", Microelectron. J. **40** (2009) 303

- M. Panfilova, A. Pawlis, C. Arens, S.M. de Vasconcellos, G. Beth, K.P. Hüsch, V. Wiedemeier, A. Zrenner, K. Lischka: "Micro-Raman imaging and micro-photoluminescence measurements of strain in ZnMgSe/ZnSe micro-discs", Microelectron. J. **40** (2009) 215

- I. S. Roqan, K. P. O'Donnell, C. Trager-Cowan, B. Hourahine, R. W. Martin, K. Lorenz, E. Alves, D. J. As, M. Panfilova, I. M. Watson: „Luminescence spectroscopy of Eu-implanted zincblende GaN", phys. stat. sol. (b) **245** (2008) 170

- A. Pawlis, M. Panfilova, D. J. As, K. Lischka, K. Sanaka, T. D. Ladd, and Y. Yamamoto: "Lasing of donor-bound excitons in ZnSe micro-discs", Phys. Rev. B **77** (2008) 153304

Acknowledgements

In Paderborn, I have been fortunate enough to be surrounded by many people who kindly offered me help to complete this research, so I would like to express my gratitude to them.

Firstly, I would like to thank my supervisor Prof. Dr. Klaus Lischka for letting me work in this great research group "Optoelectronic Semiconductors" at the University of Paderborn. He has suggested me broad range of research topics and has given a lot of valuable advices.

I would like to thank my committee members, Prof. Dr. Christine Silberhorn served as the second examiner, Prof. Dr. Wolf Gero Schmidt kindly acted as the chair in my thesis defense and Dr. Christof Hoentzsch as representative of scientific colleagues.

Thanks also goes to Prof. Dr. Donat J. As for plenty of valuable discussions and advices to support this challenging work.

Specially, I have to thank my office partner Dr. Alexander Pawlis for teaching me the MBE of ZnSe and GaAs. I thank him for lasing measurements in Stanford University and all the helpful discussions that had a notable share in the success of this research.

I would like to thank master students Y. Martin Kim and Y. Alexander Leier for their help in the performance and analysis of electrical measurements and of SiO_2 properties and their outstanding teamwork. Also thanks to bachelor student Philipp Kröger for cooperative work on membranes.

In addition I would like to thank Christoph Claßen from the group of Prof. Rolf Schuhmann for simulations of microdisk modes and Steffen J. Michaelis de Vasconcellos from Prof. Arthur Zrenner's group for kind support of production and measurements on photodiodes, and for discussions.

Next I have to mention my other fellow ex. Ph. D. students Dr. Jörg Schörmann, Dr. Stefan Potthast, Dr. Christof Arens, Dr. Stefan Preuss and Dr. Elena Tschumak for the helpful (not only in physics) discussions and a pleasant work atmosphere.

For help with English and for administrative support, I thank Irmgard Zimmermann.

Of course I am also grateful for the help of our optoelectronics staff, Bernhard Vollmer and Siegfried Igges.

I also appreciate other group members for their good influence. Maik Paluga, Alexander Zado, Christian Mietze, Thorsten Schupp, Mohamed Rashad Ahmed, Olga Kasdorf, Ricarda Maria Kemper, Jörn Kampmeier and Matthias Bürger.

Last but not least, I would like to express my gratitude to my parents for their love, encouragement and financial support during my whole life.